Nanostructured thin film pseudocapacitive electrodes for enhanced electrochemical energy storage

Laura O'Neill

Wolfson College

A thesis submitted for the degree of

Doctor of Philosophy

Hilary term 2014

Abstract

This thesis presents work relating to the fabrication of novel thin film electrodes for energy storage applications, with a focus on low cost, nanostructured transition metal oxides, and electrode manufacture by atomised spray deposition.

Iron oxide (FeO_x) nanowires were synthesised hydrothermally and combined with multi-walled carbon nanotubes (MWNT) in sprayed electrodes, which provided the necessary conductivity enhancement for effective energy storage. The spray processing technique allowed for facile control over the relative fraction of MWNTs in the sprayed electrodes. Optimised electrodes were investigated in a range of aqueous electrolytes, and the best energy storage behaviour occurred in Na_2SO_3 with a maximum capacitance from cyclic voltammetry of 312 Fg^{-1} at a scan rate of 2 mVs^{-1}. The FeO_x/MWNT electrodes were investigated for their suitability as lithium-ion battery anodes and showed reasonable energy storage behaviour.

Nickel oxide (NiO) electrodes were manufactured by hydrothermal synthesis and annealing followed atomised spray deposition. The performance of the NiO electrodes was enhanced though combination with aqueous graphene suspensions, produced in-house by ultrasonic exfoliation of graphite. The processing route used to combine the nanomaterials was considered and a co-synthesis route resulted in the best perform-

ing electrodes. Different substrates were investigated, as the most commonly used Ni-foam substrate reacted with the basic electrolytes necessary for electrochemical activity of NiO. NiO/graphene electrodes showed charge/discharge capacitances of up to 571 Fg^{-1} at a current density of 10 Ag^{-1}, which was maintained at over 300 Fg^{-1} at a very high current density of 100 Ag^{-1}.

Asymmetric supercapacitor devices were constructed using various combinations of FeO_x, NiO, and commercial carbon black electrodes to extend the operating potential window beyond the $\sim$1.23 V limit of symmetric aqueous-electrolyte devices. Power densities of over 20 $kWkg^{-1}$ were achieved for an FeO_x/MWNT-carbon device, which was comparable with current commercial carbon-only supercapacitors.

Acknowledgements

First and foremost, I would like to thank my supervisor Prof. Patrick Grant, for his guidance and assistance in overcoming the steep learning curve I faced when I started at Oxford, and whose diligent attention to detail has made this thesis considerably more readable. His assistance allowed me to travel extensively to conferences and other academic institutions, which exposed me to research and techniques I would otherwise not have experienced.

I would like to extend my gratitude to my co-supervisor Dr. Colin Johnston for the ongoing day-to-day support and advice he provided, and for training me on many analytical pieces of equipment.

My sincere thanks go to the many staff members who assisted and advised me academically; to Dr. Valaria Nicolosi for help with graphene synthesis, Dr. Alison Crossley for assistance with XPS, Dr. Chris Salter and Ms. Gabriella Chapman for training and assistance on the microscopes, Dr. Frank Dillon for considerable experimental assistance, and Mr. Philip Holloway for performing XRD on several of my samples.

I would like to thank Mr. Robin Vincent, Mr. Trevor Knibbs, Mr. Richard Turner and Dr. Andrew Lui for their extensive technical support and assistance with the

many equipment issues I encountered over the course of the project.

Special thanks go to Dr. Beatriz Mendoza-Sanchez, Dr. Meng Jiang, Dr. Chaopeng Fu and Ms. Ann Huang, the experienced members of my group who helped and advised me constantly with day-to-day experimental work and analysis. Further thanks go to many of my colleagues at Begbroke Science Park whose presence and conversations provided a welcome and necessary divergence from lab work, particularly Mr. Amoghavarsha Mahadevegowda, Mr. Cameron Taylor and Mr. Vincent Tobin, and also Ms. Qin Lei, Ms. Yunqi Wang and Mr. Zuliang Hong. Thanks to Dr. Enzo Liotti and Dr. Flynn Castles for their suggestions, assistance and advice during the writing of this thesis. I would also like to thank Mrs. Jan Pearson and Mrs. Julie Young for the considerable administrative and emotional support they provided during my time at Oxford and who our group relies on heavily.

My heartfelt thanks go to my parents, for their constant and unwavering support and for quietly making me feel like I could achieve anything. Finally, to Mr. Luke Moulton, for his endless encouragement and whose tireless drive inspired me during every stage of the project.

This work was funded by the EPSRC Supergen Energy Storage Consortium.

Contents

List of Figures

List of Tables

Chapter 1

Introduction

1.1 The increasing need for energy storage

In the last decade the world's population has increased by 1 billion[1] and, when coupled with the increasing standard of living expected by populations of developing countries, this puts substantial pressure on energy production across the globe. In addition to the increased demand for energy, governments and industries are increasingly interested in a move away from non-renewable fossil fuel technology (currently $> 80\%$ of supply) to energy production from renewable sources since current fossil fuel reserves are likely to be exhausted within the next century and CO_2 emissions are now limited by the Kyoto protocol.[2] If renewable energy sources are either to become a viable alternative or a supplement to fossil fuels and nuclear energy then it is vital to have high quality, reliable energy storage technologies in order to maximise the utilisation of these intermittent power sources.

Current electrical energy storage and consumption can be split into several distinct

areas including, but not limited to:

- Grid storage for supplying electricity to homes, buildings and industry
- Transportation of people and goods
- Consumer and portable electronics e.g. mobile phones, computers

Each category outlined brings specific requirements for energy storage in terms of capacity, time scales and mass limitations. However, all require rapid and significant improvements in stability, cycle life and energy density of current energy storage devices, to cope with the demands of a growing population and novel renewable energy technologies. For example, improved stationary energy storage would allow for a less centralized grid system which would alleviate problems brought about by adverse weather and demand overload. Indeed, it is often the case that technological advancements are marred by the limited performance of current energy storage devices, and this is particularly true of the smart phone[3] and electric vehicle markets.[4]

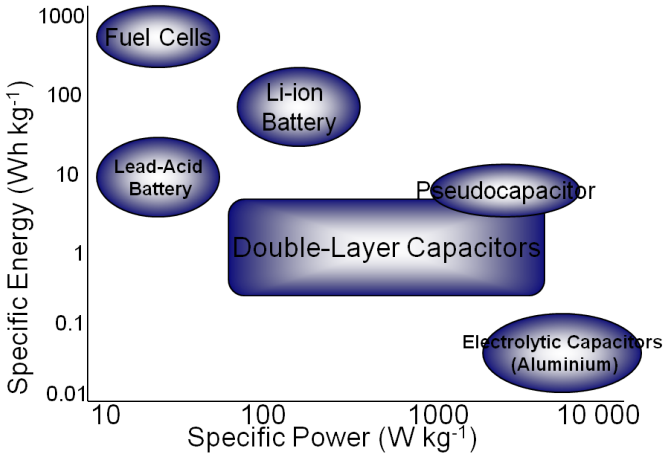

Figure 1.1: A Ragone plot, comparing the relative specific energy and power provided by a range of electrochemical energy storage systems

Several of the most common energy storage devices and their relative energy/power properties are shown in Figure 1.1. Each device has different energy storage characteristics and therefore distinct applications, although it is increasingly common to utilise a combination of devices in hybrid systems to maximise efficiency and minimise weight.[5–7] A comparison of charge storage mechanisms occurring in electrostatic capacitors, electrochemical capacitors and lithium-ion batteries is shown in Figure 1.2 and the resulting performance characteristics are described in Table 1.1.

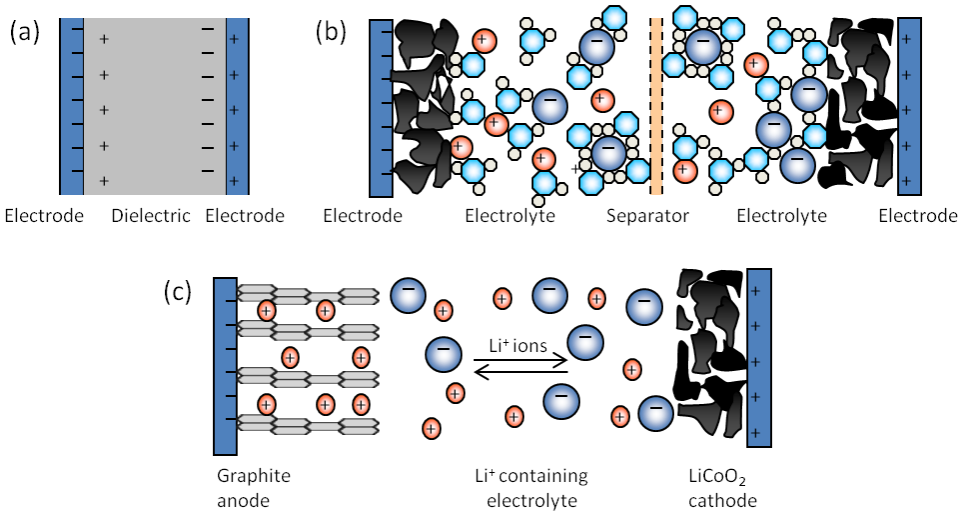

Figure 1.2: Schematic of (a) an electrostatic capacitor, (b) an electrochemical capacitor with an aqueous electrolyte where charge is stored in the Helmholtz double layer, and (c) a lithium ion battery in a lithium containing, air sensitive electrolyte in which charge storage occurs though intercalation into graphite and simultaneous reduction of $LiCoO_2$ to $Li_{(1-x)}CoO_2 + xLi^+$

	Electrostatic capacitor	**Electrochemical capacitor**	**Battery**
Charge stored	Between charged plates	Electrode/electrolyte interface	Entire electrode
Charge/discharge time	10^{-6}-10^{-3}s/10^{-6}-10^{-3}s	1-120s/1-120s	0.3-3h/1-3h
Specific power (W kg^{-1})	$\gg$10000	500-10000	$<$1000
Specific energy (Wh kg^{-1})	$<$0.1	1-10	20-150
Cycle life	$\gg 10^6$	$>10^6$	$\sim$1500
Efficiency ($\frac{t_d}{t_c}$)	$\sim$1	0.85-0.99	0.7-0.85

Table 1.1: Comparison of energy storage characteristics, adapted from reference 8

.

1.2 Electrochemical capacitors

Electrochemical capacitors (ECs), or 'supercapacitors' store energy through electrostatic charge separation in a Helmholtz double layer, known as electric double layer capacitance (EDLC) and/or through reversible surface redox reactions, known as 'pseudocapacitance' (Figure 1.2 (b)). Extremely high electrode surface areas and 'surface only' charge storage allows ECs to provide higher specific energy than classic electrostatic capacitors (10 Wh kg^{-1} vs <0.1 Wh kg^{-1}) and higher power densities than batteries (500-10000 W kg^{-1} vs <1000 W kg^{-1}), shown in Figure 1.1 and Table 1.1. ECs can therefore be used to bridge the gap between these two well established energy storage devices and are most suited for high power applications and back up power supplies such as uninterruptable power supply (UPS) and load levelling. Although the first EC patent, based on a carbon black electrode, was recorded in 1957,[8] research into supercapacitors has only gained momentum in the past 15 years. Because of this, there is an ongoing need to improve performance and consider manufacturing approaches before widespread mass-production is viable.

The most significant step forward in supercapacitor development has been the use of electrode materials with designed nanostructures.[9–12] Nano-sized electrode materials provide the highest surface area to volume ratio as well as minimising electron and ion diffusion pathways and, when used in combination with aqueous electrolytes, do not present safety risks due to secondary reactions as is the case for nanostructured lithium-ion batteries. Other techniques to maximise the performance of ECs include the use of organic/ionic liquid electrolytes[13] or the fabrication of devices with non-equivalent anode and cathode materials, known as asymmetric devices.[14, 15] These are discussed in more detail in Chapter 2.

1.3 Objectives and outline

Currently, commercial supercapacitors have been brought to market in both automotive and stationary systems. Commercial devices are based on low cost, low toxicity, activated carbon materials with high conductivity and extremely high surface area. However, the maximum energy density provided by carbon electrodes is limited by the surface area-dominated charge storage mechanism (EDLC). Transition metal oxides are able to provide higher energy density due to the availability of surface transition metal ions that can undergo fast, reversible redox reactions involving an electrochemical charge transfer process. Therefore there is interest in developing low cost, stable, safe transition metal oxide-based electrodes that have the potential to be combined with, or replace activated carbon electrodes. A better understanding of the electrode/electrolyte interface is vital for device optimisation and to minimise capacitance fading whilst maximising cycle life.

The most studied transition metal oxides are currently RuO_2[16] and MnO_2.[17] Despite the excellent performance of these materials, commercialisation has so far been limited to niche applications because of high cost and/or concerns over lifetime performance, especially cycling. Amongst the other transition metal oxides considered in the literature, iron oxides (Fe_2O_3,[18] Fe_3O_4,[19] FeOOH[20]) and nickel oxides (NiO,[21] $Ni(OH)_2$[22, 23]) have emerged as promising candidates for scalable, possibly lower cost systems. Building on this relatively recent interest in Ni and Fe oxides, the objectives of this work are as follows:

- To investigate nanostructured iron oxide based electrodes for energy storage as a low cost, safe, saleable material and to understand better the energy storage mechanisms of iron oxide in aqueous electrolytes

- To optimise and characterise pseudocapacitive electrodes with characteristics and properties suitable for combination with iron oxide in a full cell asymmetric device

- To investigate the suitability of all-sprayed, nanostructured asymmetric combinations of transition metal oxide and carbon electrodes in full-cell arrangements in terms of stability and energy density/specific energy enhancement.

The thesis is structured as follows. Chapter 2 is a literature review of the fundamental theories behind supercapacitor devices and the current academic state of the art with respect to the most relevant materials and devices to be studied. Chapter 3 describes the experimental techniques used in the thesis. Chapter 4 provides results of the supercapacitor behaviour of an iron oxide/carbon nanotube system which is then investigated further for its potential in lithium-ion batteries in Chapter 5. A new hybrid NiO/graphene system is then investigated in Chapter 6 for its electrochemical capacitor capabilities with a focus on optimisation of the processing route. Chapter 7 considers several full-cell devices using the electrodes optimised in previous chapters. Finally, concluding remarks and future work are outlined in Chapter 8.

Bibliography

[1] http://www.census.gov/population/international/data.

[2] In *Kyoto Protocol*. United Nations Framework Convention on Climate Change, (Nov 2009).

[3] Pikul, J., Gang Zhang, H., Cho, J., Braun, P., and King, W. *Nature Comm.* **4** (2013).

[4] Armand, M. and Tarascon, J. *Nature* **451**(7179), 652–657 (2008).

[5] Vosen, S. R. and Keller, J. O. *Int. J. Hydrogen. Energ.* **24**(12), 1139–1156 (1999).

[6] Xie, Q., Wang, Y., Kim, Y., Pedram, M., and Chang, N. *IEEE T. Comut. Aid. D.* **32**(7), 1003–1016 (2013).

[7] Cericola, D. and Ktz, R. *Electrochim. Acta* **72**, 1–17 (2012).

[8] Becker, H. July 23 (1957). US Patent 2,800,616.

[9] Wang, J., Zhang, S., Guo, Y., Shen, J., Attia, S., Zhou, B., Zheng, G., and Gui, Y. *J. Electrochem. Soc.* **148**(6), D75–D77 (2001).

[10] Arico, A. S., Bruce, P., Scrosati, B., Tarascon, J. M., and Van Schalkwijk, W. *Nature Materials* **4**(5), 366–377 (2005).

[11] Chen, Z., Qin, Y., Weng, D., Xiao, Q., Peng, Y., Wang, X., Li, H., Wei, F., and Lu, Y. *Advanced Functional Materials* **19**(21), 3420–3426 (2009).

[12] Chmiola, J., Yushin, G., Gogotsi, Y., Portet, C., Simon, P., and Taberna, P. *Science* **313**(5794), 1760–1763 (2006). cited By (since 1996)773.

[13] Zhu, Y., Murali, S., Stoller, M., Ganesh, K., Cai, W., Ferreira, P., Pirkle, A., Wallace, R., Cychosz, K., Thommes, M., Su, D., Stach, E., and Ruoff, R. *Science* **332**(6037), 1537–1541 (2011).

[14] Long, J. W., Belanger, D., Brousse, T., Sugimoto, W., Sassin, M. B., and Crosnier, O. *MRS Bulletin* **36**(7), 513–522 (2011).

[15] Cottineau, T., Toupin, M., Delahaye, T., Brousse, T., and Blanger, D. *Appl. Phys. A. Mater.* **82**(4 SPEC. ISS.), 599–606 (2006).

[16] Hu, C. C., Chang, K. H., Lin, M. C., and Wu, Y. T. *Nano Letters* **6**(12), 2690–2695 (2006).

[17] Toupin, M., Brousse, T., and Belanger, D. *Journal of the Materials Chemistry* **16**, 3184–3190 (2004).

[18] Nasibi, M., Golozar, M. A., and Rashed, G. *Mater. Lett.* **85**, 40 (2012).

[19] Hallam, P. M., Gomez-Mingot, M., Kampouris, D. K., and Banks, C. E. *RSC Adv.* **2**(16), 6672 (2012).

[20] Qu, Q., Yang, S., and Feng, X. *Adv. Mat.* **23**(46), 5574 (2011).

[21] Nelson, P. A., E. J. M. and Owens, J. R. *J. Electrochem. Soc.* **14**, 524–529 (2002).

[22] Yan, J., Fan, Z., Sun, W., Ning, G., Wei, T., Zhang, Q., Zhang, R., Zhi, L., and Wei, F. *Adv. Func. Mater.* **22**(12), 2632–2641 (2012).

[23] Jiang, H., Zhao, T., Li, C., and Ma, J. *J. Mat. Chem.* **21**(11), 3818–3823 (2011).

Chapter 2

Literature Review

This review considers the recent literature related to materials for supercapacitor electrodes with a focus on pseudocapacitive materials, 1-dimensional (1D) nanostructured forms and techniques used to maximise the performance of supercapacitors by balancing energy and power density. A general context is low-cost, scalable, safe devices operating in aqueous electrolytes. The literature relating to more toxic/flammable organic electrolytes or room temperature ionic liquids is mentioned only in their competitive context; similarly supercapacitor electrodes based on activated carbon or graphite are only reviewed in the context that they define the commercial state of the art in supercapacitors.

2.1 Basic concepts

2.1.1 Electrochemical energy storage

The challenge of producing enough energy to meet increasing societal needs goes hand in hand with developing effective ways to store energy produced at times of low demand. Currently, energy is most commonly stored chemically in fuels such as oil and gas, or electrochemically in devices such as batteries and fuel cells. Supercapacitors, known more accurately as 'electrochemical capacitors', are energy storage devices based on charge storage at an electrode/electrolyte interface and have been suggested as ideal devices to compliment batteries in electrical systems within areas such as portable electronics, transportation and aviation.[1–3]

In a simple electrostatic capacitor, charge is stored between two electrodes separated by a highly insulating solid material known as a dielectric, and capacitance is the ratio of electric charge on each electrode (Q) to the potential different between the electrodes (V):

$$C = \frac{Q}{V} \tag{2.1}$$

In a supercapacitor, the solid, insulating dielectric is replaced by an electrolyte solution with the ions of the electrolyte moving towards the electrode on polarization and creating an electric double layer (Figure 2.1 (b)). Polarization of the electrode induces the reversible adsorption of electrolyte ions onto the electrode and charge separation occurs giving a capacitance of:

$$C = \frac{\varepsilon_0 \varepsilon_r A}{d} \tag{2.2}$$

where ε_0 is the permittivity of free space, ε_r is the dielectric constant of the electrolyte, A is the ion accessible surface area of the electrode and d is the size of the double layer formed. This relationship shows that capacitance can be maximised by combining aqueous electrolytes, which have much higher dielectric constants that organic solvents (84 for H_2O *cf* 30.9 for N,N dimethylformamaide and 65 for propylene carbonate), with a high surface area electrode. Efforts towards the production of nanoporous electrodes with surface areas approaching 2000 m^2 g^{-1} has proven to improve capacitance.[4]

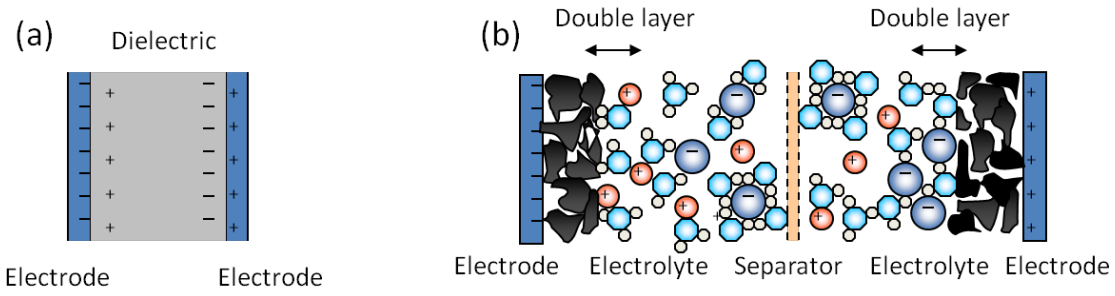

Figure 2.1: A schematic representation of energy storage in (a) electrostatic and (b) electrochemical capacitors

2.1.2 Specific energy and power

Although capacitance, in Farads or Farads per gram, is the most common measure of evaluating the performance of individual supercapacitor electrodes in the literature, it is useful to assess devices in terms of specific energy (in Wh kg^{-1}) and specific power (in W kg^{-1}) so that comparisons with other electrochemical energy storage devices e.g. batteries and fuel cells, can be made. It should be noted that specific energy/power is often incorrectly referred to as energy/power density in the literature, which has the units Wh L^{-1}/W L^{-1}, however the terms are interchangeable when the volumetric or gravimetric measurement is omitted.

The specific energy/energy density (E) of a supercapacitor is directly proportional to capacitance and can be calculated from Equation 2.3:

$$E = \frac{1}{2}CV^2 \tag{2.3}$$

and so can be maximised by increasing both the capacitance and the operating potential window (often limited by the breakdown of the electrolyte).

Specific power/power density is a measure of the energy delivered per unit time ($P = \frac{E}{t}$) and the maximum power of a device is given by Equation 2.4):

$$P_{max} = \frac{V^2}{4R_s} \tag{2.4}$$

where R_s is the equivalent series resistance (ESR, Ω) which takes into account the resistance of the capacitor components and is often estimated to be *(2/3) t.r'/A*, where t is electrode thickness, r' is electrolyte resistivity and A is electrode geometric area. In order to achieve high specific power, specific capacitance and applied potential should be maximised and ESR minimised.

2.1.3 Capacitance Mechanisms

Electrochemical capacitors can be split into two sub-classes, defined by the mechanism of charge storage. In both cases a Helmholtz double layer is formed upon charging, as shown in Figure 2.1 (b) and the charge storage is related to the electrode itself and the orientation of electrolyte ions in the double layer.

The more basic charge storage mechanism is known as electric double layer capac-

itance (EDLC) and as the name suggests, charge is stored purely by electrostatic charge separation across the electrochemical double layer. As such, materials for EDLC combine high surface area with high conductivity. The charge/discharge cycle life of these materials is theoretically limitless as there is no physical or chemical change in the structure of the electrode material. The most common electrode material in these capacitor systems is carbon due to the low cost, high conductivity and potential for high surface area by chemical 'activation' or etching of nanopores onto the surface.

The second mechanism of capacitance is known as pseudocapacitance, and differs from EDLC as it is faradaic due to the involvement of fast, reversible charge transfer of valence electrons across the double layer. The charge transfer can be brought about by (1) redox reactions involving electrolyte ions and transition metal ions, (2) adsorption/desorption of protons or electrolyte cations, or (3) reversible doping/dedoping of conducting polymer chains. As faradaic reactions occur at specific potentials dependent on the individual reaction being considered, pseudocapacitance is characterised by a potential dependant capacitance and there is an approximately linear relationship between charge stored and potential supplied, modifying Equation 2.1 to:

$$C = \frac{\Delta Q}{\Delta V} \tag{2.5}$$

The charge transfer across the double layer that occurs during pseudocapacitance means higher energy densities can be achieved, however this is usually accompanied by a reduction in long term stability and cycle life of the electrode. Transfer across the double layer induces degradation of the electrode structure brought about by

physical/mechanical strain which leads to pulverisation and eventually fading of the capacitance. Typical materials utilised in pseudocapacitive electrodes include; (1) transition metal oxides, which have many easily accessible oxidation states, and (2) conducting polymers, which can undergo redox reactions through the π conjugated backbone of the polymer chain. The difference in the charge storage mechanisms means materials with differing chemical, electronic and mechanical properties are suitable for EDLCs and pseudocapacitors.

2.2 Electrode Materials - EDLC

Carbon is an extremely well studied material for EDLCs due to a large achievable surface area (of 1000s of $m^2\ g^{-1}$), good physiochemical stability, good processability and low cost. It is possible to produce symmetric devices with both cathode and anode consisting of the same carbon material which results in cheap, easily fabricated devices. The low cost of the raw materials used in carbon based supercapacitors have ultimately led to the commercialisation of these devices. So called 'activated carbons' (carbons where the mesoporosity has been maximised by heat treatment with gases at high temperature) are industrially attractive in terms of cost and can have extremely high surface areas of over 2000 m^2g^{-1} which has led to specific capacitances of up to 300 F g^{-1}.[5] The most commonly available commercial capacitors consist of high surface area carbon electrodes and have an specific energy of *ca.* 6 Wh kg^{-1}. Beyond activated carbons, carbons with designed nanostructures (high aspect ratio, tailored porosity) such as carbon nanotubes, carbon nanohorns and derivatives of graphene have been widely studied due to the level of control that is possible when coming from a 'bottom-up' approach to morphology and structure.

2.2.1 Activated Carbon

Current commercial supercapacitor electrodes are almost exclusively comprised of amorphous, activated carbons mixed with appropriate conductivity enhancers and binders. Activated carbons are produced through the pyrolysis of low cost natural materials such as coconut shells or coal and the extremely low cost of materials and manufacture combined with excellent cycle life mean that few of the extensive pool of alternative materials have shown economic competitiveness with carbon. Despite this, activated carbons tend to give relatively low capacitances, not usually exceeding 150 F g^{-1} in aqueous electrolyte,[6] and so for high specific energy applications, there is wide interest in developing low cost, high capacitance alternatives.

2.2.2 Carbon Nanotubes

Carbon nanotubes (CNTs) are cylindrical nanostructured carbon allotropes with a high aspect ratio and accessible surface area of up to 475 m^2 g^{-1}. They are electrochemically stable in most electrolytes and electrically conductive (up to 5 x 10^5 S m^{-1}) and since their discovery have attracted wide interest due to their unusual mixture of mechanical strength, electrical conductivity and chemical properties.[7] CNTs can be structured in two general ways: 'Single walled nanotubes' (SWNTs) and 'Multi walled nanotubes' (MWNT), dependent on the number of graphene sheets involved. MWNTs have a metallic conductivity whereas SWNTs can be semi-conductors and capacitive properties have been studied for both single,[8, 9] and multiwalled[10] nanotube electrodes.

It was quickly discovered that when fabricated in an electrode, CNTs would naturally

produce a superior structure to that of activated carbon or graphite, as the 1-D nature and low pore distribution means CNTs naturally tangle up to form an open, mesoporous structure providing high accessibility of the electrolyte to the entire surface area which in combination with the low ESR of the material led to high power densities of over 8 kW kg^{-1}.[11] An open, mesoporous structure produced by tangled CNTs is shown in Figure 2.2.

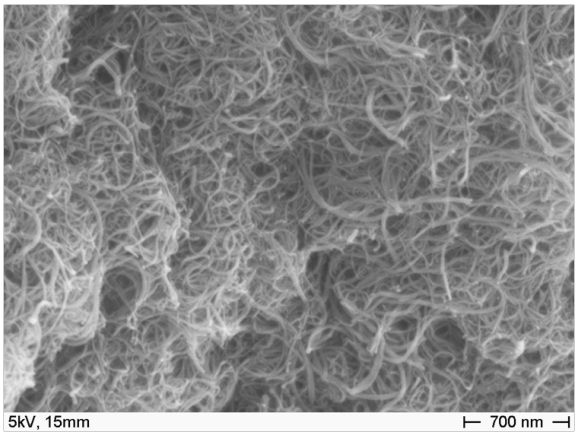

Figure 2.2: An example of a mesoporous CNT electrode

Like other forms of carbon, to obtain reasonable capacitance, it is usually necessary to activate CNTs by heating in acidic or basic aqueous solution, which can also functionalise them with surface heteroatom groups, (oxygenate or nitrogenous). Pre-treatment increases the surface area and mesoporosity of the nanotubes and if functionalisation also occurs, can introduce an element of pseudocapacitance to nanotube-based electrodes. Functionalisation additionally renders the nanotubes 'self-adhesive' so that no binder material is necessary to hold the structures together which not only reduces the mass of the electrodes (important when considering processing and scale-up) but also minimises impurity formation in the structures. Using this pre-treatment to activate the CNTs can increase the specific capacitance by a factor of up to 2.5.[13, 14]

Despite the advantageous properties outlined, capacitance of CNT-based electrodes in practice has been somewhat disappointing. Capacitances for un-functionalised CNT electrodes have not surpassed 80 F g^{-1},[1,8, 15] and functionalised CNT electrodes usually have a specific capacitance of approximately 150 F g^{-1}.[10] A maximum capacitance of 180 F g^{-1} was obtained for SWNT in 7.5 M KOH at a discharge current of 1 mA cm^{-2} and resulting specific energy of 6.55 Wh kg^{-1},[16] - these capacitances are not exceptional, especially when the cost of synthesis/purchase is taken into account, as similar, or even higher capacitance can be obtained using activated carbon and milder electrolytes.[17] However this electrode did have an exceptional specific power of 20 kW kg^{-1}, which was obtained by heat treatment to 1000 °C which minimised the ESR to 51 mΩ.

It is likely that the main use of CNTs within supercapacitors will be as conductivity additives in devices as there are many reports of CNTs enhancing capacitance in pseudocapacitive electrodes where the conductivity of the material is otherwise a limiting factor to performance e.g. with Fe_2O_3 nanowires,[12] MnO_2,[18] VO_x,[19] In_2O_3 nanowires,[20] ZnO[21] and polypyrrole.[22, 23] This approach usually uses a low fraction amount of CNTs in comparison to the majority metal oxide ($< 5\%$) so the cost is minimised whilst maximising the conferred conductivity. This approach is discussed in more detail in section 2.5.3.

More recently, CNTs have been used as electrode materials for solid state supercapacitors, as the flexibility and porosity provided by the electrode structure is favourable when a solid (or gel) electrolyte is used.[24–28] This is discussed in more detail in Section 2.5.2

2.2.3 Graphene

Graphene has been explored as a possible candidate for supercapacitor electrodes. Graphene consists of a 2-D layer of carbon atoms with a high theoretical surface area of 2600 m^2 g^{-1} and although studied theoretically for nearly 60 years, was not discovered in its free state until 2004.[29] Graphene has shown reasonable capacitances of over 200 F g^{-1},[30] and excellent capacitance retention after many thousand cycles and at extremely high scan rates of over 10,000 mV s^{-1}.[31] However, due to the relative recent discovery, most research is in elementary stages and capacitive behaviour is likely to increase as knowledge of graphene's properties and fabrication techniques are improved. Most reports thus far have been based around developing the best synthesis and fabrication techniques, which have included electrophoretic deposition,[32] oxidation of graphite[33] and reduction of graphene oxides,[34] as well as the use of graphene oxide itself as an electrode material.[35] A graphene based supercapacitor has been prepared by reduction of graphene oxide by hydrazine[30] and produced an excellent specific energy of 28.5 Wh kg^{-1} for a symmetric 2-electrode device (corresponding specific capacitance of 205 F g^{-1}) in H_2SO_4. This was combined with a good specific power of 10 kW kg^{-1}; the combination of attractive energy and specific power in these reports combined with the potential for low cost, scalable synthesis[36, 37] suggests that graphene is likely to surpass the performance of CNTs as a supercapacitor electrode material.

Graphene nanosheets tend to re-stack when used as a monolithic electrode material[38] and as such there is much interest around reducing agglomeration and developing suitable co-materials that could hold open the layers, and therefore retain the mesoporosity of the material. This approach has been explored using carbon nanotubes as the structural additive, with 'pillars' of nanotubes separating layers of graphene

in a sandwich structure. This structure achieved a specific capacitance of 385 F g^{-1} by cyclic voltammetry at 10 mV s^{-1} in 6 M KOH,[39] and was attributed to the reduced agglomeration and subsequent increase in surface area from 202 m^2 g^{-1} to 612 m^2 g^{-1}, as well as some pseudocapacitance conferred from residual cobalt hydroxide catalyst from the CNT synthesis. Perhaps the most remarkable property of this arrangement is the *increase* in specific capacitance by 20% after 2000 cycles, which was thought to be caused by increased interfacial area between cobalt oxide and the electrolyte.

There is much scope for developments in graphene based electrodes as there are many different synthesis routes and, as the material is in its infancy, the best techniques are likely yet to come. There is current debate over whether graphene, which is more expensive and as mentioned has the structural problem of re-stacking, or graphene oxide which is cheaper and has shown higher capacitance thus far, is the best material to develop.[40]

Other carbon materials have shown good capacitive behaviour including carbide derivatives[4, 41] and nanofibers.[42] In depth information on the use of carbon materials for supercapacitor electrodes can be found in several extensive review papers.[43–45]

2.3 Electrode Materials - Pseudocapacitance

For a material to exhibit pseudocapacitance there must be at least two easily accessible redox states; usually these come in the form of a transition metal ion or the conjugated π cloud of a conducting polymer. The most well studied pseudoca-

pacitive material is RuO_2, however efforts have moved towards cheaper alternatives which could compete with carbon based materials on a commercial level. Electrodes based on pseudocapacitive materials usually display enhanced specific energy when compared to EDLCs, however the strains of intercalation and/or redox reactions tend to induce degradation and crumbling of the electrode structure, which in turn leads to capacity 'fading'.

2.3.1 Ruthenium and Manganese Dioxides - RuO_2/MnO_2

Ruthenium oxides have been widely studied for supercapacitor electrodes due to their theoretical highest capacitance of over 2000 F g^{-1} and an exceedingly high conductivity of $\sim 10^5$ S cm^{-1}, which approaches that of metals. Capacitance occurs due to electron hopping through the crystalline lattice coupled with adsorption at the surface of protons from the electrolyte (Equation 2.6), which is enhanced in hydrous ruthenium oxide ($RuO_2 \cdot xH_2O$):

$$Ru^{IV}O_2 + xH^+ + xe^- \longleftrightarrow Ru^{IV}_{1-x}Ru^{III}_{x}O_2H_x \tag{2.6}$$

There are several different redox states possible for a ruthenium ion, from Ru(I) to Ru(VIII), and these multiple states provide the high capacitance. The redox reactions occur during a voltage potential sweep at overlapping potentials so the cyclic voltammogram for RuO_2 looks more rectangular than most other pseudocapacitive materials, which usually show distinct peaks where the redox reaction is occurring. An example of rectangular RuO_2 cyclic voltammograms at different electrode masses is shown in Figure 2.3.

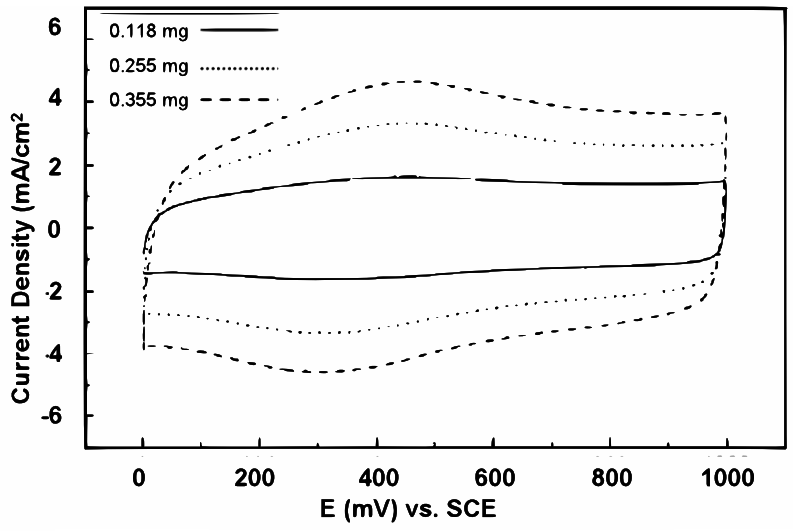

Figure 2.3: Cyclic voltammograms measured at 20 mV s^{-1} of $RuO_2 \cdot xH_2O$ electrodes in 0.5 M H_2SO_4 as a function of mass[46]

$RuO_2 \cdot xH_2O$ based electrodes can easily be synthesised with specific capacitances of approximately 650 F g^{-1}, for example by electrostatic spray deposition (ESD),[47, 48] which is a very effective synthetic method as it is low temperature, one-step and can produce stable, highly porous films with capacitances that are stable at cyclic voltammetry scan rates over 50 mV s^{-1}. Alternatively, the sol-gel technique produces materials with slightly higher capacitances and energy densities of approximately 750 F g^{-1} and 26.7 Wh kg^{-1}, however both capacitance and specific energy tend to drop more quickly at higher scan rates than ESD prepared electrodes.[49, 50] So far the highest capacitance for a pseudocapacitive material with no carbon or other conductivity enhancement is 1300 F g^{-1} obtained in an aligned $RuO_2 \cdot xH_2O$ nanotube electrode,[46] giving exceptional specific power and energy densities of 4320 kW kg^{-1} and 7.5 Wh kg^{-1} respectively - an specific energy comparable to commercially available activated carbon supercapacitors but with higher specific power. The remarkable performance was attributed to the morphology of the aligned nanotubes - synthesised with an aluminium oxide template - which simultaneously provided

super-efficient electron conduction and maximum electrolyte accessibility, and the presence of RuO_2 crystallites formed by thermal annealing.

In addition to high specific capacitance capabilities, RuO_2 is an attractive material in supercapacitor electrodes as it displays: high acidic stability - necessary as the electrolyte is usually H_2SO_4, good electrochemical stability and, unusually, very good proton diffusion.

RuO_2 however suffers from very high cost and is believed to be used only in niche military systems. Much work has gone into developing cheaper metal oxide systems that are inherently not as conductive as RuO_2 but much cheaper, both in the cost of the raw materials and the processing costs. The main challenge presented to pseudocapacitive research at the present time is the development of a capacitive electrode material that can match the performance of RuO_2 at a much lower cost.

In the search to find a cheap, high performance, scalable pseudocapacitive electrode material, attentions next turned towards MnO_2. MnO_2 devices have displayed good energy storage properties in other electrochemical systems such as batteries[51, 52] and fuel cells[53] and have the attractive properties of lower cost and toxicity than RuO_2 based devices. Usually combined with a carbon conductive additive, capacitances of over 200 F g^{-1} in a mild aqueous electrolyte (KCl) were quickly obtained.[54–56] Aqueous electrolytes are inherently safer than the usually flammable organic electrolytes in activated carbon systems, but operate at a lower voltage to avoid the hydrolysis of water.

The capacitive behaviour of MnO_2 arises from the many oxidation states of manganese, from Mn (II) through to Mn (VII) with a maximum theoretical capacitance of 1100 F g^{-1} for the Mn(IV) - Mn(III) transition, although experimentally difficult

to achieve. Although manganese has several accessible oxidation states, most of the redox transitions are not reversible enough to be utilised in pseudocapacitance, as fast charge/discharge, reversibility and cycle stability are vital properties of supercapacitors; practical capacitance tends to be due to the Mn(III) - Mn(IV) transition only. The cycle life of MnO_2 electrodes is affected by (a) manganese dissolution and (b) oxygen evolution - most devices show 20% reduction in specific capacitance after 1000 cycles and care must be taken not to drive the potential to a point where an irreversible transformation occurs. This limits the operating potential window of MnO_2 electrodes to 0 - 0.9 V vs. Ag/AgCl, again with knock-on effects to limit overall capacitance and power.

The mechanism of pseudocapacitance is proposed to arise due to the adsorption and insertion of metal alkali cations into the open, crystalline framework,[57] with the manganese ion in oxidation states (III) and (IV) for the oxidised and reduced forms (Equation 2.7) where X is the alkali metal cation, or a proton:

$$MnO_2 + X^+ + e^- \longleftrightarrow MnOOX \tag{2.7}$$

The pseudocapacitive mechanism was investigated in both thick and thin films by X-ray photoelectron spectroscopy and occurred only in the surface layer,[58] limiting capacitance to below 200 F g^{-1} when electrodes are prepared in the traditional way (doctor blade/rolling) into thick (>100 μm) films, plus conductive additives and binders. When the electrodes were prepared as thin films (<5 μm), eliminating the need for binders, exceptional capacitances of 1380 F g^{-1} were obtained, comparable to RuO_2. The preferred 'thin film' approach has thus been applied to many transition metal oxide electrodes and almost always gives increased capacitances per gram of active material.

2.3.2 Less well-studied oxides

There are intense efforts to develop low cost, high capacitance electrode materials using low cost transition metal oxides, mostly focussed on MnO_2. A brief outline of other materials that have attracted research interest are given below.

Iron Oxide - FeO_x

Iron has been suggested as a suitable oxide material for supercapacitor electrodes due to the inherent low cost, low environmental impact and ease of handling. Several forms of iron oxides have been studied, both crystalline and amorphous, and in single material electrodes and composites including: haematite (Fe_2O_3),[12, 59] goethite (FeOOH),[60] and magnetite (Fe_3O_4).[61–63]

Magnetite is of interest as it combines low cost with easily accessible redox states of iron in the corner sharing Fe^{2+}/Fe^{3+} inverse spinel crystal structure which leads to much higher conductivity (10^2 - 10^3 Ω^{-1} cm^{-1} *cf.* 10^{-9} Ω^{-1} cm^{-1} for Fe_2O_3/FeOOH). Magnetite initially showed a reasonable specific capacitance (when compared with other 'cheap' transition metal oxides) of 30 F g^{-1} in 0.1 M Na_2SO_3 when structured as a bulk electrode with activated carbon as a conducting additive.[63] Capacitance was improved in a nanoparticulate Fe_3O_4 film to 84 F g^{-1} in 1 M Na_2SO_4.[64] Further improvements involved synthesising thin film Fe_3O_4 by electroplating onto gold electrochemical quartz crystal microbalance (EQCM) plates, with a specific capacitance of 170 F g^{-1} in 1 M Na_2SO_3,[61] although the fabrication technique and substrate were clearly unsuitable for scale-up into practical devices.

The best overall performance of a predominantly Fe_3O_4 based electrode, of over 220

F g^{-1} at a discharge current of 0.1 mA cm^{-2} in 0.1 M Na_2SO_3 was achieved in an arrangement composed of high aspect ratio magnetite nanowires ($\sim$3 μm long, $\sim$100 nm diameter) coated with polypyrrole to enhance conductivity.[65] This is a significant increase in capacitance when compared with the unstructured, bulk, carbon containing electrodes previously studied (220 F g^{-1} *cf.* $\sim$30 F g^{-1}) and was attributed to the inter-twined, self-supporting, mesoporous network of nanowires that allowed maximum access of the electrolyte ions to the material alongside the conductivity enhancement brought about by low cost, environmentally compatible polypyrrole. All the materials involved were low cost and aqueous in nature, and the fabrication technique facile and at ambient conditions (see Section 3.3.2).

The specific capacitance of thin film Fe_3O_4 electrodes in different electrolytes (Na_2SO_3, Na_2SO_4, KOH) was studied[61] by cyclic voltammetry at 2 mV s^{-1} and was highly sensitive to the electrolyte anion involved, with sulphite (SO_3^{2-}) providing superior capacitance of 170 F g^{-1} compared with 25 F g^{-1} in 1 M Na_2SO_4 and 3 F g^{-1} in 1 M KOH and the cyclic voltammograms are displayed in Figure 2.4.

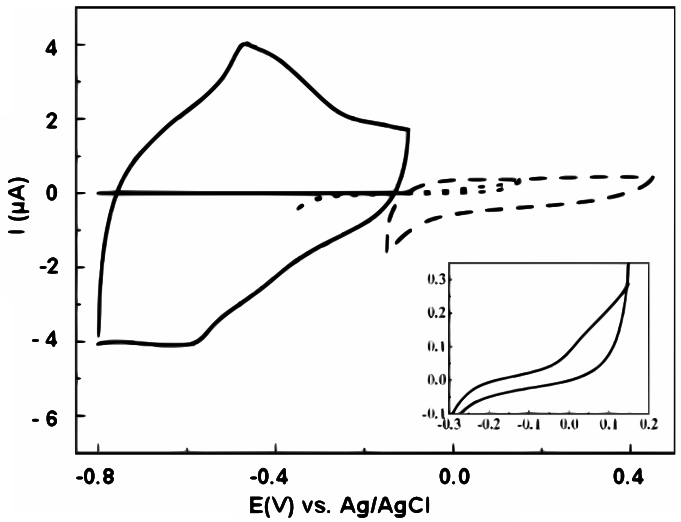

Figure 2.4: Cyclic voltammograms of Fe_3O_4 electrodes in 1 M Na_2SO_3 (solid line), 1 M Na_2SO_4 (dashed line) and 1 M KOH (dotted line)[61]

Strong adsorption of SO_3^{2-} onto the electrode surface was supported by electrochemical quartz crystal microbalance (EQCM) and XPS analysis. The adsorption of $SO_3{}^{-2}$ onto Fe_3O_4 provided capacitance due to the subsequent redox reactions of the sulphite ions:

$$2SO_3^{2-} + 2H_2O + 2e^- \rightleftharpoons S_2O_4^{2-} + 4OH^- \tag{2.8}$$

$$S_2O_4^{2-} + H_2O + 2e^- \rightleftharpoons S_2O_3^{2-} + 2OH^- \tag{2.9}$$

$$S + 2e^- \rightleftharpoons S^{2-} \tag{2.10}$$

Note that in Equations 2.8-2.10 there is no explicit role for the Fe_3O_4 itself. Therefore, circumstantially it is suggested that Fe_3O_4 provides some 'catalytic' effect to stimulate the reduction of SO_3^{2-} and subsequent species, with an efficiency not seen with other transition metal oxides, or for Fe_3O_4 and other electrolyte ions. Speculatively, this may imply other transition metal oxide/electrolyte combinations that may show similar or enhanced behaviour.

There have been increasing numbers of reports of Fe_2O_3[66]/FeOOH[67]/Fe_3O_4[68] based electrodes using a basic KOH/NaOH/LiOH electrolyte with charge storage attributed to surface cation intercalation combined with $Fe^{2/3+}$ redox reactions,[69] and typical capacitance values of 150 - 200 F g^{-1}. A combination of Fe_2O_3 with carbon gave a high capacitances of 315 F g^{-1} at a scan rate of 2 mV s^{-1} however, the capacitance faded to below 100 mV s^{-1} at relatively low scan rates of 25 mV s^{-1} and the cycle testing at a high current density of 10 A g^{-1} may mask the destructive effect of intercalation occurring at slower rates.

Nanowire Fe_3O_4-based electrodes[65] and similar results demonstrate that to compete with the ultrahigh specific capacitances of RuO_2 and MnO_2 based electrodes, novel fabrication techniques and a fuller understanding of the Fe_3O_4 charge storage mechanism is required.

Iron oxide as a lithium battery anode

Because of the high theoretical capacity of lithium intercalation into Fe_2O_3 and Fe_3O_4 compared to the most commonly used graphite (372 mAh g^{-1}), iron oxide electrodes have been investigated as a potential replacement anode in a lithium-ion battery. Initially, it was thought that the lithium insertion reaction was irreversible, however it was shown that by reducing Fe_2O_3 particle size from $\sim$0.5 μm to $\sim$20 nm,[70] intercalation became reversible as the smaller particles were able to accommodate the large volume changes involved without the onset of irreversible phase changes from hexagonal to cubic close packed.

Iron oxide has been successfully fabricated in combination with carbon nanotubes[71–74] and graphene[75–77] as well as the more common conductivity additives of carbon/acetylene black. The influence of conductivity additives has be shown to be the formation of a more homogeneous and thin solid electrolyte interphase (SEI) layer[78] which improves rate performance and can improve structural integrity.

A wide range of capacities are reported for FeO_x electrodes, from $\sim$400 mAh g^{-1},[75, 79–81] up to reversible capacities of over 1000 $mAhg^{-1}$ for Fe_2O_3 electrodes.[82, 83] It is important to consider both the number of cycles tested, and the rate for the capacity quoted, as a 0.1 rate will give a much higher capacity than C, however such low discharge currents may not be representative of a real-life device.

Nickel oxides - NiO

Energy storage behaviour has been observed for nickel oxides in the form of NiO and $Ni(OH)_2$ with respective redox reaction mechanisms of:

$$Ni(OH)_2 + OH^- \rightleftharpoons NiOOH + H_2O + e^- \tag{2.11}$$

$$NiO + OH^- \rightleftharpoons NiOOH + e^- \tag{2.12}$$

The NiO reaction mechanism is a surface-located, pseudocapacitive reaction whereas the $Ni(OH)_2$ mechanism involves proton intercalation[84] and so the process is controlled by bulk, solid, diffusion of protons. As such, NiO is a more appropriate electrode material for supercapacitors as the cycle life should be superior and $Ni(OH)_2$ is often used as a battery electrode e.g. in NiCd and NiMH batteries.

NiO has a high theoretical capacitance of 2573 F g^{-1} but experimental studies have generally shown much lower capacitance in practice due to the low conductivity of NiO (10^{-1} Ω^{-1} cm^{-1}). Initially, reasonable capacitances of 227 F g^{-1} in 1 M KOH were obtained for single-electrode NiO deposited electrochemically from solution at 4 mA cm^2,[85] a similar performance was shown for NiO synthesised by a sol-gel method (256 F g^{-1})[86] and electrostatic spray deposition (251 F g^{-1}).[87]

The ~250 F g^{-1} 'barrier' for NiO has been broken by careful structuring of the electrode at the nanoscale with these 'model' NiO electrodes showing 710 F g^{-1} at 1 A g^{-1} with 98% retention after 2000 cycles and up to 4 A g^{-1} (525 F g^{-1}).[88] These nanostructured electrodes were fabricated by a low temperature, template free (and therefore low-cost) method in which hierarchical micro/mesoporous structures were

formed through aqueous self-assembly followed by Oswald ripening. The hierarchical structures were able to reduce the diffusion length for electrolyte ions that accounted for the high specific capacitance and its retention.

Another technique used to boost the achieved capacitance of NiO electrodes is the manufacture of composite electrodes with nanostructured conductivity additives which helps to increase conductivity both through the electrode and to the current collector. NiO composite electrodes with carbon nanotubes[89–92, 92] have achieved varying capacitances between 250 - 750 F g^{-1} and with graphene[93–96] of 500 - 600 F g^{-1}, with a reduced graphene oxide/NiO electrode manufactured by co-precipitation and slurry/casting achieving a capacitance of 770 F g^{-1} at a scan rate of 2 mV s^{-1} with 96% retention after 1000 charge/discharge cycles.

Cobalt oxides - CoO_x

Cobalt oxides are becoming increasingly popular as candidates for supercapacitor electrodes as they have reasonable electrical conductivity. The first report of encouraging capacitative behaviour involved amorphous CoO_x xerogels prepared via a sol-gel technique.[97] Before this, limited capacitances were ascribed to the low surface area of the prepared oxides; calcining xerogels at 150 °C produced a surface area of 198 m^2 g^{-1} and specific capacitance of 291 F g^{-1} in 1 M KOH, measured by cyclic voltammetry at 5 mV s^{-1}. The most important synthetic parameter was the calcining temperature that had a significant effect on the surface area and pore volume of the resulting material, and subsequently the specific capacitance.

Morphological nanostructuring of loosely packed crystalline Co_3O_4 nanoparticles (3 - 15 nm diameter) produced capacitances ∼40% higher than those achieved in the

calcined xerogels, reaching 401 F g^{-1} in 1 M KOH.[98] The fabrication route simply involved the 'painting' of a slurry of Co_3O_4, acetylene black for conduction, and binder material onto the substrate. The electrode structure was said to be 'loosely packed' with a maximum surface area of 212 m^2 g^{-1} determined by sorption analysis. However, as in many cases (where actually stated in the paper), the surface area was measured on the as-prepared Co_3O_4 powder, not from the processed electrode. In general it is safe to assume that the ion accessible surface area per unit weight in the fabricated electrode will be significantly less than in the feedstock powder - a point rarely alluded to, even in the highest profile and most-cited, which is surprising given the importance of surface area in supercapacitors. Discussions with other scientists in this area suggest that accessible surface area may be reduced by ∼50% in fabricated electrodes, and there are significant experimental details in defining this in practice.

Vanadium Oxides - V_2O_5

V_2O_5 has been suggested as a strong candidate for low cost capacitors as it has readily available oxidation states and displays good capacitive behaviour in a mild aqueous electrolyte (KCl)[99] where the K^+ ions in electrolyte solution undergo ready intercalation and deintercalation.

The best performance of V_2O_5 within a supercapacitor has come from a full-cell supercapacitor comprised of an activated carbon anode and $V_2O_5 \cdot 6\,H_2O$ nanoribbon based cathode in 0.5 M K_2SO_4 to give an excellent specific energy of 29 Wh kg^{-1}. The specific power was calculated from the measured specific capacitance of 130 F g^{-1} for the $V_2O_5 \cdot 6\,H_2O$ electrode (64 F g^{-1} for the whole device) and a wide operating voltage of 0 - 1.8 V vs. SCE. This asymmetric supercapacitor arrangement

is attractive as it achieves a high specific energy using a mild, aqueous electrolytes, low cost electrode materials and a wide operating potential.

2.4 Device processing

As the development of pseudocapacitive devices is immature in terms of commercialisation, many fabrication techniques reported in the literature are low-tech, usually involving 'painting' a slurry of the active material, carbon-based conductor, and a binder material onto the current collector plate.[100] Although this approach has proven to be capable of high specific capacitance devices in many cases, for both EDLCs[100] and pseudocapacitors,[98] there are numerous arguments for the development of more sophisticated processing techniques. Firstly, the slurry/painting fabrication provides no control of the structure of the electrode at the micro or nano-scale. As discussed further in Section 2.5.1, highly porous electrodes with control of the morphology, porosity and structure at the nanoscale will be vital in the 'quest' towards devices with high energy densities and this level of control is not possible with such a rudimentary fabrication technique. Secondly, as energy and power densities are typically measured per gram (of active material in papers, of device in real systems) it is likely that thin film devices will be the most successful, as they allow the highest accessible surface area per weight of material, reducing the amount of weight 'wasted' in bulky thick films by inaccessible active material. The slurry/painting technique is demonstrated schematically in Figure 2.5 and typically produces films of 100 μm $\rightarrow$ mm thickness whereas it can be sensibly proposed that a better technique would be one that reproducibly fabricate films < 20 μm thick. However, the 'optimum' electrode thickness will likely be a strong function of the nature of the

mesoporosity controlling ion transport, conductivity controlling electron transport and the specific kinetics of the electrode/electrolyte system. There are no studies that identify such an optimum in terms of any of the above parameters.

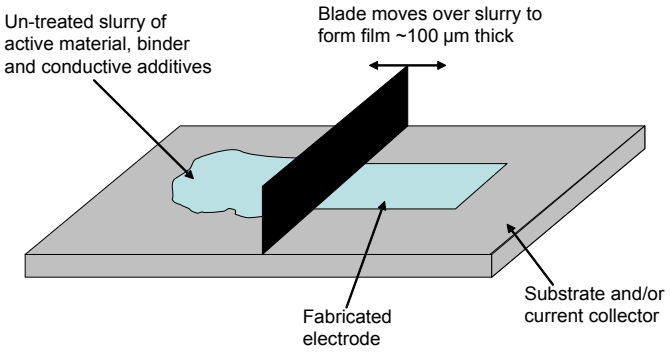

Figure 2.5: The doctor blade fabrication technique

More sophisticated techniques have started to be developed as the importance of the more strain tolerant, high surface area nanoscale morphology is realised, such as electrochemical alignment and templating of metal oxide nanorods,[101–103] electrodeposition[57] by potentiostatic cycling and electrostatic spray deposition.[47, 48] Most of these techniques are used to fabricate nanostructured electrodes on the cm^2 scale for small-scale electrochemical testing - careful thought must be taken as to the feasibility of scale up of these techniques if any of the results show promising qualities since commercial supercapacitors require 10 - 100 m^2 of current collector area.

Spray forming of nanostructured electrodes

A fabrication technique has been developed to produce nanostructured, porous electrodes that combine thin films with high levels of mesoporosity that promotes accessible surface area to electrolyte ions. The technique involves spraying a dilute suspension of nanostructured materials onto a heated substrate so that as the material deposits onto the substrate, the suspension medium almost immediately evaporates

and additionally, if the nanostructures have a high aspect ratio, they are able to tangle together to form an open, porous, self supporting network.[12, 65, 104] The process is shown schematically in Figure 2.6, with the heated substrate moving in the x-y plane to provide homogeneous coverage of areas 10's cm^2. Deposition occurs typically at low temperatures (< 120 °C) and atmospheric pressure and ideally with aqueous suspensions to minimises the cost of both materials and fabrication. In addition, it is applicable on both the small (cm^2) scale and on larger electrodes (m^2)

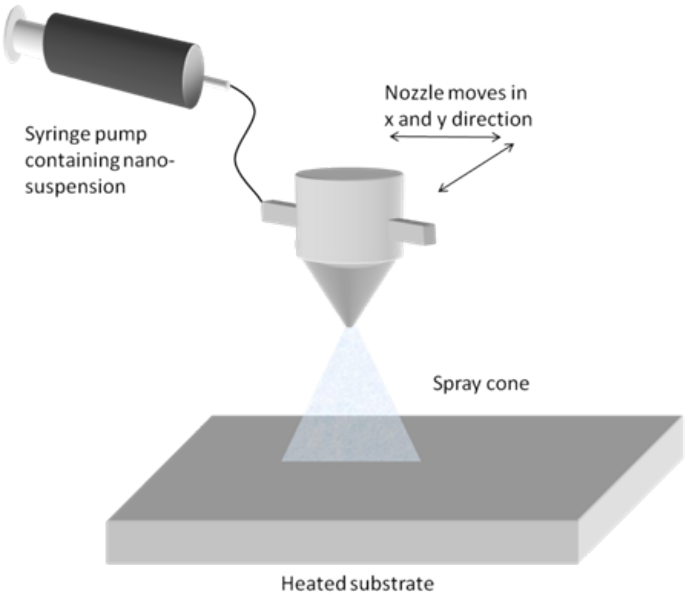

Figure 2.6: Spray deposition set up

The spraying technique has been successful with a range of different electrode materials, both EDLC and pseudocapacitive, and is currently being developed for application to other aspects of supercapacitor research; for example processing of stacked solid-state devices or high throughput manufacture of composite electrode material ratios.

2.5 Balancing specific energy and power

Although many advances have been made in the area of the supercapacitor electrode materials, it is, on the whole, carbon based devices that have progressed to market. The primary reason that few other materials have reached commercialisation is the inherent low specific energy combined with the high cost of materials other than carbon both in terms of: (1) raw materials, and (2) fabrication and assembly of full-cell devices. According to Equation 2.3 to increase specific energy, both specific capacitance and the voltage across which the device operates should be maximised. Similarly and according to Equation 2.4, for maximum specific power, the ESR should be minimised and again the voltage window maximised. However, the combination of these properties is not always facile and increasing the specific energy of electrodes often in turn reduces the specific power by undermining electrical conductivity, in effect turning a 'good supercapacitor' into a 'poor battery'. It is vital therefore to develop means to increase the specific energy supplied by supercapacitors whilst at the same time not compromising specific power. Reports in the literature are not always explicit in the parameters that are used to measure capacitance and specific energy - for full cell devices it is necessary to consider the mass of every part of the electrode, cell and packaging, and not just the mass of one active electrode material. Hence, materials that have been reported to have good capacitive properties measured according to the mass of electro-active material in half cell electrode versus a standard electrode (Section 2.2, 2.3) may prove to be low performing when, for example, binders, additives and substrates are taken into consideration and they are counterposed with another electrode in a full cell (device) arrangement. Techniques used to produce the highest performing devices, with the best energy/power balance are discussed below.

2.5.1 Nanostructured Electrodes

Although the concept of an 'electrochemical capacitor' has been around since the 1950s,[105] research based on supercapacitors has increased dramatically in the past decade. One reason for this is advances in 'nanotechnology' - as surface area is a key property of high performance supercapacitors, nanostructuring of electrodes can provide large increases in surface area, specific capacitance, and subsequent specific energy of devices.

Efforts towards highly porous carbon electrodes have shown that surface area on the nanoscale is an important factor, and that the balance between micro- (pores <2 nm), meso- (pores 2 - 50 nm), and macro- (pores >50 nm) porosity is a vital relationship and not as simple as one would intuitively assume.[45] It was thought that the electrolyte ions in solution were always surrounded by a solvent sphere (solvated ion), as in the outer Helmholtz layer, so the total number of ions held at the surface was dependent on the solvated ion diameter. However, by decreasing the average pore size within carbide-derived carbon materials, it was reported that the specific capacitance decreased until a turning point of a pore size of 1 nm was reached, after which capacitance (normalised to the BET surface area) dramatically increased from 5 μF cm^2 to nearly 15 μF cm ^{2} at 0.6 nm.[4] These results are shown graphically in Figure 2.7 with a comparison against previous studies. The increase occurred despite the average pore size being smaller than that of the solvated ion and was attributed to distortion in the solvation shell allowing ions to penetrate channels that previously had been thought too small. However, there is some scepticism in the supercapacitor community about the reproducibility and interpretation of this result.

Increased capacitance in nanostructured forms has been shown in most pseudocapac-

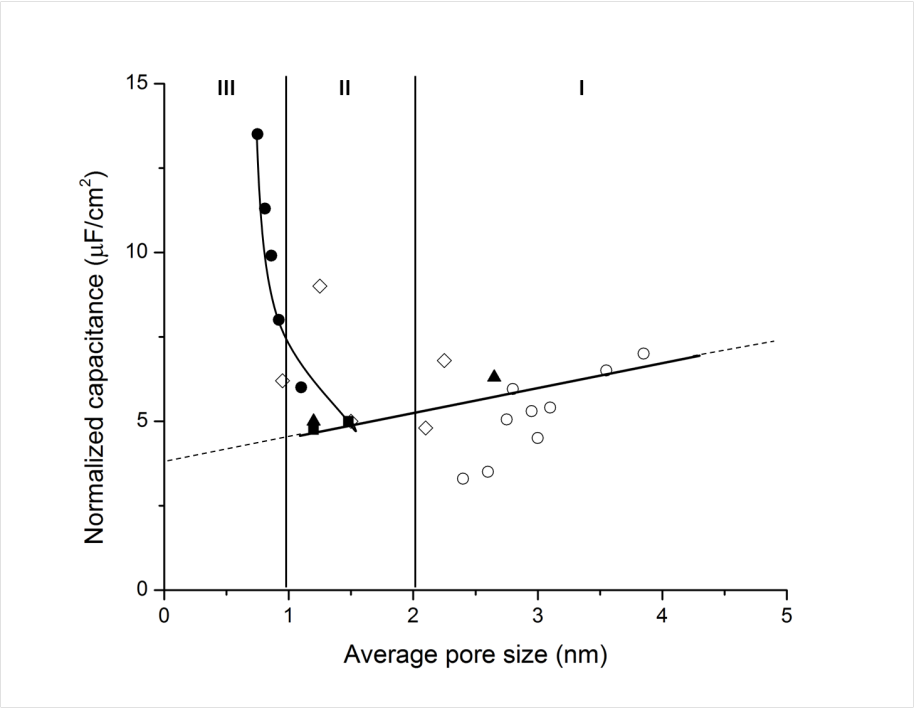

Figure 2.7: Specific capacitance normalized to BET surface area for new (filled circles) and previous (all other data points) . Reproduced from[4]

itive materials studied when compared with the micro/bulk. For example, a specific capacitance of 1300 F g^{-1} and specific energy of 7.4 Wh kg^{-1} was obtained by synthesising nanostructured hydrous RuO_2 tube by a hard templating method around an anodic aluminium oxide (AAO) membrane.[103] The mesoporous, 1D nanostructure was suggested to minimise the equivalent series resistance (ESR) and resulted in the high specific capacitance and a specific power of 4320 kW kg^{-1} with no carbon conductive additive necessary. The 1D nanostructure was thought to provide 'superhighways' for electron transport, minimising inter-particle resistance. Figure 2.8 shows how protons, or electrolyte cations can easily access a large surface area and transferred electrons are provided with a simple propagation route to the substrate/current collector.

There was a similar trend in nanostructured thin film Fe_3O_4 with specific capaci-

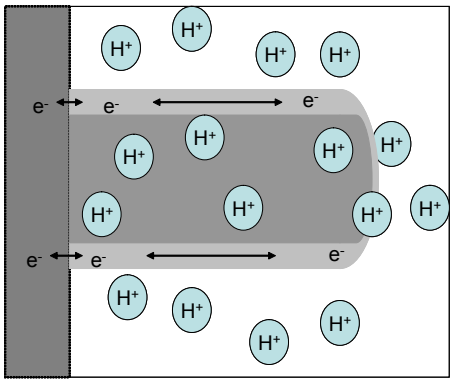

Figure 2.8: Representation of how 1D nanostructures can minimise resistance in electrodes[103]

tances of 106 F g^{-1} for 1D nanowires with no added conductive additive[65] and a substantial improvement over previous reports of 30 F g^{-1}[63] for unstructured, thick films that also required a carbon black additive to enhance conductivity. Higher aspect ratio forms of Fe_3O_4 had progressively higher capacitance, from 12 F g^{-1} for Fe_3O_4 nanoparticles, increasing slightly to 18 F g^{-1} for nanorods with a final dramatic increase to 106 F g^{-1} for the nanowires. Similarly to the RuO_2 electrode discussed above, this large increase in attributed to the facile electron transport along Fe_3O_4 nanowires, which minimised the ESR and so the low conductivity which had previously been a major issue in Fe_3O_4 electrodes was improved. However, interpretation is difficult as the extent of mesoporosity and therefore the surface area also varied.

Less well-studied metal oxides with lower overall capacitive properties show dramatic increases in specific capacitance when the electrodes are nanostructured. TiO_2 - previously considered non-capacitive - showed that by alignment into nanotubes compared with a conventional particulate powder slurry, a capacitance increase of nearly 400 % was achieved at a scan rate of 1 mV s^{-1} in 1 M KCl, from 181 to 911 μF cm^2.[101] This remarkable increase transforms TiO_2 from a barely-capacitive

metal oxide with low conductivity and typical capacitances of ∼10 - 40 μF cm^2 to a potentially attractive electrode material. It is worth noting that although TiO_2 is a metal oxide, the current-potential (CV) behaviour of the aligned TiO_2 nanotubes suggested that the increased capacitance was purely due to improved charge propagation and the charge storage was non-faradaic because the current density increased linearly with scan rate. Impedance spectroscopy measurements suggested that by increasing the aspect ratio and aligning the nanotubes, electrons were provided with simple charge propagation routes with minimal particle interface resistance. These titania results provided a strong suggestion as to how other materials that otherwise show with low conductivity may still offer interesting capacitive properties.

Synthesis of 1-D transition metal oxides

The synthesis of 1-D materials is now well-studied, as the enhanced electronic, mechanical and chemical properties of these nanomaterials can be applied to a wide range of areas from biomedical applications to electronics and energy storage.[106] In the case of supercapacitor electrodes, the increase in surface area when nanostructures are employed is an obvious advantage, but other advantages include the often enhanced conductivity of nanowires due to reduced particle junctions and the stability of the networks formed, which are often self supporting therefore reducing the need for binder material and the overall mass of the electrode.

There are several general techniques for the formation of 1D transition metal oxide materials:

- Hard templating
- Soft templating

- Self assembly through preferential growth of one crystal face
- Vapour phase growth
- Field alignment

Each technique has advantages and disadvantages and the success of each technique is usually dependent on the properties of the specific material in question. For the application of the various approaches for supercapacitor electrodes important factors to consider are: (1) the cost of synthesis, (2) the purity of the surface if templating is used and (3) the stability of the structures in the electrolyte.

2.5.2 Solid State Supercapacitors

A development in the processing of electrochemical capacitors has been the introduction of all-solid-state devices. Solid state capacitors are attractive because the removal of liquid increases the ease of handling and safety of the devices as there is a minimal chance of leaking or corrosion - reducing maintenance. Solid state electrolytes generally display enhanced thermal and chemical stability and operate over a wider potential window and temperature limits when compared with liquid equivalents. However, their major disadvantage is low ion mobility that undermines characteristic high specific power and high cost of the electrolyte.

There are several types of solid state electrolytes: (1) organic polymer hydro/aerogels e.g. PVA-H_2SO_4[100, 107] that allow certain cations to penetrate them and act as both a separator and electrolyte, (2) solvent cast/injected proton conducting polymer membranes e.g. Nafion/H_2SO_4;[108–110, 110] and (3) inorganic doped silica based gels[111] that can show the highest conductivity but are usually more expensive. 'Dry' solid

state electrolytes (i.e. aerogels) are generally safer than 'wet' gels (i.e. hydrogels), however they display a limited conductivity (*ca.* 10^{-8} S cm^{-1} compared with *ca.* 10^{-1} S cm^{-1}) and so hydrogel electrolytes are preferred since they display liquid-like conductivity at the same time as solid-like stability.

Most reports of all-solid-state devices have employed carbon based electrodes. A solid state supercapacitor with PANI coated CNT electrodes and H_2SO_4/PVA gel electrolyte was prepared with a specific capacitance of 350 F g^{-1} of active electrode materials and 31.4 F g^{-1} for a full cell device[100] - more than 6 times greater than any commercial device. The electrolyte had an extremely high conductivity of 1.73 x 10^{-1} S cm^{-1} and the full cell device was flexible and stable after over 1000 cycles. There was only a small reduction in the specific capacitance of 8% when compared with the same electrodes in 0.5 M H_2SO_4 solution. Several PANI/CNT/H_2SO_4/PVA devices were stacked together (to increase voltage to a maximum of 4 V) and used to light an LED bulb.

More recently, an all-sprayed, flexible solid state supercapacitor has been fabricated combining carbon nanotube/Nafion ionomer electrodes with a Nafion membrane electrolyte/separator.[28] Extremely high energy densities for a solid state device of 12.6 Wh kg^{-1} were obtained for a single electrode stack with a corresponding specific power of 3.3 kW kg^{-1}, which was attributed to the influence of the ionomer coating providing improved wetting/physical contact between electrode and electrolyte, and the spraying conditions which deposited additional protons throughout the electrode/ionomer membrane.

There are few reports of solid state devices with primarily metal oxide electrodes. However preliminary reports on RuO_2 electrodes with have shown capacitances as high as 1000 F g^{-1} with a PVA/PAA gel electrolyte and 1263 F g^{-1}[1112] for RuO_2

nanoparticles dispersed on TiO_2 nanotubes to maximise surface area in a PVA-H_3PO_4-H_2O electrolyte. Therefore the capacitance (and specific energy) of metal oxide electrodes is not necessarily limited by the use of gel electrolytes and solid state capacitors are not limited to carbon-based electrodes. Surprisingly, the RuO_2/TiO_2 devices had low internal resistances of 1.5 - 2 Ω and thus specific power is also not significantly reduced. This approach could be exploited to produce 'cheap' devices with high energy densities, especially if other, less costly metal oxides were used. If a processing technique was developed that could quickly, easily and cheaply produce many of these devices stacked on top of one another, a significant step forward could be made towards the production of a different class of commercial supercapacitor, for example for large scale grid electrical storage.

2.5.3 Hybrid Electrodes

As previously described, the combination of different materials within one electrode can be used to improve mechanical and electrochemical properties of the electrode, including stability, porosity and charge propagation (conductivity). This approach is most often used in pseudocapacitive electrodes where a carbon additive is used to increase conductivity. This is so common within the transition metal oxide area that most reports do not class the inclusion of carbon black additives as the formation of 'hybrid' electrodes and it is regarded as an inevitable requirement. The carbon fraction is not usually enough to provide any increased capacitance due to EDLC. However, in some cases the mixture of two or more materials is purposefully used to improve the characteristics of one or more of the materials involved.

Carbon Nanotubes and Pseudocapacitance

Increasingly, electrodes are being fabricated to exploit specifically the combination of EDLC and pseudocapacitance. For CNTs, decoration of the carbon wall with metal oxide nanoparticles is a popular approach as CNTs alone are unlikely to be performance and/or cost competitive, as mentioned in section 2.2.2. The combination of CNTs with a metal oxide can produce capacitances greater than either individual component. This effect was demonstrated in a system of MWNT decorated with ZnO nanoparticles.[113] The highest capacitance of MWNTs alone was 182.4 F g^{-1}; when a reasonable amount of ZnO nanoparticles was added (5 mins reaction time in ZnCl/HCl), capacitance was nearly doubled to 323.9 F g^{-1}. However, when the nanotubes were 'overloaded' with ZnO (20 mins reaction in ZnCl/HCl) the capacitance reduced to 49.6 F g^{-1}. The introduction of pseudocapacitance caused the initial increase in capacitance, however the resistance of the system greatly increased (from 0.6 Ω to 4.8 Ω) when the ZnO content was higher. Synergistic effects have also been reported for RuO_2 nanoparticles on oxygen functionalised MWNTs[114] and MnO_2 nanograins physically cross-linked with MWNTs.[115]

The structural benefits of using CNTs for conductivity was demonstrated in a CNT/PEDOT composite electrode where capacitances of 160 F g^{-1} were obtained at a scan rate of 2 mV s^{-1} with CNT/PEDOT compared with 127 F g^{-1} for acetylene black/PEDOT at the same scan rate. The PEDOT had a more homogeneous dispersion and therefore charge propagation was better.

Another approach is to combine 1-D (nanowire) metal oxides with CNTs, to form an inter-penetrating, co-tangled, open, mesoporous network of 1D nanostructured materials. The accessibility of all the electrode surface to the electrolyte ions is con-

sequently improved. This approach has been utilised for many metal oxide containing systems including In_2O_3,[20] V_2O_5,[116] Fe_2O_3,[12] MnO_2,[117] and TiO_2.[118]

Mixed transition metal oxides

Although transition metal oxides, excluding RuO_2, generally have poor conductivity, there have been examples where a metal oxide with higher conductivity has improved the capacitance of a poorly conducting metal oxide. SnO_2 nanowires have a maximum conductivity of 74 S cm^{-1} compared with bulk MnO_2 at 8 x 10^{-2} S cm^{-1} and nanostructured MnO_2 at 4.2 x 10^{-4} S cm^{-1}. Combination of SnO_2 nanowires coated with a thin film of MnO_2 exploited the good capacitive qualities of MnO_2 with the relatively high conductivity of SnO_2 to give a capacitance of 800 F g^{-1} at 1 A g^{-1} , specific energy of 35.4 Wh kg^{-1} and specific power of 25 kW kg^{-1}. This performance balance cannot be achieved using either material independently.

TiO_2 is another transition metal oxide used to enhance the capacitive properties of other oxides. In this case, the morphological structuring and stability of TiO_2 nanowires is often used to disperse other metal oxide nanoparticles and provide added conductivity to the electrode. TiO_2-V_2O_5 mixed oxide nanotubes have been synthesised into highly ordered arrays by anodization of Ti-V alloys.[102] Although pure V_2O_5 has shown promising capacitance behaviour (section 2.3.2), arrayed V_2O_5 nanowires can not easily be synthesised as V_2O_5 tends to be unstable in common electrolytes used for oriented growth. By incorporating V_2O_5 into TiO_2 nanostructures an specific energy of 20 Wh kg^{-1} was obtained alongside a specific capacitance of 220 F g^{-1}, with no significant decrease after 500 charge/discharge cycles and less than 30% loss in capacitance at the highest CV scan rate of 500 mV s^{-1}.

Mixing RuO_2 with other, less conductive metal oxides has been used to reduce the cost of RuO_2 electrodes without dramatically sacrificing the otherwise excellent capacitive properties. Mesoporous Co_3O_4/RuO_2 composite electrodes were prepared by co-precipitation and thermal annealing with a Ru concentration of 5, 10, 20 and 50 %.[119] As expected, the higher ruthenium content gave higher capacitance, however a 50% decrease in the ruthenium concentration would significantly reduce the relative cost (Co is itself considered expensive for energy storage applications), and very high capacitances of 642 F g^{-1} were maintained in the Co_3O_4/RuO_2 1:1 electrode in 1 M KOH.

2.5.4 Asymmetric Devices

As well as increasing the capacitance of the electrode materials, for example by maximising surface area, another strategy to increase the specific energy of supercapacitors is to increase the potential window across which the device performs. Equation 2.3 showed that doubling the voltage window across which the device performs increases the specific energy by a factor of 4. An increased voltage window can be achieved through the use of more expensive non-aqueous electrolytes, such as organic solvents[120] and room-temperature ionic liquids (RTILs)[121] so that electrolysis of water is avoided. The use of full cell devices comprising different electrode materials for the anode and cathode can also extend the overall operating voltage window to between the limits of the combined electrochemical windows. A full cell can be considered to be two capacitors in series, one at the cathode and one at the anode. Unfortunately therefore the specific capacitance of the combined device calculated from Equation 7.1 will always be lower than the capacitance of either electrode individually:

$$C_{tot} = \frac{C_{e1}.m_{e1}.C_{e2}.m_{e2}}{C_{e1}.m_{e1} + C_{e2}.m_{e2}} \tag{2.13}$$

where C_{e_x} is the specific capacitance of an individual electrode and m_{e_x} is the mass of the material. However this disadvantage can be offset by an increase in the electrochemical stability window.

A pseudocapacitive material with a non-faradaic (EDLC) material[115, 122–126] or electrodes of two different pseudocapacitive materials[127] was first demonstrated with a positive electrode of activated carbon counterposed against a Li intercalation negative electrode of $Li_4Ti_5O_{12}$, in $LiPF_6$ electrolyte.[128] The resulting electrochemical stability window was extended to 3 V. This approach has been subsequently demonstrated in aqueous based electrolyte systems.

Operating voltages of firstly 2.0 V[125, 126] in KCl then 2.2 V[129] in K_2SO_4 were obtained for devices consisting of a MnO_2 based positive electrode and an activated carbon negative electrode. These voltages are much higher than the operating potential available for the constituent electrodes (∼0.9 V each) in these aqueous electrolytes. The increase was due to the combination of the high hydrogen evolution overpotential for activated carbon and the high oxygen evolution overpotential for MnO_2. Figure 2.9 shows the overlapping cyclic voltammograms for activated carbon and MnO_2 in K_2SO_4 demonstrating how a combination of these two materials can extend the full device operating window. The devices had good stability and had energy densities of up to 29 Wh kg^{-1}, comparable with amorphous RuO_2 (∼28 Wh kg $^{-1}$) and over 4 times greater than currently available commercial carbon devices (∼6 Wh kg^{-1}).

To try and improve the specific energy of asymmetric devices, the combination of two

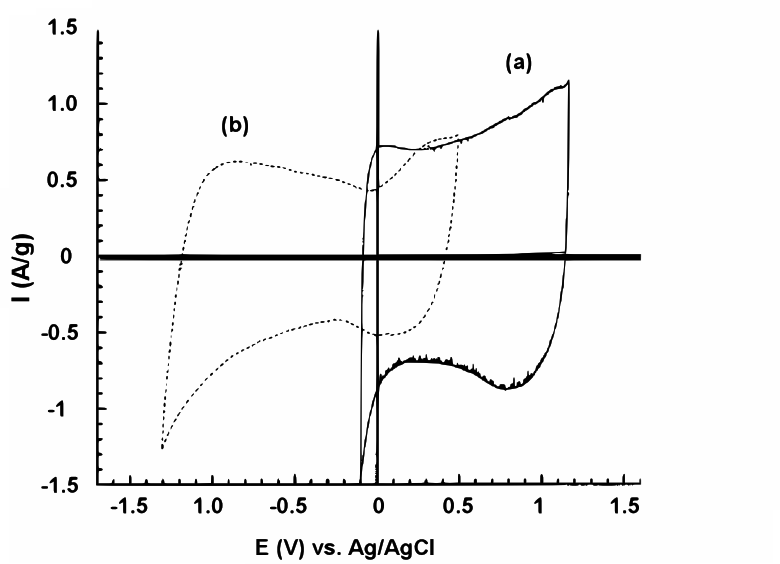

Figure 2.9: Cyclic voltammograms of (a) MnO_2 electrode and (b) activated carbon electrode in 0.65 M K_2SO_4 at 5 mV s^{-1}[129]

pseudocapacitive electrode is desirable as the overall cell capacitance is limited by the lower capacitance electrode (usually carbon). The first significant example of a capacitor with two pseudocapacitive electrodes consisted of a nanoparticulate MnO_2 cathode and Fe_3O_4 anode.[127] The specific capacitances of the individual materials in 0.1 M K_2SO_4 were 150 and 75 F g^{-1} respectively, with the specific capacitance of the combined device reaching 21.5 F g^{-1}, which is in approximate agreement with Equation 7.1. Despite the relatively low capacitance in the combined cell compared with the single electrodes an specific energy of 8.1 Wh kg^{-1} was achieved because the operating window was extended to 1.8 V, which is higher than for either of the individual materials of 1.2 V for MnO_2 and 0.9 V for Fe_3O_4. As the upper and lower potential limits were carefully controlled, there was no gas evolution and the configuration demonstrated that workable fully metal oxide supercapacitors may be feasible.

More recently, vanadium nitride (VN) has been used as a negative electrode with

a high capacitance and good cycle life with a β-$Ni(OH)_2$ positive electrode.[130] The capacitances of the individual electrodes were 580 and 680 F g^{-1} respectively and a full-cell capacitance of 126 F g^{-1} was achieved with corresponding energy and power densities of 26 Wh kg^{-1} and 2400 W kg^{-1}. However, the specific power fell to 365 W kg^{-1} when the specific energy was at a maximum of 50 Wh kg^{-1} which is indicative of the 'good supercapacitor or bad battery?' issue mentioned earlier. Additionally, the two-electrode experiments were performed in a glass cell with no separator which is not representative of a 'real-life' device and so the high energy densities may not be scalable.

Finally, approaches can be combined using hybrid electrodes in asymmetric full cells. For example the combination of metal oxide coated MWNT electrodes in 2 M KCl (MnO_2/MWNT positive electrode, SnO_2/MWNT negative electrode both at 1:1 wt ratio) gave a high specific energy of 20.3 Wh kg^{-1} at a corresponding specific power of 0.4 kW kg^{-1} and a slightly reduced specific energy of 10.2 Wh kg^{-1} and a high specific power of 6.5 kW kg^{-1}, as well as good charge retention after 1000 cycles (92%).[131] This attractive balance was attributed to the enhanced conductivity of the electrodes when compared with pure metal oxide/metal oxide devices.

A summary of some metal-oxide based hybrid devices is outlined in Table 2.1 and a Ragone plot comparing a range of energy and power densities for a sample of the asymmetric cells described is shown in Figure 2.10. Compared with the commercial supercapacitor specifications shown in Figure 2.10, academic reports usually have higher energy densities, however this comes at the expense of lower power densities than are currently commercially available. It is important to consider whether the power densities reported relate to the *maximum* possible power, calculated from Equation 2.4, or the experimental specific power which is calculated from real exper-

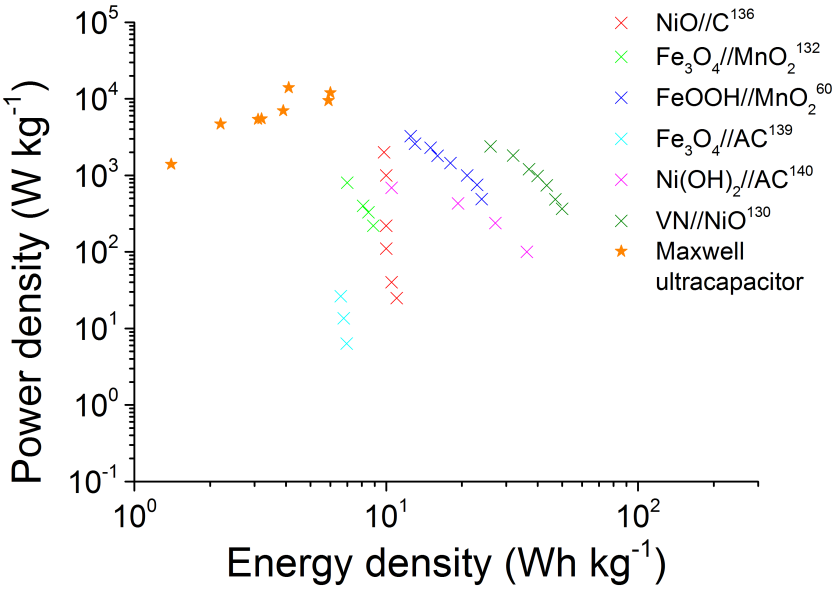

Figure 2.10: Energy and power densities for reported asymmetric configurations

imental data and covers a range of values according to the experimental parameters e.g. current density, scan rate.

The concept of hybrid/asymmetric full cells along with electrolyte options and nanostructuring/morphological control opens up a huge 'design space' for next generation supercapacitors. However, as ever, commercial impact will depend not only on performance but raw material costs and the availability of a scalable low cost process technology that provides the appropriate level of manufacturing control.

Ref	Cathode	Anode	Electrolyte	Voltage (v)	C_s (Fg^{-1})	Specific Energy) ($Wh\ kg^{-1}$)	Specific Power ($kW\ kg^{-1}$)	Cycles
[132]	MnO_2 NPs	Fe_3O_4 NPs	0.1 M K_2SO_4	0 - 1.8	21.5	8.1	10.2	5000
[132]	MnO_2 NPs	AC	0.1 M K_2SO_4	0 - 2.2	31.0	17.3	19.0	5000
[133]	δ-MnO_2 nanorods	AC	0.5 M Li_2SO_4	0 -1.8	31.0	17	2	23000
[62]	Fe_3O_4 NPs	AC	6 M KOH	0 - 1.2	37.9	7.6	0.07	500
[126]	amorphous MnO_2	AC	1 M KCl	0 - 2	50	20.8 - 28.8	0.5 - 8	100
[134]	amorphous MnO_2	AC	0.1 M K_2SO_4	0 - 2	21	10	16	195000
[135]	V_2O_5	AC	0.5 M K_2SO_4	0 - 1.8	64.4	20.3 - 29	0.07 - 2	100
[136]	NiO nanoflakes	porous carbon	6 M KOH	0 - 1.3	38	10	0.01 - 10	1000
[137]	$Ni(OH)_2$/MWNT	AC	6 M KOH	0 - 1.5	96	32	1.5	2000
[138]	MnO_2/porouscarbon	V_2O_5/MWNT	1 M Na_2SO_4	0 - 1.6	45	5.5 - 16	0.075 - 3.75	100
[131]	MnO_2/MWNT	SnO_2/MWNT	2 M KCl	0 - 1.7	38	20.3 - 10.2	0.4 - 6.5	1000
[60]	MnO_2	β-FeOOH nanorods	1 M Li_2SO_4	0 - 1.85	51	15 - 24	0.45 - 2	2000
[130]	NiO	VN	1 M KOH	0 - 1.5	140	26 - 50	2.4 - 0.37	1000
[139]	AC	Fe_3O_4	1 M KOH	0 - 1.2	38	-	-	500
[140]	AC	$NiOH_2$	6 M KOH	0 - 1.6	106	36.2	0.1	1000
[141]	$LiNi_{0.5}Mn_{1.5}O_4$	AC	1 M $LiPF_6$	0 - 2.8	32	55	-	1000
[142]	$LiMn_2O_4$	MnO_2/MWNT	1 M $LiClO_4$	0 - 2.5	60	26 - 56	0.3 - 2.4	-
[143]	$LiCoPO_4$ NPs	carbon nanofoam	1 M $LiClO_4$	0 - 2	21.9	11	0.2	1000
[144]	$LiMnO_4$/AC	$Li_4Ti_5O_{12}$	1 M $LiPF_6$	1.2 - 2.8	59	16	4	5000
[128]	AC	$Li_4Ti_5O_{12}$	1 M $LiBF_4$	1.5 - 3	-	85	-	5000
[145]	PFPT	$Li_4Ti_5O_{12}$ NPs	1 M $LiPF_6$	0 - 3	13	16	2.5	1500
[146]	AC	TiO_2	1 M $LiPF_6$	1.2 - 3.5	44	30 - 80	0.35	600
[118]	MWNTs	TiO_2 nanowires	1 M $LiPF_6$	0 - 2.8	11.5	8 - 12.5	0.3 - 1.2	600
[12]	MWNTs	Fe_2O_3/MWNTs	1 M $LiPF_6$	0 - 2.8	80	50	1	500

Table 2.1: A summary of the different asymmetric arrangements that have been investigated[147]

2.6 Summary

- The highest capacitance for monolithic pseudocapacitive electrodes were obtained for RuO_2 and MnO_2. To move the field forward, and away from these two well studied materials and attendant limitations, the combination of full understanding of capacitance mechanisms, new fabrication techniques and careful structuring of the electrodes is required. However sufficient data has been reviewed to suggest the tremendous potential for new supercapacitor arrangements providing a variety of energy, power, cyclability, toxicity and cost combinations.

- Careful interpretation of electrochemical, surface area and other data is necessary to ensure accurate comparisons can be drawn. This is true in particular when considering specific capacitance and specific energy when either the mass of simply the active material is used or whether substrates, binders, conductive additives and electrolytes are accounted for. Cycle life measurements are often taken with different parameters used to obtain capacitance and specific energy which will affect the accuracy of comparisons drawn. In some systems, even the most basic mechanisms for pseudocapacitance is not well-understood, and there is a general lack of generic modelling to underpin experimental data.

- For a new type of full cell electrochemical capacitor device to be brought to commercialisation, the specific energy of the cell must be maximised and the specific power must be retained so the fast, powerful charging and discharging behaviour characteristic of supercapacitors is not sacrificed. There are many techniques that are currently in development to exploit this relationship, and it is likely that the best performing, low cost full-cell device will be drawn

from the large design space afforded by an asymmetric capacitor with hybrid electrodes.

Bibliography

[1] Simon, P. and Gogotsi, Y. *Nat. Mater.* **7**(11), 845–854 (2008).

[2] Service, R. F. *Science* **313**(5789), 902–902 (2006). Service, Robert F.

[3] Vol'fkovich, Y. M. and Serdyuk, T. M. *Russ. J. Electrochem.* **38**(9), 935–958 (2002).

[4] Chmiola, J., Yushin, G., Gogotsi, Y., Portet, C., Simon, P., and Taberna, P. L. *Science* **313**(5794), 1760–1763 (2006).

[5] Kim, J., Shin, K., Jin, C., Kim, D., Kim, Y., Park, J., Lee, Y., Joo, Y., and Lee, K. *Electrochemistry* **69**(11), 853–857 (2001).

[6] Simon, P. and Burke, A. *Electrochem. Soc. Interface* **17**(1), 38–43 (2008).

[7] Baughman, R., Zakhidov, A., and de Heer, W. *Science* **297**(5582), 787–792 (2002).

[8] Futaba, D. N., Hata, K., Yamada, T., Hiraoka, T., Hayamizu, Y., Kakudate, Y., Tanaike, O., Hatori, H., Yumura, M., and Iijima, S. *Nat. Mater.* **5**(12), 987–994 (2006).

[9] Kaempgen, M., Chan, C. K., Ma, J., Cui, Y., and Gruner, G. *Nano Lett.* **9**(5), 1872–1876 (2009).

[10] Lee, S. W., Kim, B. S., Chen, S., Shao-Horn, Y., and Hammond, P. T. *J. Am. Chem. Soc.* **131**(2), 671–679 (2009).

[11] Niu, C. M., Sichel, E. K., Hoch, R., Moy, D., and Tennent, H. *Appl. Phys. Lett.* **70**(11), 1480–1482 (1997).

[12] Zhao, X., Johnston, C., and Grant, P. S. *J. Mater. Chem.* **19**(46), 8755–8760 (2009).

[13] Li, C., Wang, D., Liang, T., Wang, X., and Ji, L. *Mater. Lett.* **58**(29), 3774–3777 (2004).

[14] Jiang, Q., Qu, M., Zhou, G., Zhang, B., and Yu, Z. *Mater. Lett.* **57**(4), 988–991 (2002).

[15] Pushparaj, V. L., Shaijumon, M. M., Kumar, A., Murugesan, S., Ci, L., Vajtai, R., Linhardt, R. J., Nalamasu, O., and Ajayan, P. M. *Proceedings of the National Academy of Sciences of the United States of America* **104**(34), 13574–13577 (2007).

[16] An, K., Kim, W., Park, Y., Choi, Y., Lee, S., Chung, D., Bae, D., Lim, S., and Lee, Y. *Adv. Mater.* **13**(7), 497+ (2001).

[17] Chen, J. H., Li, W. Z., Wang, D. Z., Yang, S. X., Weng, J. G., and Ren, Z. *Carbon* **40**(8), 1193–1197 (2002).

[18] Zhu, G., He, Z., Chen, J., Zhao, J., Feng, X., Ma, Y., Fan, Q., Wang, L., and Huang, W. *Nanoscale* **6**(2), 1079–1085 (2014).

[19] Boukhalfa, S., Evanoff, K., and Yushin, G. *Energ. Enviro. Sci.* **5**(5), 6872–6879 (2012).

[20] Chen, P. C., Shen, G., Sukcharoenchoke, S., and Zhou, C. *Appl. Phys. Lett.* **94**(4) (2009).

[21] Zhang, Y. P., Sun, X. W., Pan, L. K., Li, H. B., Sun, Z., Sun, C. Q., and Tay, B. K. *J. Alloy. Comp.* **480**(2), L17–L19 (2009).

[22] Zhou, C. F., Kumar, S., Doyle, C. D., and Tour, J. M. *Chem. Mater.* **17**(8), 1997–2002 (2005).

[23] Kim, J. Y., Kim, K. H., and Kim, K. B. *J. Power Sources* **176**(1), 396–402 (2008).

[24] Pint, C., Nicholas, N., Xu, S., Sun, Z., Tour, J., Schmidt, H., Gordon, R., and Hauge, R. *Carbon* **49**(14), 4890–4897 (2011).

[25] Kang, Y., Chung, H., Han, C.-H., and Kim, W. *Nanotechnology* **23**(6) (2012).

[26] Gao, K., Shao, Z., Wang, X., Zhang, Y., Wang, W., and Wang, F. *RSC Adv.* **3**(35), 15058–15064 (2013).

[27] Hsia, B., Marschewski, J., Wang, S., In, J., Carraro, C., Poulikakos, D., Grigoropoulos, C., and Maboudian, R. *Nanotech.* **25**(5) (2014).

[28] Huang, C. and Grant, P. *Sci. Rep.* **3** (2013).

[29] Novoselov, K., Geim, A., Morozov, S., Jiang, D., Zhang, Y., Dubonos, S., Grigorieva, I., and Firsov, A. *Science* **306**(5696), 666–669 (2004).

[30] Wang, Y., Shi, Z., Huang, Y., Ma, Y., Wang, C., Chen, M., and Chen, Y. *J. Phys. Chem. C* **113**(30), 13103–13107 (2009).

[31] Mendoza-Sanchez, B., Rasche, B., Nicolosi, V., and Grant, P. S. *Carbon* **52**, 337–346 (2013).

[32] Chen, Y., Zhang, X., Yu, P., and Ma, Y. *J. Power Sources* **195**(9), 3031–3035 (2010).

[33] Du, X., Guo, P., Song, H., and Chen, X. *Electrochim. Acta* **55**(16), 4812–4819 (2010).

[34] Byon, H. R., Lee, S. W., Chen, S., Hammond, P. T., and Shao-Horn, Y. *Carbon* **49**(2), 457–467 (2011).

[35] Hsieh, C. T., Hsu, S. M., Lin, J. Y., and Teng, H. *J. Phys. Chem. C* **115**(25), 12367–12374 (2011).

[36] Lotya, M., Hernandez, Y., and Nicolosi, V. e. a. *J. Electrochem. Soc.* **131**(10), 3611–3620 (2009).

[37] Hernandez, Y., Nicolosi, V., Lotya, M., and Coleman, J. N. e. a. *Nat. Nanotech.* **3**(9), 563–568 (2008).

[38] Wang, D., Li, F., Wu, Z.-S., Ren, W., and Cheng, H. *Electrochem. Comm.* **11**(9), 1729–1732 (2009).

[39] Fan, Z., Yan, J., Zhi, L., Zhang, Q.and Wei, T., Feng, J., Zhang, M., Qian, W., and Wei, F. *Adv. Mater.* **22**(33), 3723+ (2010).

[40] Xu, B., Yue, S., Sui, Z., Zhang, X., Hou, S., Cao, G., and Yang, Y. *Energ. Environ. Sci.* **4**(8), 2826–2830 (2011).

[41] Arulepp, M., Leis, J., Latt, M., Miller, F., Rumma, K., Lust, E., and Burke, A. F. *J. Power Sources* **162**(2, SI), 1460–1466 (2006).

[42] Kim, C. *J. Power Sources* **142**(1-2), 382–388 (2005).

[43] Pandolfo, A. G. and Hollenkamp, A. F. *J. Power Sources* **157**(1), 11–27 (2006).

[44] Frackowiak, E. and Beguin, F. *Carbon* **39**(6) (2001).

[45] Gamby, J., Taberna, P., Simon, P., Fauvarque, J., and Chesneau, M. *J. Power Sources* **101**(1), 109–116 (2001).

[46] Kim, I. H. and Kim, K. B. *J. Electrochem. Soc.* **153**(2), A383–A389 (2006).

[47] Kim, I. and Kim, K. *Electrochem. Sol. St. Lett.* **4**(5), A62–A64 (2001).

[48] Kim, I. H. and Kim, K. B. *J. Electrochem. Soc.* **151**(1), E7–E13 (2004).

[49] Zheng, J. P. and Jow, T. R. *J. Electrochem. Soc.* **142**(1), L6–L8 (1995).

[50] Zheng, J., Cygan, P. J., and Jow, T. R. *J. Electrochem. Soc.* **142**(8), 2699–2703 (1995).

[51] Park, M. and Yoon, W. *J. Power Sources* **114**(2), 237–243 (2003).

[52] Komaba, S., Kumagai, N., and Chiba, S. *Electrochim. Acta* **46**(1), 31–37 (2000).

[53] Feng, R., Dong, H., Wang, Y., Ai, X., Cao, Y., and Yang, H. *Electrochem. Commun.* **7**(4), 449–452 (2005).

[54] Zhang, B. and Zhang, N. *Acta Phys.-Chim. Sin.* **19**(3), 286–288 (2003).

[55] Zhang, Z., Yang, B., Deng, M., Hu, Y., and Wang, B. *Acta Chim. Sin.* **62**(17), 1617–1620 (2004).

[56] Kim, H. and Popov, B. *J. Electrochem. Soc.* **150**(3), D56–D62 (2003).

[57] Pang, S., Anderson, M., and Chapman, T. *J. Electrochem. Soc.* **147**(2), 444–450 (2000).

[58] Toupin, M., Brousse, T., and Belanger, D. *J. Mater. Chem.* **16**, 3184–3190 (2004).

[59] Nagarajan, N. and Zhitomirsky, I. *J. Appl. Electrochem.* **36**(12), 1399–1405 (2006). Times Cited: 8.

[60] Jin, W.-H., Cao, G.-T., and Sun, J.-Y. *J. Power Sources* **175**(1), 686–691 (2008).

[61] Wang, S. Y., Ho, K. C., Kuo, S. L., and Wu, N. L. *J. Electrochem. Soc.* **153**(1), A75–A80 (2006).

[62] Du, X., Wang, C. Y., Chen, M. M., Jiao, Y., and Wang, J. *J. Phys. Chem. C* **113**(6), 2643–2646 (2009).

[63] Wang, S. Y. and Wu, N. L. *J. Appl. Electrochem.* **33**(3-4), 345–348 (2003).

[64] Pang, S. C., Khoh, W. H., and Chin, S. F. *J. Mater. Sci.* **45**(20), 5598–5604 (2010).

[65] Zhao, X., Johnston, C., Crossley, A., and Grant, P. S. *J. Mater. Chem.* **20**(36), 7637–7644 (2010).

[66] Wang, D., Li, Y., Wang, Q., and Wang, T. *J. Sol. St. Electrochem.* **16**(6), 2095–2102 (2012).

[67] Qu, Q., Yang, S., and Feng, X. *Adv. Mater.* **23**(46), 5574–5580 (2011).

[68] Guan, D., Gao, Z., Yang, W., Wang, J., Yuan, Y., Wang, B., Zhang, M., and Liu, L. *Mater. Sci. Eng. B* **178**(10), 736–743 (2013).

[69] Hallam, P., Gmez-Mingot, M., Kampouris, D., and Banks, C. *RSC Adv.* **2**(16), 6672–6679 (2012).

[70] Larcher, D., Masquelier, C., Bonnin, D., Chabre, Y., Masson, V., Leriche, J.-B., and Tarascon, J.-M. *J. Electrochem. Soc.* **150**(1), A133–A139 (2003).

[71] Seo, S.-D., Lee, G.-H., and Kim, D.-W. *J. Alloy. Comp.* (2014).

[72] Bak, B., Kim, S.-K., and Park, H. *Mater. Chem. Phys.* (2014).

[73] Seo, S.-D., Lee, G.-H., and Kim, D.-W. *J. Alloy. Comp.* (2014).

[74] Bak, B., Kim, S.-K., and Park, H. *Mater. Chem. Phys.* (2014).

[75] Zhao, B., Liu, R., Cai, X., Jiao, Z., Wu, M., Ling, X., Lu, B., and Jiang, Y. *J. Appl. Electrochem.* **44**(1), 53–60 (2014).

[76] Jang, B., Chae, O., Park, S.-K., Ha, J., Oh, S., Na, H., and Piao, Y. *J. Mat. Chem. A* **1**(48), 15442–15446 (2013). cited By (since 1996)1.

[77] Wang, J.-Z., Zhong, C., Wexler, D., Idris, N., Wang, Z.-X., Chen, L.-Q., and Liu, H.-K. *Chem-Eur. J.* **17**(2), 661–667 (2011).

[78] Zhang, W.-M., Wu, X.-L., Hu, J.-S., Guo, Y.-G., and Wan, L.-J. *Adv. Funct. Mater.* **18**(24), 3941–3946 (2008).

[79] Liu, H., Wexler, D., and Wang, G. *J. Alloy. Comp.* **487**(1-2), L24–L27 (2009).

[80] Wu, S., Wang, Z., He, C., Zhao, N., Shi, C., Liu, E., and Li, J. *J. Mater. Chem. A* **1**, 11011–11018 (2013).

[81] Di Lupo, F., Gerbaldi, C., Casino, S., Francia, C., Meligrana, G., Tuel, A., and Penazzi, N. *J. Alloy. Comp.* (2014).

[82] Xu, Y., Jian, G., Liu, Y., Zhu, Y., Zachariah, M., and Wang, C. *Nano Energy* **3**, 26–35 (2014).

[83] Jiang, Y., Zhang, D., Li, Y., Yuan, T., Bahlawane, N., Liang, C., Sun, W., Lu, Y., and Yan, M. *Nano Energy* **4**, 23–30 (2014).

[84] Nelson, P. and Owen, J. *J. Electrochem. Soc.* **150**(10), A1313–A1317 (2003).

[85] Nam, K. and Kim, K. *J. Electrochem. Soc.* **149**(3), A346–A354 (2002).

[86] Cheng, J., Cao, G. P., and Yang, Y. S. *J. Power Sources* **159**(1), 734–741 (2006).

[87] Nam, K. W. and Kim, K. B. *Electrochemistry* **69**(6) (2001).

[88] Yuan, C., Zhang, X., Su, L., Gao, B., and Shen, L. *J. Mater. Chem.* **19**(32), 5772–5777 (2009).

[89] Jia, W., Xu, M., Lei, C., Bao, S., and Jia, D. *Acta Chim. Sinica* **69**(15), 1773–1779 (2011).

[90] Su, A., Zhang, X., Rinaldi, A., Nguyen, S., Liu, H., Lei, Z., Lu, L., and Duong, H. *Chem. Phys. Lett.* **561-562**, 68–73 (2013).

[91] Mahmoudi, L., Mahboubi, F., and Yazdi, M. *Adv. Mater. Res.* **829**, 654–658 (2014).

[92] Dai, K., Liang, C., Dai, J., Lu, L., Zhu, G., Liu, Z., Liu, Q., and Zhang, Y. *Mater. Chem. Phys.* **143**(3), 1344–1351 (2014).

[93] Gao, F., Wei, Q., Yang, J., Bi, H., and Wang, M. *Ionics* **19**(12), 1883–1889 (2013).

[94] Wu, M.-S., Lin, Y.-P., Lin, C.-H., and Lee, J.-T. *J. Mater. Chem.* **22**(6), 2442–2448 (2012).

[95] Bu, Y., Wang, S., Jin, H., Zhang, W., Lin, J., and Wang, J. *J. Electrochem. Soc.* **159**(7), A990–A994 (2012). cited By (since 1996)5.

[96] Xia, X., Tu, J., Mai, Y., Chen, R., Wang, X., Gu, C., and Zhao, X. *Chem. Euro. J.* **17**(39), 10898–10905 (2011).

[97] Lin, C., Ritter, J. A., and Popov, B. N. *J. Electrochem. Soc.* **145**(12), 4097–4103 (1998).

[98] Cao, L., Lu, M., and Li, H. *J. Electrochem. Soc.* **152**(5) (2005).

[99] Lee, H. Y. and Goodenough, J. *J. Sol. St. Chem.* **148**(1), 81–84 (1999).

[100] Liu, Q., Nayfeh, M. H., and Yau, S.-T. *J. Power Sources* **195**(21, SI), 7480–7483 (2010).

[101] Salari, M., Aboutalebi, S. H., Konstantinov, K.and Jafelicci, M., and Liu, H. K. *Phys. Chem. Chem. Phys.* **13**, 5038–5041 (2011).

[102] Yang, Y., Kim, D., Yang, M., and Schmuki, P. *Chem. Comm.* **47**(27), 7746–7748 (2011).

[103] Hu, C. C., Chang, K. H., Lin, M. C., and Wu, Y. T. *Nano Lett.* **6**(12), 2690–2695 (2006).

[104] X., Z., C., H., Johnston, C., Dobson, P. J., and Grant, P. S. *Mater. Sci. Eng. B* **151**(2), 140–145 (2008).

[105] Becker, H. E. US patent 2800616 to General Electric Co.

[106] Kuchibhatla, S. V. N. T., Karakoti, A. S., Bera, D., and Seal, S. *Prog. Mater. Sci.* **52**(5), 699–913 (2007).

[107] Meng, C., Liu, C., Chen, L., Hu, C., and Fan, S. *Nano Lett.* **10**(10), 4025–4031 (2010).

[108] Lufrano, F. and Staiti, P. *Electroche. Sol. St. Lett.* **7**(11), A447–A450 (2004).

[109] Yin, Y., Zhou, J., Mansour, A., and Zhou, X. *J. Power Sources* **196**(14), 5997–6002 (2011).

[110] Choi, B., Hong, J., Hong, W., Hammond, P., and Park, H. *ACS Nano* **5**(9), 7205–7213 (2011).

[111] Matsuda, A., Honjo, H., Hirata, K., Tatsumisago, M., and Minami, T. *J. Power Sources* **77**(1), 12–16 (1999).

[112] Yong-gang, W. and Xiao-gang, Z. *Electrochim. Acta* **49**(), 1957–1962 (2004).

[113] Zhang, Y. P., Sun, X. W., Pan, L. K., Li, H. B., Sun, Z., Sun, C. P., and Tay, B. K. *Sol. St. Ionics* **180**(32-35), 1525–1528 (2009).

[114] Park, J. H., Ko, J. M., and Park, O. O. *J. Electrochem. Soc.* **150**(7), A864–A867 (2003).

[115] Wang, G. X., Zhang, B. L., Yu, Z. L., and Qu, M. Z. *Sol. St. Ionics* **176**(11-12), 1169–1174 (2005).

[116] Chen, Z., Augustyn, V., Wen, J., Zhang, Y. W., Shen, M. Q., Dunn, B., and Lu, Y. F. *Adv. Mater.* **23**(6), 791–+ (2011).

[117] Fang, Y. P., Liu, J. W., and Li, J. *J. Nanosci. Nanotechn.* **10**(8), 5099–5105 (2010).

[118] Wang, Q., Wen, Z. H., and Li, J. H. *Adv. Funct. Mater.* **16**(16), 2141–2146 (2006).

[119] Liu, Y., Zhao, W., and Zhang, X. *Electrochim. Acta* **53**(8), 3296–3304 (2008).

[120] Ricketts, B. W. and Ton-That, C. *J. Power Sources* **89**(1), 64–69 (2000).

[121] Lewandowski, A. and Galinski, M. *J. Phys. Chem. Sol.* **65**(2-3), 281–286 (2004).

[122] Raymundo-Pinero, E., Khomenko, V., Frackowiak, E., and Beguin, F. *J.Electrochem.Soc., volume = 152, number = 1, pages = A229-A235, year = 2005* .

[123] Park, J. H. and Park, O. O. *J. Power Sources* **111**(1), 185–190 (2002).

[124] Laforgue, A., Simon, P., Fauvarque, J. F., Sarrau, J. F., and Lailler, P. *Journal of the Electrochemical Society* **148**(10), A1130–A1134 (2001).

[125] Khomenko, V., Raymundo-Pinero, E., and Beguin, F. *J. Power Sources* **153**(1), 183–190 (2006).

[126] Hong, M. S., Lee, S. H., and Kim, S. W. *Electrochem. Sol. St. Lett.* **5**(10), A227–A230 (2002).

[127] Brousse, T. and Belanger, D. *Electrochem. Sol. St. Lett.* **6**(11), A244–A248 (2003).

[128] Amatucci, G. G., Badway, F., Du Pasquier, A., and Zheng, T. *J. Electrochem. Soc.* **148**(8), A930–A939 (2001).

[129] Brousse, T., Toupin, M., and Belanger, D. *J. Electrochem. Soc.* **151**(4), A614–A622 (2004).

[130] Gao, Z., Zhang, H., Cao, G., Han, M., and Yang, Y. *Electrochim. Acta* **87**, 375–380 (2013).

[131] Ng, K. C., Zhang, S., Peng, C., and Chen, G. Z. *J. Electrochem. Soc.* **156**(11), A846–A853 (2009).

[132] Cottineau, T., Toupin, M., Delahaye, T., Brousse, T., and Belanger, D. *Appl. Phys. A* **82**(4), 599–606 (2006).

[133] Qu, Q., Zhang, P., Wang, B., Chen, Y., Tian, S., Wu, Y., and Holze, R. *J. Phys. Chem. C* **113**(31), 14020–14027 (2009).

[134] Brousse, T., Taberna, P. L., Crosnier, O., Dugas, R., Guillemet, P., Scudeller, Y., Zhou, Y., Favier, F., Belanger, D., and Simon, P. *J. Power Sources* **173**(1), 633–641 (2007).

[135] Qu, Q. T., Shi, Y., Li, L. L., Guo, W. L., Wu, Y. P., Zhang, H. P., Guan, S. Y., and Holze, R. *Electrochem. Comm.* **11**(6), 1325–1328 (2009).

[136] Wang, D. W., Li, F., and Cheng, H. M. *J. Power Sources* **185**(2), 1563–1568 (2008).

[137] Wang, Y. G., Yu, L., and Xia, Y. Y. *J. Electrochem. Soc.* **153**(4) (2006).

[138] Chen, Z., Qin, Y., Weng, D., Xiao, Q., Peng, Y., Wang, X., Li, H., Wei, F., and Lu, Y. *Adv. Funct. Mater.* **19**(21), 3420–3426 (2009).

[139] Du, X., Wang, C., Jiao, J., and Wang, J. *J. Phys. Chem. C.* **113**, 26432646 (2009).

[140] Huang, J., Xu, P., Cao, D., Zhou, X., Yang, S., Li, Y., and Wang, G. *J. Power Sources* **246**(0), 371 – 376 (2014).

[141] Li, H. Q., Cheng, L., and Xia, Y. Y. *Electrochem. Sol. St. Lett.* **8**(9), A433–A436 (2005).

[142] Ma, S. B., Nam, K. W., Yoon, W. S., Yang, X. Q., Ahn, K. Y., Oh, K. H., and Kim, K. B. *Electrochem. Comm.* **9**(12), 2807–2811 (2007).

[143] Vasanthi, R., Kalpana, D., and Renganathan, N. *J. Sol. St. Electrochem.* **12**(7-8), 961–969 (2008).

[144] Hu, X., Deng, Z., Suo, J., and Pan, Z. *J. Power Sources* **187**(2), 635–639 (2009).

[145] Du Pasquier, A., Laforgue, A., Simon, P., Amatucci, G. G., and Fauvarque, J. F. *J. Electrochem. Soc.* **149**(3), A302–A306 (2002).

[146] Brousse, T., Marchand, R., Taberna, P. L., and Simon, P. *J. Power Sources* **158**(1), 571–577 (2006).

[147] Zhao, X., Sanchez, B. M., Dobson, P. J., and Grant, P. S. *Nanoscale* **3**(3) (2011).

Chapter 3

Experimental Techniques

3.1 Materials synthesis

Nanostructuring of electrode materials has been shown to afford major improvements in supercapacitor performance,[1–3] as ion access and mobility may be improved and volumetric changes can be more easily accommodated. Electrodes with an open, porous nanostructure and/or tailored porosity are advantageous where high power is required and in this thesis are produced by combining spray processing for electrode manufacture (detailed in section 3.3.2) with 1-dimensional nanomaterials, as shown in Figure 3.1

Nanostructured transition metal oxide materials were synthesised through low temperature and therefore low cost hydrothermal synthesis that employed H_2O as the reaction medium, again helping towards the potential for scale up without the larger costs associated with solvent handling.

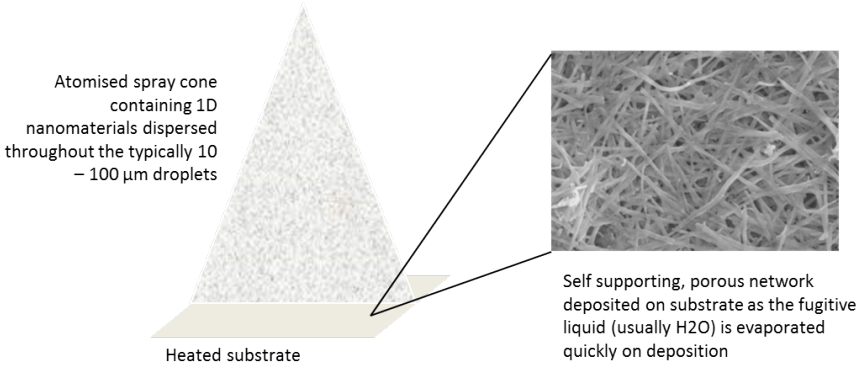

Figure 3.1: Schematic of how the suspension of a fine scale solid material dispersed in the atomised droplets forms an inter-mingled meso-porous electrode

3.1.1 Iron oxide 1D nanostructures

To synthesise iron oxide nanostructures with 1D morphology that will form network structures, it is necessary to accelerate growth in one crystallographic direction over others. This can be achieved through a combination of soft templating/surfactant effects, and controlling the pH, reaction time and temperature.

The synthesis used to produce the mixed-phase iron oxide nanowires used in Chapters 4 and 5 was modified from the literature,[4] and was as follow: 3.5 g $FeSO_4$ and 1.5 g $Na_2S_2O_3$ were added to 20 ml DI H_2O with stirring. Once a clear mixture had formed, 5.6 g poly(ethylene glycol) (PEG, $M_w = 4000$) was added and the mixture stirred for 15 minutes ensuring total dissolution and forming a viscous solution to which 7.0 g NaOH was gradually added, turning dark blue-black. The solution was transferred to a 120 ml teflon lined stainless steel autoclave and heated at 120 °C for 20 hours. After cooling, the supernatant was decanted and the brown/black solid washed with DI H_2O followed by centrifugation until pH = 7. Finally, the FeO_x powder was dried at 60 °C overnight. A single autoclave typically produced ∼1.5 g of iron oxide.

Before the optimum conditions for the synthesis were arrived at, a range of reaction conditions were investigated and resulted in a wide range of materials. Representative examples of the morphologies obtained and the corresponding experimental conditions are shown in Figure 3.2

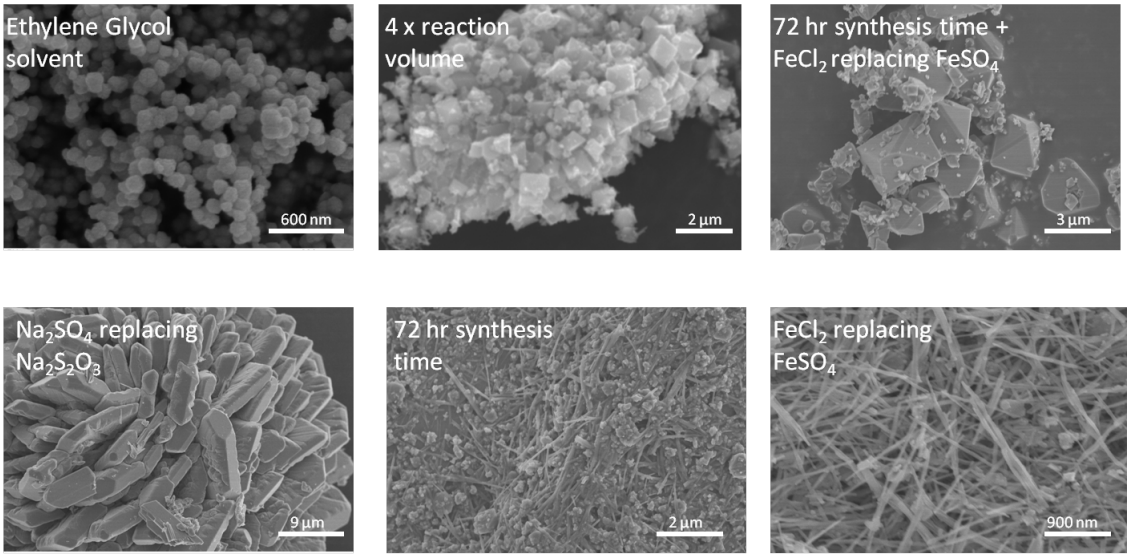

Figure 3.2: Iron oxide morphologies produced by altering hydrothermal synthesis reaction conditions, based on the approach in reference 4

3.1.2 Nickel oxide nanostructures

Nickel oxide (NiO) powders were synthesised using hydrothermal synthesis to form directly NiO, or $Ni(OH)_2$ that could be transformed to NiO through high temperature annealing:[5] 9.8 mmol NaOH was dissolved in 10 ml H_2O and 9.8 mmol $NiSO_4.7\,H_2O$ was dissolved in 30 ml H_2O. The NaOH solution was added dropwise to the $NiSO_4$ solution under magnetic stirring resulting in immediate precipitation of a pale blue solid. The mixture was transferred to a 120 ml teflon lined stainless steel autoclave and heated at 120 °C for 24 hours. After cooling, the resultant pale blue solid was collected, washed with DI H_2O until pH = 7 and dried in air overnight at 60 °C.

Finally, the powder was annealed at 400 °C in air for 2 hours for complete conversion to NiO. An autoclave typically produced ∼0.75 g of material.

3.1.3 Exfoliated graphene aqueous solutions

As described in Chapter 2, transition metals oxides such as those of Fe and Ni generally have low electrical conductivity and therefore additives are required for electrode applications, especially if high rate (high power) performance is required, which is a key characteristic of a supercapacitor. For iron oxide, multi-walled nanotubes were used from a commercial source (described later) and although carbon nanotubes were effective in producing a porous electrode structure with enhanced conductivity, it was not possible to form a stable suspension of carbon nanotubes in H_2O therefore nickel oxide used graphene prepared in-house according to a ultrasonic exfoliation technique.[6, 7] The exfoliation technique is suitable for the production of relatively large volumes of generally pristine graphene suspensions through low power ultrasonic exfoliation of graphite in a suitable medium. Exfoliation of the graphitic layers can occur spontaneously in specific organic solvents due to the matched surface charges of the solvent and graphene, while for this to occur in H_2O, a surfactant addition is necessary.

Aqueous solutions of exfoliated graphene were produced as follows: 1.5 g graphite was added to a 0.1% aqueous solution of sodium cholate (NaC, 500 ml) that had been stirred overnight to ensure a homogeneous suspension of NaC micelles. Low power sonication was carried out in a 150 W ultrasonic bath for 50 hours after which the mixture was left to settle for 24 hours. The resulting suspension was centrifuged at 1000 rpm for 90 minutes to remove residual graphite, and the supernatant graphene

solution decanted. Although it was possible to exfoliate graphite in organic solvents e.g. NMP without the need for surfactant, for low cost manufacture, safety and ease of handling during atomised spray deposition onto a heated substrate, an aqueous suspension of graphene was preferred.

3.2 Materials characterisation

3.2.1 X-ray diffraction

The crystal structure of as-synthesised and as-sprayed transition metal oxide powders were characterised using a Siemens D500 X-ray powder diffractometer with Cu K_α radiation ($\lambda = 0.154$ nm) in the 2Θ range from 10° to 100° at a scan rate of 0.05° s^{-1}. Incident X-rays are diffracted by electrons in the crystal structure at different scanning angles depending on electron (and therefore atom) location and so information about crystallinity, unit cell and particle size could be deduced from the resultant pattern.

3.2.2 X-ray photoelectron spectroscopy

XPS is a surface-specific technique used to characterise the materials chemistry of atoms/ions in a material by measuring the kinetic energy of electrons that are emitted from the top ∼10 nm of the sample when a beam of X-rays is incident. X-ray photoelectron spectroscopy (XPS) was performed in an ion pumped VG Microtech CLAM 4 MCD analyser system using 200 W unmonochromated Mg X-ray excitation. The analyser was operated at constant pass energy of 100 eV for wide scans and

20eV for detailed scans setting the C1s peak at BE 284.8 eV to overcome any sample charging. Data was obtained using SPECTRA version 8 operating system. Data processing was performed using CASAXPS. Peak areas were measured after satellite subtraction and background subtraction. Ion bombardment was undertaken using a Ar^+ VG2 ion gun operating at 5 kV.

3.2.3 Raman spectroscopy

Raman spectroscopy is a technique commonly used to characterise carbon-based materials through probing the vibrational and rotational modes of the atomic bonds.[8] A JY Horiba Labram Aramis imaging confocal Raman microscope was used to perform Raman spectroscopy with excitation emission from a solid state YAG laser source at $\lambda = 532$ nm (green). The resultant spectra were used to characterise graphene, and graphene-containing samples, where the relative intensity of various Raman modes can be used to deduce semi-quantitative insights into the defect population of the carbon materials.

3.2.4 UV-visible spectroscopy

UV-visible (UV-vis) spectroscopy of exfoliated graphene suspensions with exfoliation times of 30 mins to 100 hrs was performed using a Varian Cary 5000 UV-visible-NIR spectrometer. The optical spectra were used to calculate the concentration (c) of graphene platelets in the aqueous suspensions using the Beer-Lambert law at 660 nm:

$$A = \varepsilon * c * l \tag{3.1}$$

where the molar absortivity, ε, was pre-defined in the literature as 6600 L g^{-1} m^{-1},[9, 10] and the cuvette path length l was 1 cm.

3.2.5 Scanning electron microscopy

The morphology of materials as purchased, as-synthesised and after processing into thin-film electrodes was characterised by scanning electron morphology (SEM) using a field-emission gun (Jeol FESEM 840 F). Powders were attached to 15 mm stainless steel stubs using adhesive carbon tabs and electrodes were attached using conductive silver paste. To improve conductivity, all samples were sputter coated with a 2 - 3 nm layer of Pt using a Cressington 208 HR Pt/Au coater. Typical SEM experimental conditions were: a working distance of 15 mm, an acceleration voltage of 5 kW, a beam current of 1 - 2 x10^{-11} A and magnifications of x 25,000 - 100,000.

3.3 Electrode manufacture

By far the most common method for manufacture of electrodes in both the supercapacitor and battery field (academic and commercial) is slurry/casting/pressing. Despite its widespread applicability and high productivity, this method becomes progressively more difficult to control as the particle size reduces and especially as the aspect ratio deviates significantly from unity and viscosity increases, and where thin (<10 μm) electrodes are sought. A low cost, low temperature, convenient spray processing technique has been developed in the research group[10–12] that allows for thin film processing using nanomaterials even when the aspect ratio $\gg$1, along with control over electrode thickness, simply controlled by the spray time. The experi-

mental set-up is described below.

3.3.1 Suspension preparation

To facilitate spray atomisation rather than slurry casting, and to avoid clogging in the spray nozzle(s), stable and homogeneous nano-suspensions of the various materials were produced by ultrasonic agitation, where the precise conditions for sonication were dependent on the particular material involved. Two different ultrasonic equipments were used: a low-power (150 W / 42 kHz) Bransonic ultrasonic bath and a high power (750 W / 20 kHz) Sonics & Materials VCX750 probe. The amplitude, pulse time and sonication time were chosen depending on the material to be dispersed, and the fugitive medium. High power sonication was performed in a sound abating enclosure.

Iron oxide nanowires/multi-walled carbon nanotube co-suspensions were formed by high power sonication in EtOH for 5 minutes with a total solid concentration of 0.1 - 0.5 mg ml^{-1}. Due to the low surface tension and boiling point/flash point of EtOH, a solid ultrasonic probe was used and the mixture was encased in an ice bath.

Nickel oxide powders and nickel oxide/graphene mixtures were dispersed in H_2O at a concentration of 1 mg ml^{-1} using low power sonication for 30 minutes.

Carbon black powders required a 5 wt.% addition of PTFE to act as surfactant for a stable suspension to form. The suspension medium was NMP and the mixture was sonicated using the high power probe for 10 minutes in 30 s pulses with a 30 s break time to avoid overheating, along with an ice bath.

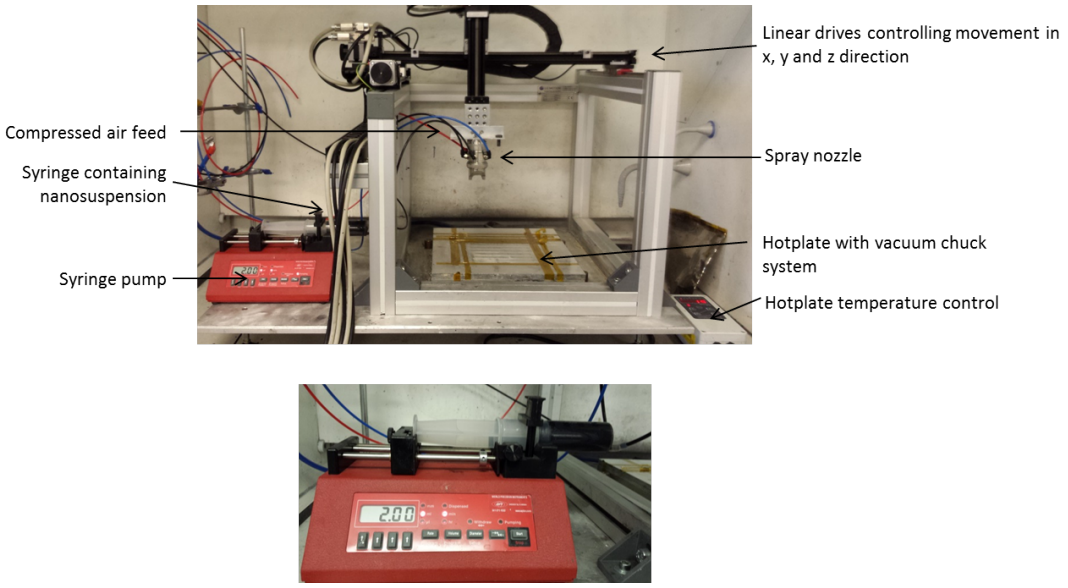

Figure 3.3: Spray processing experimental equipment (top) and close up of syringe pump (bottom)

3.3.2 Spray processing

Electrodes were manufactured by spray deposition of pre-prepared suspensions onto substrates heated to a temperature 5 - 20 °C higher than the boiling point of the suspension medium to effect almost immediate vapourisation of the fugitive liquid. Suspensions were pumped using a syringe pump with a controllable flow rate between 0.01 and 30 ml min^{-1} into a Viscomist atomising nozzle (Lechler, Germany). A detailed description of the nozzle specification and operation is given elsewhere.[13, 14] Suspensions were atomised in the nozzle using compressed air at 1 kPa and the apex of the resulting spray cone formed 10 cm above the heated substrate. The atomising air pressure and flow rate could be varied to give control over the spray cone density and angle to produce different film nanostructures. The spray processing equipment is shown in Figure 3.3 (top) with a close up of the syringe pump and syringe containing nanosuspension below.

During spraying, the nozzle moved alternately in the x any y direction at a speed between 10 and 100 mm s^{-1}. The size of the spray area was set to be at least 20 mm larger on all sides than the area to be covered to avoid edge effects. Due to the highly flexible nature of the spray equipment, it was possible to spray up to four different nanosuspensions simultaneously as two nozzles could be positioned side-by-side and each nozzle could accept two nanosuspensions. This approach allows for increase flexibility in the sprayed film arrangement of materials and properties e.g. by alternately spraying two materials with opposing surface charges layer-by-layer to increase film density.[15]

For nickel oxide and carbon black electrodes, in order to improve interfacial adhesion and electron transfer, a thin layer of polyethyleneimine (PEI) was deposited onto the substrate before the electrode material, with spray conditions: 0.1 % solution of PEI in H_2O, 0.5 ml min^{-1} flow rate, 10 cm nozzle height, 50 mm s^{-1} nozzle speed, 5 mm pitch, hotplate at 115 °C.

3.4 Electrode characterisation

3.4.1 Thickness and mass measurements

The thickness of sprayed electrodes was determined by step-height measurements using a Veeco Dektak 6M Surface Profiler. The mass of deposited material was measured by weighing the substrate before and after deposition using a Sartorius 5-figure microbalance.

3.4.2 Electrochemical cells

A three electrode cell arrangement was used to characterise electrochemical surface reactions, cycling stability and operating voltage window of individual sprayed electrodes. Reference electrodes were either Ag/AgCl, calomel (SCE) or hydroflex dependent on the electrolyte used and the counter electrode was a Pt coil or Pt coated Ti rod. Full-cell, two-electrode devices were tested in swagelok cells, coin cells and face-to-face arrangement which are described in more detail in Chapter 7. Battery cells were assembled in a glove box using standard coin cell casing, Li metal as counter and reference electrode, 0.3 mm Whatman glass fibre separator and $LiPF_6$ in a 1:1 mixture of ethylene carbonate:dimethyl carbonate as electrolyte.

Electrochemical testing was carried out at room temperature using a Gamry Reference 600 potentiostat. Electrochemical analysis and EIS fitting was performed on Gamry eChem Analyst software version 6.20 to accurately determine charge, capacitance and impedance values. Further details are given subsequently.

3.4.3 Cyclic voltammetry

Cyclic voltammetry (CV) is a dynamic technique that allows quantitative calculation of specific capacitance and kinetic analysis of electrochemical reactions. The potential of an electrode is varied in a linear fashion and the resulting current output measured, which allows the electrochemical stability voltage window to be determined, cycling stability to be tested, and electric double layer and redox reactions to be evaluated. Cyclic voltammetry was used to investigate the behaviour of sprayed electrodes in aqueous electrolytes at scan rates between 1 and 1000 mV s^{-1}. The volt-

age window was set by measuring the open circuit potential and hydrogen/oxygen evolution overpotentials in various aqueous based electrolytes.

Where only double layer charge storage occurred in the working electrode, the CV curves should have a rectangular/pseudo-parallelogram shape as the current response is constant over the entire potential window, and immediately reversed upon voltage switching. When an electrochemical reaction is able to occur at a specific electrode potential in a pseudocapacitive electrode, species on the electrode surface are oxidised/reduced resulting in an increase in current and a peak at a specific potential in the cyclic voltammogram. The peak current caused by a reduction/oxidation at an applied potential can be calculated according to the Randles-Sevcik equation as:[16]

$$I_p = 0.45(\frac{n.F.D.\nu}{R.T})^{\frac{1}{2}} n.F.A.c \tag{3.2}$$

where n is the number of electrons transferred, F is the Faraday constant, R is the gas constant, T is the temperature, A is the electrode area, D is the diffusion coefficient, c is the electrolyte concentration and ν is the scan rate

As the charge, $Q = C.V$ and $Q = \frac{\int I.dV}{\nu}$, specific capacitance C_s can be calculated from cyclic voltammetry curves according to:

$$C_s = \frac{\int I.dV}{2.m.\Delta V.\nu} \tag{3.3}$$

where $\int I.dV$ was the integrated area under both the anodic and cathodic sweep, m was the electrode material mass (including conductivity additives and binder, where

applicable), ΔV was the voltage window, ν was the scan rate and the factor of 2 accounts for the averaging across the anodic and cathodic scan.

3.4.4 Galvanostatic charge/discharge

Charge/discharge testing is used as a complementary technique to cyclic voltammetry in which a constant current is applied to the cell and the resulting voltage is measured as a function of time. Typical discharge times for supercapacitors are 1 - 100 s, which leads to the comparatively high power densities previously discussed. Charge/discharge testing more accurately describes the behaviour of a working supercapacitor device and so is preferred for calculating accurate capacitance and cycle life. Series resistance can be determined from the magnitude of the voltage drop as current switches (ΔI) at the beginning of discharge from $R = \frac{V_{drop}}{\Delta I}$.

Capacitance can be determined from the profile of a linear discharge slope by:

$$C_s = \frac{I.\Delta t}{m.\Delta V} \tag{3.4}$$

where I is the applied current, t is the discharge time, m is the total electrode mass and V is the voltage after any IR drop. Where pseudocapacitive reactions occur and the discharge curve is not linear, $\frac{\Delta t}{\Delta V}$ was approximated considering a corresponding linear discharge time and area under the discharge curve given by $\frac{2.\int V.dt}{\Delta V^2}$.

Individual electrodes were tested at charging and discharging currents between 0.1 - 100 Ag^{-1} for up to 1000 cycles. Two electrode devices were tested at charging and discharging currents between 0.5 - 10 mA for up to 1000 cycles. Charging potential

limits were set according to the characteristics of the electrode(s) being tested.

3.4.5 Potentiostatic electrochemical impedance spectroscopy

Electrochemical impedance spectroscopy (EIS) is a powerful technique that can be used to monitor electrode reactions over a wide range of frequencies that allows reactions with different time constants to be separated out in a non-destructive manner. A very small, oscillating A.C. potential is applied at a specified D.C. potential and the resulting current behaviour indicates the impedance of the cell at any particular frequency. As the potential oscillation is limited to a few mV, the current response can be considered linear and the cell to be under steady-state conditions so that $V = Z.i$ where V is the voltage, Z is the impedance and i is the current. The linearization of the system allows the cell to be described in terms of equivalent circuit components, from which various resistance, capacitance and inductance values can be estimated.

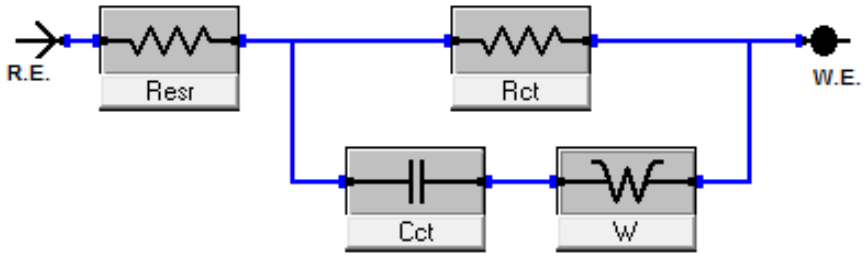

Figure 3.4: Randles' equivalent circuit

The most simple and commonly used equivalent circuit model for a supercapacitor electrode is the Randles circuit shown in Figure 3.4 where R_{ESR} is the combined resistance of the electrolyte and circuit components, R_{ct} is the charge transfer resistance, C_{ct} is the charge transfer capacitance and W is the 'Warburg' element which

accounts for diffusion to/from/through a porous electrode.

EIS was performed on two and three electrode cell in aqueous electrolytes at frequencies of 100,000 to 0.1 Hz at an A.C. voltage of 3 mV rms and various D.C. voltages.

Bibliography

[1] Zhao, X., Snchez, B., Dobson, P., and Grant, P. *Nanoscale* **3**(3), 839–855 (2011).

[2] Simon, P. and Gogotsi, Y. *Nature Materials* **7**(11), 845–854 (2008).

[3] Aric, A., Bruce, P., Scrosati, B., Tarascon, J.-M., and Van Schalkwijk, W. *Nature Materials* **4**(5), 366–377 (2005).

[4] He, K., Xu, C., Zhen, L., and Shao, W. *Mater. Lett.* **61**, 3159 (2007).

[5] Wang, Y., Zhou, D., Zhao, D., Hou, M., Wang, C., and Xia, Y. *J. Electrochem. Soc.* **160**(1), A98–A104 (2013).

[6] Lotya, M., Hernandez, Y., and Nicolosi, V. e. a. *J. Electrochem. Soc.* **131**(10), 3611–3620 (2009).

[7] Hernandez, Y., Nicolosi, V., Lotya, M., and Coleman, J. N. e. a. *Nature Nanotech.* **3**(9), 563–568 (2008).

[8] Ferrari, A. *Sol. St. Comm.* **143**(1-2), 47–57 (2007).

[9] Lotya, M., King, P., Khan, U., De, S., and Coleman, J. *ACS Nano* **4**(6), 3155–3162 (2010).

[10] Mendoza-Snchez, B., Rasche, B., Nicolosi, V., and Grant, P. *Carbon* **52**, 337–346 (2013).

[11] Zhao, X., Hinchliffe, C., Johnston, C., Dobson, P., and Grant, P. *Mat. Sci. Eng. B. Solid.* **151**(2), 140–145 (2008).

[12] Huang, C. and Grant, P. *Sci. Rep.* **3** (2013).

[13] Jiang, M. *Processing and Properties of Nanostructured Thin Film Energy Storage Devices*. PhD thesis, University of Oxford, (2013).

[14] Mendoza-Sanchez, B. *Synthesis of nanostructured materials and subsequent processing into nanometer-thick films for supercapacitor applications*. PhD thesis, University of Oxford, (2012).

[15] Huang, C., Grobert, N., Watt, A., Johnston, C., Crossley, A., Young, N., and Grant, P. *Carbon* **61**, 525–536 (2013).

[16] Girault, H. H. *Analytical and Physical Electrochemistry*. CRC Press, (2010).

Chapter 4

Enhancing the supercapacitor behaviour of Fe_3O_4/FeOOH nanowire hybrid electrodes in aqueous electrolytes

4.1 Introduction

Pseudocapacitive materials can provide an additional or alternative energy storage mechanism to electric double layer capacitance by making use of surface redox reactions or surface intercalation.[1] The most studied pseudocapacitive materials are the transition metal oxides RuO_2[2–4] and MnO_2,[5–8] although more recently there has been significant interest in other metal oxides such as CoO_3[9–11] and $Ni(OH)_2$.[12–15] Reports of the highest performing oxide-based electrodes generally rely on complex

and expensive materials synthesis, such as chemical vapour deposition and electrodeposition,[4, 16, 17] although commercially, slurry casting and rolling/pressing is used almost exclusively for electrode processing. Although highly productive and automated, slurry casting offers a comparatively restricted scope for control over electrode structure in electrode materials based on particulate materials with an aspect ratio >1 because slurry viscosity becomes problematical, or in the case of nano-scale materials, agglomeration effects dominate slurry rheology and casting behaviour.

Control over microstructure to maximise electrolyte accessible surface area and promote high ion mobilities is critical in developing attractive new supercapacitor materials that can compete with activated carbon based electrodes. Therefore, despite the attractive performance of current activated carbon electrodes when combined with non-aqueous, Li ion containing electrolytes that typically provide a capacitance of 100 - 200 F g^{-1} and almost unlimited cycle life, there is a continuing interest in complementary or alternative supercapacitor systems that combine both cheaper materials and safer, easy to handle and maintain aqueous electrolytes manufactured via routes that allow for practical scale up.

Iron oxide (FeO_x) is low cost, has low environmental impact, is easily contrived during synthesis into different morphologies, and in principle offers the potential for $Fe^{2+} \rightleftharpoons Fe^{3+}$ surface pseudocapacitive reactions in an aqueous electrolyte. However, the various types of iron oxide (Fe_3O_4, Fe_2O_3, FeOOH) have been relatively neglected as potential supercapacitor electrode materials because of their inherent high electrical resistance and apparent low cyclability. Suggested mechanisms of charge storage in iron oxide include redox pseudocapacitance[18–22] in Fe_3O_4 and intercalation in Fe_2O_3 and FeOOH[23–27] , although most reports allude to their somewhat limited

electrochemical double layer capacitance (EDLC) only.[28–30] Until the charge storage mechanisms in FeO_x in various electrolytes are better understood it will continue to be difficult to understand the real potential for iron oxide systems in supercapacitor applications, and therefore to realise more fully the potential advantages of these cheap and safe materials.

In this chapter, FeO_x and commercial carbon nanotubes were combined using a low cost, scalable spray processing technique to produce composite FeO_x-based thin-film electrodes with surprisingly high capacity performance. The spray process allows for the easy and intimate incorporation of commercially available multiwalled carbon nanotubes (MWNTs) as a minority phase to provide percolating electron pathways with FeO_x nanomaterials, with the resulting electrodes compromising an open macro/mesoporous network of inter-woven 1D FeO_x and MWNTs. Electrochemical testing in a variety of aqueous electrolytes is used to reveal the likely mechanisms underpinning charge storage behaviour, and to identify optimum FeO_x:MWNT ratios in the highest performing electrolyte.

4.2 Experimental Procedure

4.2.1 Synthesis of iron oxide nanowires

All materials were obtained from Sigma-Aldrich (UK) and used without further purification. FeO_x nanowires were synthesised by a modified hydrothermal technique described elsewhere:[31] 3.5 g $FeSO_4$ and 1.5 g $Na_2S_2O_3$ were added to 20 ml DI H_2O with stirring. Once a clear mixture had formed, 5.6 g poly(ethylene glycol) (PEG, M_w = 4000) was added and the mixture stirred for 15 minutes ensuring total dissolution

and forming a viscous solution to which 7.0 g NaOH was gradually added, turning dark blue-black. The solution was transferred to a 120 ml teflon lined stainless steel autoclave and heated at 120 °C for 20 hours. After cooling, the supernatant was decanted and the brown/black solid washed with DI H_2O followed by centrifugation until pH = 7. Finally, the FeO_x powder was dried at 60 °C overnight.

4.2.2 Preparation of iron oxide and carbon nanotube electrodes

MWNTs (Bayer) were purified by refluxing in H_2SO_4 for 6 hrs to remove residual graphitic particles then washed thoroughly with DI H_2O and dried at 60°C overnight. Electrodes were processed using novel spray processing equipment described elsewhere.[32–35] Briefly, FeO_x was suspended in EtOH at a concentration of 0.1 mg ml^{-1} by high power probe sonication for 10 minutes using a Sonics & Materials Vibra Cell VC750. MWNTs were then added and the mixture sonicated for a further 3 - 5 minutes until a stable suspension was formed. FeO_x:MWNT mass ratios of 100:1 to 1:2 were investigated, with the spray suspension route able to process readily the full range of nanomaterial mixtures. The suspension was sprayed onto 2 x 1 cm stainless steel substrates from a height of 10 cm until a mass of 0.25-0.35 mg was deposited. The thickness of the electrodes was 3 - 5 μm.

4.2.3 Material and electrode characterisation

Powder x-ray diffraction (PXRD) was performed in a Siemens D5000 powder diffractometer using Cu-Kα radiation with 0.15418 nm wavelength. X-ray photoelectron

spectroscopy (XPS) was performed in an ion pumped VG Microtech CLAM 4 MCD analyser system using 200 W unmonochromated Mg X-ray excitation. Electrode thickness was determined by step height measurements in a Dektak 6 M profilometer (Veeco Instruments Inc.). The mass of deposited material was measured by weighing the substrates before and after spraying using a five figure microbalance (Sartorius). Scanning electron microscopy (SEM) was performed in a JEOL JSM-840F operating at an acceleration voltage of 5 kV and beam current of 2 x10^{-11} A. Images were acquired using secondary and backscattered electrons for both as-synthesised materials and the sprayed electrodes.

4.2.4 Electrochemical testing

Electrochemical testing was performed using a Gamry Reference 600 potentiostat in a three electrode cell using a SCE reference electrode and a Pt coated titania counter electrode. Electrochemical tests were performed using 0.5 M Na_2SO_3, Na_2SO_4, Li_2SO_4 and KCl aqueous electrolytes. Cyclic voltammetry was performed in the potential range 0 to -1.1 V vs. SCE at scan rates 2 - 500 mV s^{-1}. Galvanostatic charge/discharge tests were performed at current densities of 0.5 - 10 A g^{-1}. Electrochemical impedance spectroscopy (EIS) measurements were obtained using an AC voltage of 5 mV rms and DC voltages of 0 to -1 V vs SCE in the frequency range 100 kHz - 0.01 Hz. Calibration experiments were performed to ensure there were no underlying reactions between the substrates and the electrolytes over the voltage range of interest. Specific capacitance values were reproducible to +/- 5 F g^{-1}

4.3 Results and discussion

4.3.1 Materials characterisation

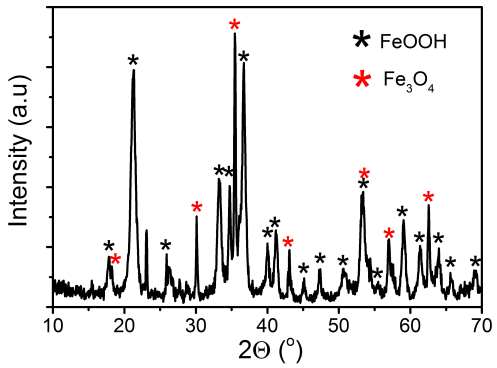

Figure 4.1: PXRD pattern from the as-synthesised FeO_x powder

The PXRD pattern of as-synthesised FeO_x powder (Figure 6.1) showed a mixed phase iron oxide crystal structure with highest intensity peaks for magnetite (Fe_3O_4) as well as lesser peaks for goethite (FeOOH). It was not possible to synthesis Fe_3O_4 only nanowires if, as desired, a 1D wire-like morphology was to be maintained. To investigate any surface specific segregation of phases, XPS was performed on as-sprayed FeO_x electrodes prior to any electrochemical testing. The Fe 2p region of the XPS spectrum (Figure 4.2) showed a peak at 711.87 eV that corresponded to Fe^{3+} in both Fe_3O_4 and FeOOH.[36] However, the lack of a Fe^{2+} XPS peak in the region of 710 eV along with the satellite peak at ~725 eV that would accompany Fe_3O_4 suggested that FeOOH dominated the surface phase chemistry.[36, 37] From the PXRD and XPS data it was concluded that the as-synthesised FeO_x powder was composed of co-axial arrangement of a largely Fe_3O_4 core with a substantially FeOOH surface layer.

SEM images of the as-synthesised FeO_x powder (Figure 5.2 (a)) showed nanowires

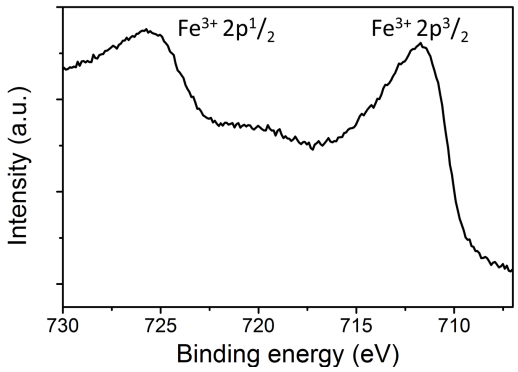

Figure 4.2: Fe 2p region in the XPS spectrum of the as-synthesised FeO_x powder

of length 5 -10 μm and width ~100 nm. As intended, the combination of PEG-4000 acting as a soft template and a high pH reaction medium forced the enhanced growth of the (100) crystal face of Fe_3O_4[31] producing a high aspect ratio that proved ideal for the formation of porous electrodes with inter-connected meso-porosity.

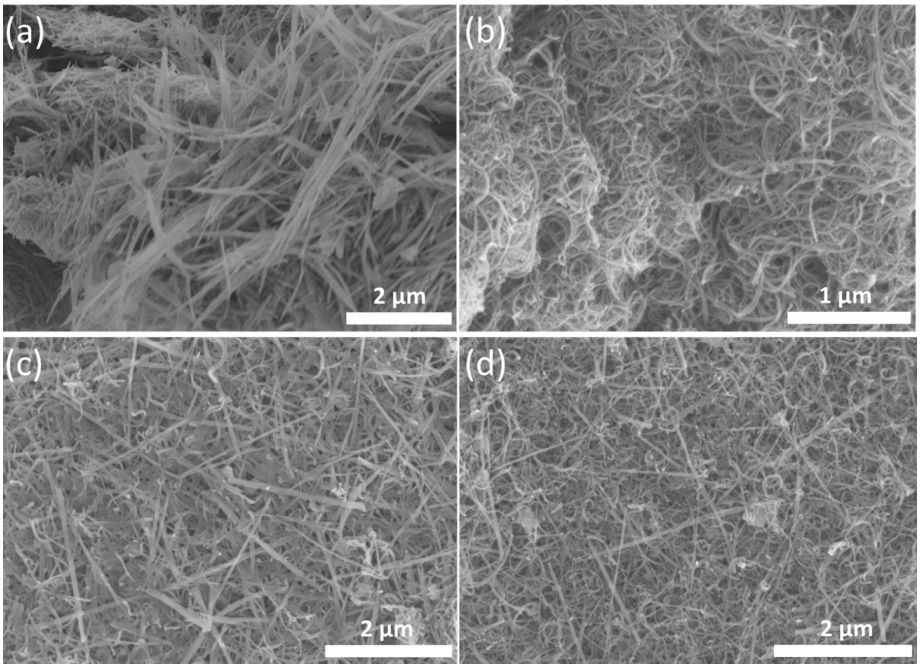

Figure 4.3: SEM images of: (a) synthesised FeO_x powder; (b) acid treated MWNTs; (c) a sprayed FeO_x/MWNT electrode (ratio 2:1); and (d) sprayed FeO_x/MWNT electrode (ratio 1:2)

The FeO_x and acid treated MWNTs are shown in Figures 5.2 (a) and (b) respectively. Figures 5.2 (c) and (d) show the as-sprayed electrodes containing FeO_x and MWNTs at a mass ratio of (2:1) and (1:2) respectively, in each case maintaining the porous, interconnected network. The combination of the two similarly sized 1D nanomaterials in suspension and at deposition caused the MWNTs to "tangle" with the FeO_x nanowires to form a macro/mesoporous, self-supporting network held together by friction, with no requirement for binder. The SEM images showed no significant morphological changes to either material due to high power sonication in suspension preparation, or due to the spray processing.

4.3.2 Electrochemical behaviour in Na_2SO_3

Cyclic voltammetry (CV) was used to investigate sprayed electrodes with FeO_x:MWNT ratios across the range from 10:1 to 1:2, as well as FeO_x only and MWNT only electrodes in a 3 electrode electrochemical cell containing 0.5 M Na_2SO_3. Specific capacitance C_s (F g^{-1}) was estimated from CV curves according to:

$$C_s = \frac{\int IdV}{2\nu m dV} \tag{4.1}$$

where $\int IdV$ is the integrated area under the CV curves, I is the current (A), ν is the scan rate (mV s^{-1}), m is the total mass of deposited electrode material (g) and dV is the CV voltage window.

Figure 4.4 (a) shows that when no MWNTs were present, the inherent high electrical resistance of the FeO_x nanowires inhibited electron movement within the FeO_x nanowires and to the current collector, demonstrated by a low current flow and al-

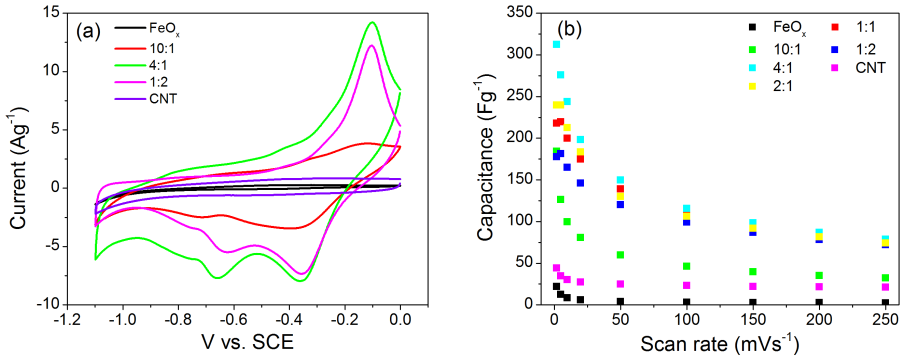

Figure 4.4: (a) CV curves of various sprayed FeO_x/MWNT electrodes at a scan rate of 20 mV s^{-1} and (b) FeO_x/MWNT electrode capacitance as a function of scan rate in 0.5 M Na_2SO_3

most no charge storage behaviour. In contrast, MWNT only electrodes provided a maximum electric double layer capacitance of 48 F g^{-1} at a scan rate of 2 mV s^{-1}. Na_2SO_3 is generally considered a comparatively poor electrolyte for carbon electrode materials, and usually H_2SO_4 is used to provide 2-4 times greater electric double layer capacitances.[38–40]

The cyclic voltammograms of all the electrodes at 20mV s^{-1} containing both FeO_x and MWNTs showed current densities much greater than either material individually. This increased current flow was attributed to the electrically conductive CNTs providing electron pathways from the FeO_x surface to the current collector, enabling electrons generated during surface reactions between FeO_x and Na_2SO_3 solution to progress throughout the porous electrode structure. The morphology of the CNTs meant that, unlike other more common conductivity additives such as carbon black or acetylene black, there was minimal pore blockage throughout the FeO_x network that allowed electrolyte ions to access all of the FeO_x surface area. In all the composite electrodes, the CV curves showed peaks in the current flow at particular voltages, and these are discussed in more detail later.

The combination of favourable morphology and spray processing meant that no additional conductivity additives (e.g. carbon black) or binder were needed, which would have increased the total electrode material mass. It is often the case in the literature that in addition to the cited 'conductivity additive' e.g. graphene[41, 42] or CNTs,[43] electrodes *also* contain carbon/acetylene black and polymer binders which are not included during the gravimetric calculation of capacitance, giving an over-estimate of specific capacitance. No such considerations were needed here.

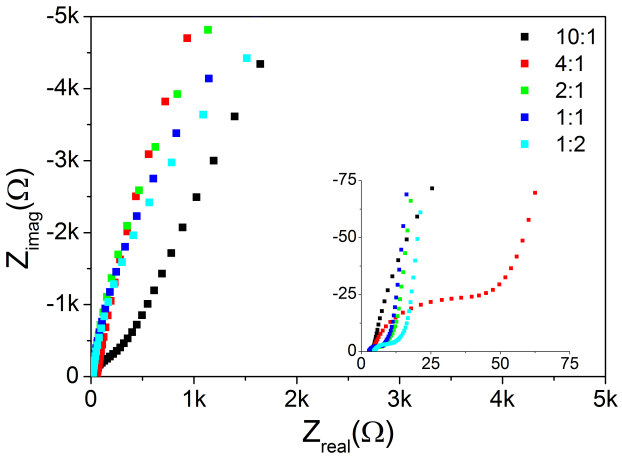

Figure 4.5: Nyquist plots of the various sprayed FeO_x/MWNT electrodes with inset of the high frequency region.

As the primary function of the comparatively expensive MWNTs was as a conductivity enhancer, it was important to minimise their mass in the electrode whilst concurrently maximising their effect on enhanced electrode conductivity. To investigate the effect of the fraction of MWNT additions, capacitances from electrodes with FeO_x:MWNT ratios between 10:1 and 1:2 were investigated. Figure 4.4(b) shows that the highest specific capacitance was 312 F g^{-1} at a scan rate of 2 mV s^{-1} with a mass fraction of FeO_x to MWNT of 4:1, which reduced to 100 F g^{-1} at a higher scan rate of 250 mV s^{-1}.

To confirm that the addition of MWNTs improved electron transfer throughout the

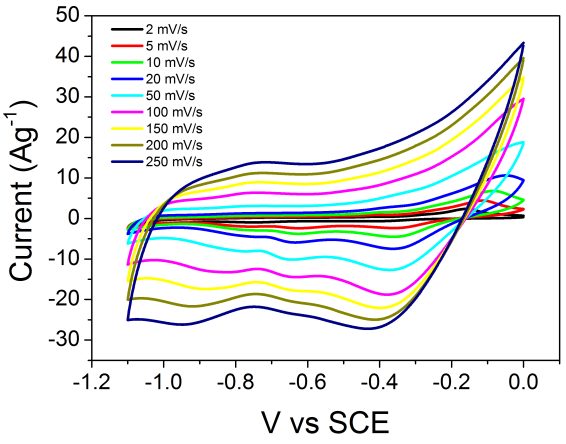

Figure 4.6: CV curves for the FeO_x/MWNT (4:1) sprayed electrodes in 0.5 M Na_2SO_3 at scan rates up to 250 mV/s.

electrode, electrochemical impedance spectroscopy (EIS) was performed in the frequency range 100 kHz to 0.01 Hz. The diameter of the high frequency semi-circle in a complex plane EIS (Nyquist) plot can be used to estimate the resistance to charge transfer at the electrode interface. Figure 4.5 shows Nyquist plots for electrodes with various MWNT mass loadings taken at open circuit potential. There was a marked decrease in the charge transfer resistance from 250 Ω for 10:1 FeO_x:MWNT to less than 10 Ω for 2:1, after which the resistance did not significantly decrease with increasing MWNT fraction. Although the higher mass fractions of MWNT afforded the lowest overall resistance, this did not correspond with the highest capacitance because the comparatively low double layer capacitance of the MWNTs began to dominate over the higher pseudocapacitance of the FeO_x beyond a 4:1 ratio. Hereafter, all results for FeO_x/MWNT electrodes refer to the optimum 4:1 ratio unless otherwise stated.

The mechanism of charge storage in Na_2SO_3 was considered by analysis of the cyclic voltammogram shape. Figure 4.6 shows the electrochemical behaviour of the 4:1 electrode in 0.5 M Na_2SO_3 at scan rates up to 250 mV s^{-1} in more detail. The CV

shape deviated from a rectangular electric double layer capacitor behaviour at all scan rates up to 250 mV s^{-1} indicating a strong pseudocapacitive contribution to charge storage, with a major peak on the anodic sweep CV at -0.2 V vs. SCE and several peaks on the cathodic sweep, notably at -0.35, -0.65 and -0.72 V vs. SCE. At low scan rates, the pseudocapacitive peaks were much more obvious due to the relatively slow kinetics of pseudocapacitance compared with EDLC; however shallow anodic peaks were still apparent at 250 mV s^{-1} and, due to the peak potential increase as scan rate increased, the dominant cathodic peak likely occurred at a potential >0 V vs SCE. The retention of these redox peaks at high scan rates suggests fast kinetics for the pseudocapacitive reactions occurring in Na_2SO_3 compared with other, faradaic reaction.

4.3.3 Electrochemical behaviour in other neutral electrolytes

To understand further the charge storage behaviour and to investigate charge storage effects of FeO_x in other neutral electrolytes, FeO_x/MWNT electrodes were investigated in the same potential window using several other benign, aqueous electrolytes containing various cations and anions. This allowed the relative contribution of different charge storage reactions in FeO_x in each electrolyte to be elucidated. Although attractive and comparable specific capacitances have been reported for iron oxide electrodes in a concentrated KOH electrolyte[23, 44] , the more benign electrolytes explored in this work are less corrosive and easier to handle, and so are more suitable for scale-up.

Figure 4.7 (a) shows the cyclic voltammograms for FeO_x/MWNT in Na_2SO_3, Na_2SO_4, Li_2SO_4 and KCl. The behaviour of the electrode in $SO_3{}^{2-}$ was markedly different

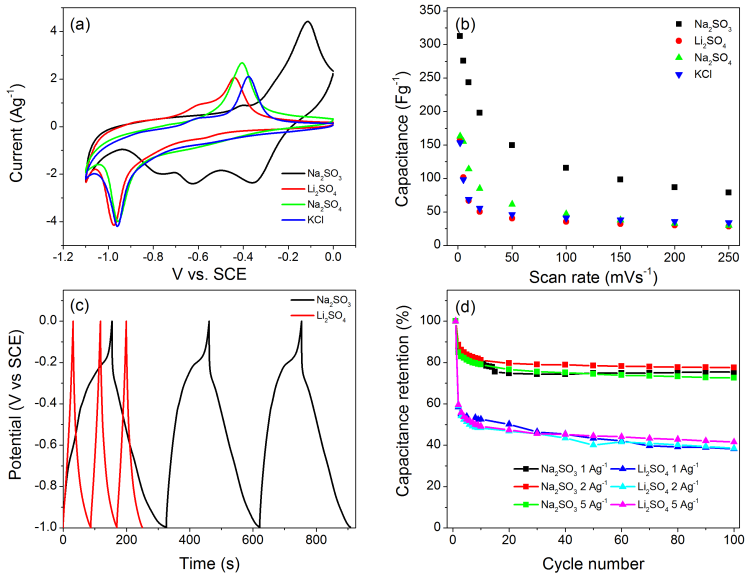

Figure 4.7: (a) Cyclic voltammograms in various aqueous electrolytes at a scan rate of 20 mV s^{-1} (b) specific capacitance from CV curves in various aqueous electrolytes (c) the 10^{th} - $13th$ charge/discharge cycle in Na_2SO_3 and Li_2SO_4 at a charging current density of 0.5 Ag^{-1}, (d) capacitance retention in Na_2SO_3 and Li_2SO_4 from discharge testing at various charging current densities

from the other electrolytes. When there was no sulphite ion, there was only one redox peak pair in the voltammograms, regardless of the cation (Na^+, Li^+, K^+) and anion (SO_4, Cl^-). This common redox pair must therefore arise from a reaction in the FeO_x, most likely due to the reduction/oxidation of Fe ions coupled with surface intercalation of electrolyte cations, a commonly suggested charge storage mechanism for FeOOH supercapacitors.[23–25] The specific capacitances calculated from the CV curves are shown in Figure 4.7 (b) and for all electrolytes other than Na_2SO_3, the capacitance was ∼150 F g^{-1} at 2 mV s^{-1}, approximately half that in Na_2SO_3, because the only pseudocapacitance was due to the FeO_x redox reaction. At higher scan rates capacitance reduced to ∼50 F g^{-1} as kinetic limitations of the reactions dominated.

Returning to the higher energy storage behaviour in the presence of SO_3^{2-}, in the relatively limited previous work, the pseudocapacitive behaviour of Fe_3O_4 was attributed to redox reactions of adsorbed $SO_3{}^{2-}$ ions due to the following reactions:[22]

$$2SO_3^{2-} + 3H_2O + 4e^- \leftrightarrow S_2O_3^{2-} + 6OH^- \tag{4.2}$$

and

$$S_2O_3^{2-} + 3H_2O + 8e^- \leftrightarrow 2S^{2-} + 6OH^- \tag{4.3}$$

These reactions are notable because they imply little or no structural change in the FeO_x, which then might be expected to maintain storage behaviour to comparatively high cycles for a metal oxide, before the well-known pulverizing effects of surface redox reactions significantly undermine the performance - a usually key weakness of transition metal oxide pseudocapacitors. The adsorption of $SO_3{}^{2-}$ onto the surface of iron oxide in H_2O with no applied potential is a well known reaction[45, 46] and likely occurred instantaneously when the electrodes were immersed in Na_2SO_3.

The cycle life of the FeO_x/MWNT electrodes in Na_2SO_3 and Li_2SO_4 was investigated using galvanostatic charge/discharge testing at current densities of 1, 2 and 5 A g^{-1}. The charge/discharge behaviour in both electrolytes, shown in Figure 4.7 (c), was asymmetric and typical of a pseudocapacitive response although there was a clear difference in both charge/discharge time and potential response in the two electrolytes. In Li_2SO_4, there was a slight flattening of the charging curve at approximately -0.5 V and of the discharge curve at -0.9 V, corresponding to the potentials at which redox reactions occurred in Figure 4.7 (a). The discharge curve for Na_2SO_3 showed a more gradual discharge with smaller deviations due to the sulphite redox reactions whereas the charging curve showed a highly flattened plateaux at -0.2 V,

the potential of the large anodic peak in the CV.

Figure 4.7 (d) shows that the capacitance retention was higher in Na_2SO_3 than in Li_2SO_4 at all current densities. After 150 cycles in Na_2SO_3, the capacitance retention was approximately 80%, however in Li_2SO_4 capacitance faded to approximately 60 % after the first cycle and then to <55 % after 150 cycles - a retention of less than 80% is considered device failure in a commercial context. The greater resilience of the storage behaviour in SO_3^{2-} can be attributed to charge storage reactions taking place primarily in the layer of adsorbed sulphite ions at the FeO_x surface, avoiding large crystal strains and subsequent electrode surface pulverization and dissolution that occurred in the other aqueous electrolytes.

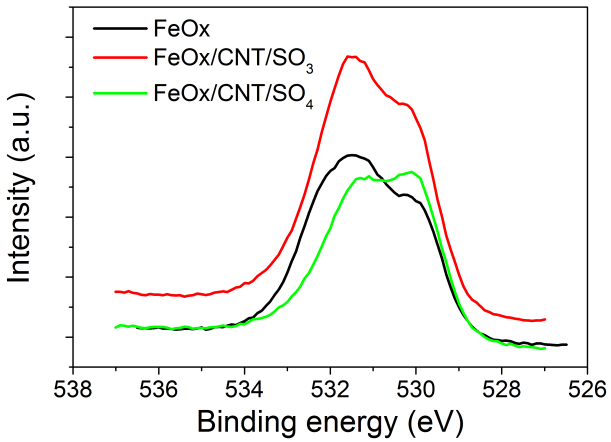

Figure 4.8: O 1s region of XPS spectra of a sprayed electrode before cycling (black) and after cycling in Na_2SO_3 (red) and Li_2SO_4 (green)

XPS spectra in the O 1s region of the as sprayed iron oxide electrode, and FeO_x/CNT electrodes after charging in Na_2SO_3 and Li_2SO_4 are shown in Figure 4.8. The electrodes were pre-conditioned for 20 CV cycles between 0 and -1.1 V then discharged to -1 V and held at this potential for 30 minutes before being removed from the electrolyte, washed with DI H_2O and dried overnight at 60°C. The high binding energy peak of the doublet at 532 eV arises from the O-H ions in the surface FeOOH.

After charging to -1 V in Li_2SO_4 the intensity of this peak reduced when compared with the lower binding energy peak at 530 eV, suggesting that there were now less OH groups at the surface and that FeOOH was reduced to FeO or Fe_2O_3 in Li_2SO_4. In contrast, identical charging experiments to -1 V in Na_2SO_3 did not lead to any significant change in O-H/O relative intensity, and again suggested that redox reactions in Na_2SO_3 uniquely took place predominantly in the surface adsorbed layer of sulphite ions, not in the FeO_x.

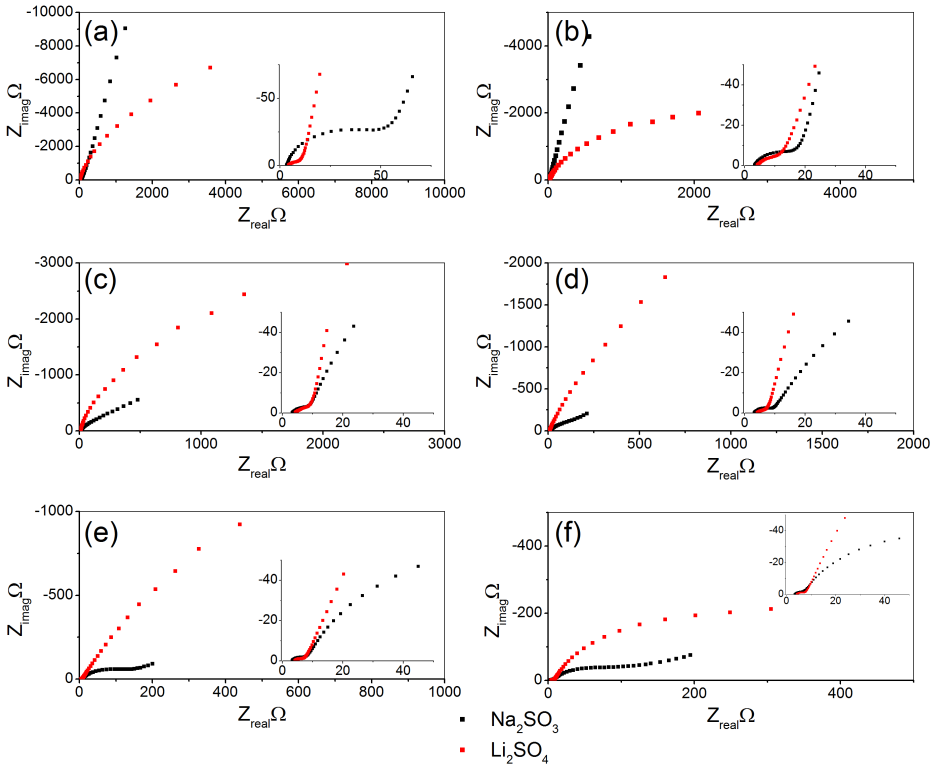

Figure 4.9: Nyquist plots in Na_2SO_3 (black) and Li_2SO_4 (red) at (a) 0 V (b) -0.1 V (c) -0.3 V (d) -0.6 V (e) -0.8 V (f) -1 V vs. SCE

EIS testing at different DC voltages can be used to probe the progression of a potential dependent charge transfer process and Figure 4.9 shows Nyquist plots of the FeO_x/MWNT electrode in Na_2SO_3 and Li_2SO_4 at various potentials from 0 to -1 V vs SCE. The EIS data was fitted using the equivalent circuit shown in Figure 4.10

where R_s is the electrolyte and circuit element resistance, Y_f/α_{ct} is a constant phase element (CPE) representing charge transfer capacitance, R_{ct} is charge transfer resistance, Y_f/α_f is the pseudocapacitive CPE, R_f is the pseudocapacitive resistance and W is a Warburg element that accounts for diffusion to and from the electrode, and through the electrode pores. In Na_2SO_3 the pseudocapacitive elements represented surface SO_3^{2-} reactions and in Li_2SO_4 the pseudocapacitive elements represented a redox reaction on the FeO_x surface. The best-fit estimates of resistance are shown in Tables 4.1 and 4.2. Considering the high frequency semi-circle in the Nyquist plots relating to charge transfer at the interface, in Na_2SO_3 the semi-circle decreased in diameter from -0.1 V to -0.6 V vs. SCE, and then remained approximately constant with further increases in potential, which is shown by the decrease in charge transfer resistances in Table 4.1 from 95 Ω to 7.5 Ω. In Li_2SO_4 the interface charge transfer resistance exhibited a lower variation from 12 - 5 Ω across all potentials. These behaviours again suggested the reactions in Na_2SO_3 took place at the electrode/electrolyte interface as the interface resistance varied with potential whereas in Li_2SO_4, charge storage occurred due to reactions within the surface layers of the FeO_x-based crystal structure.

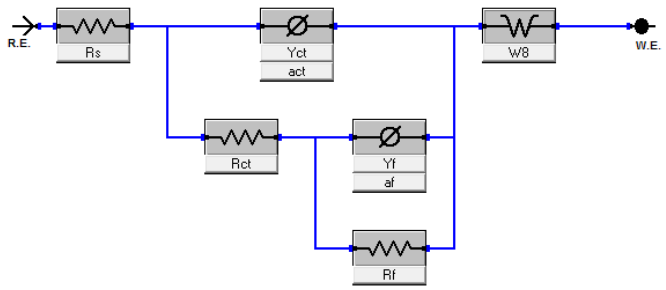

Figure 4.10: Equivalent circuit model used

Between -0.1 and -0.3 V in Na_2SO_3, the low frequency (capacitive) region was a straight line in the Nyquist plot, close to the vertical axis (90°) and was typical of

V vs SCE	R_s (Ω)	R_{ct} (Ω)	R_f (Ω)
0	3.361	94.58	$6.8e^4$
-0.1	3.36	66.24	$3.3e^{10}$
-0.3	3.28	19.7	$2.5e^{10}$
-0.6	3.21	7.446	456
-0.8	3.18	6.759	298
-1	3.14	6.544	115

Table 4.1: EIS fitting resistance values for FeO_x/MWNT electrodes in Na_2SO_3

V vs SCE	R_s (Ω)	R_{ct} (Ω)	R_f (Ω)
0	4.106	12.16	$7.1e^4$
-0.1	4.006	12.85	$1.5e^4$
-0.3	4.115	10.45	4792
-0.6	4.084	8.667	6268
-0.8	4.017	5.963	9453
-1	4.012	4.811	576
-1.1	4.069	4.802	3267

Table 4.2: EIS fitting resistance values for FeO_x/MWNT electrodes in Li_2SO_4

a non-perfect capacitor, shown in Figures 4.9a - c. Deviation from a vertical line in this region can be attributed to electrode porosity and surface roughness[47] , and the corresponding high pseudocapacitive resistances (R_f) of over 1000 Ω in Table 4.1 suggested that pseudocapacitive reactions were not occurring at these potentials. Once the DC potential reached -0.5 V (Figures 4.9d - f), R_f decreased to <500 Ω and there was emergence of a second, pseudo-capacitive semi-circle in the medium frequency region, indicating another charge transfer process, along with the beginnings of a Warburg region at frequencies below 50 mHz, again relating to the porous nature of the electrode. In Li_2SO_4, there was the beginning of a single, depressed semi-circle in the medium and low frequency regions at all potentials. The pseudocapacitive resistance R_f had a local minimum at -0.3 and -1 V which were the potentials that roughly corresponded to the regions where redox reactions occurred, as shown in Figure 4.7 (a). The emergence of low frequency semi-circles in the Nyquist plot for Li_2SO_4 at -0.3 and -1 V is shown more clearly in Figure 4.11. It should be noted that the low

frequency charge transfer process in Na_2SO_3 had a much lower resistance (smaller semi-circle diameter) at all frequencies than in Li_2SO_4, which again is consistent with charge storage reactions occurring primarily in solution at the FeO_x surface, rather than within the crystal structure. The considerable differences between the EIS behaviour in Na_2SO_3 and Li_2SO_4 were in agreement with the electrochemical results from cyclic voltammetry and galvanostatic charge/discharge.

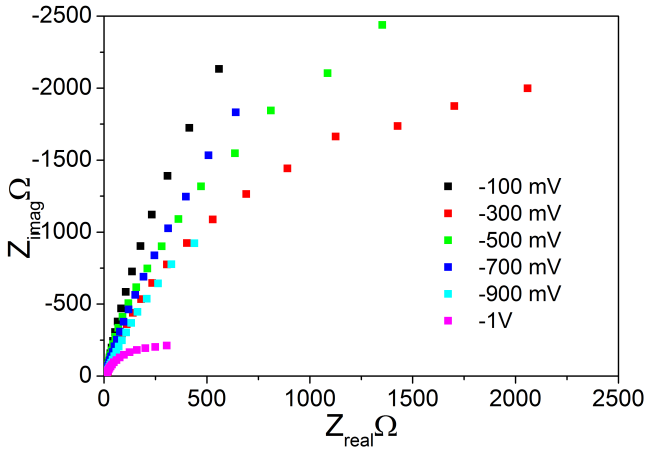

Figure 4.11: Nyquist plots in Li_2SO_4 at varying DC potential showing a more developed low frequency semi-circle at -0.3 V (red) and -1 V (purple)

4.3.4 Post-mortem SEM analysis

To investigate any structural changes to the electrode during cycling, electrodes were subject to 100 charge/discharge cycles at 1 A g^{-1} then removed from the electrolyte, washed thoroughly with DI H_2O and dried at 60 °C overnight and then investigated in the SEM. Figure 4.12 shows images of electrodes after cycling in Na_2SO_3 and Li_2SO_4. Electrodes cycled in Na_2SO_3 (Figure 4.12) showed minimal disturbance to the structure compared with the pristine as-processed electrodes shown earlier in Figures 5.2 (c)/(d). In contrast, after cycling in Li_2SO_4 (Figure 4.12 (b)) there were significant

changes in the nano-morphology of the FeO_x material, which was pulverised from long nanowires into disordered nano-particulates because of the pseudocapacitive reactions involving FeO_x surface regions and quickly mitigated any favourable effects brought about by the original macro/mesoporous electrode structure as shown in the earlier fading of capacitance in Figure 4.7 (d).

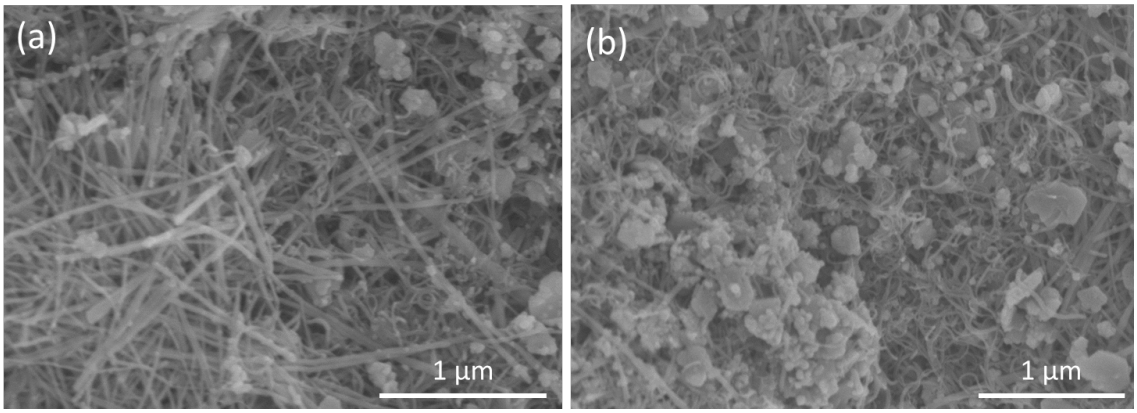

Figure 4.12: SEM images of FeO_x/MWNT electrodes after charge discharge cycling in 0.5 M: (a) Na_2SO_3 and (b) Li_2SO_4

4.4 Conclusions

Iron oxide/multiwalled carbon nanotube (MWNT) composite electrodes have been fabricated using low cost, facile synthesis and processing methods. The highly scalable spray processing technique allowed control over the mass fraction of MWNTs in the electrode over the full range and produced a well-dispersed, meso-porous network of inter-twined FeO_x nanowires and MWNTs without the need for a binder. Optimum mass fraction additions of MWNTs to FeO_x allowed relatively efficient electron transport to and from the surface of FeO_x to the current collector and suggested attractive charge storage behaviour of FeO_x in aqueous electrolytes. The capacity of the electrodes was highly dependent on the presence or lack of $SO_3{}^{2-}$ ions in the

electrolyte. When SO_3^{2-} was absent, redox reactions occurring at and in the vicinity of the FeO_x surface (which comprised predominantly FeOOH) gave a maximum capacitance of 176 F g^{-1} at 2 mV s^{-1} with rapid fading at higher scan rates to 45 F g^{-1} at 50 mV s^{-1}. When SO_3^{2-} was present, the adsorption and subsequent reactions of SO_3^{2-} rather than FeO_x afforded a much higher specific capacitance of 312 F g^{-1} at 2 mV s^{-1}, which was amongst the highest reported for FeO_x-based electrodes. The adsorbed ions were able to react rapidly in the adsorbed layer and minimised strain accumulation in the FeO_x crystal surface so that performance was retained at even high scan rates and comparatively long cycling. If MWNTs could be replaced by a cheaper conductivity enhancer that inter-twined with the FeO_x in a similar manner, then FeO_x based sprayed electrodes may provide a low cost, environmentally benign option with the potential for easy and competitive scale-up, for example, in grid-scale storage applications.

Bibliography

[1] Zhao, X., Sanchez, B. M., Dobson, P. J., and Grant, P. S. *Nanoscale* **3**(3) (2011).

[2] Hu, C. C., Chang, K. H., Lin, M. C., and Wu, Y. T. *Nano Lett.* **6**(12), 2690 (2006).

[3] Park, J. H., Ko, J. M., and Park, O. O. *J. Electrochem. Soc.* **150**(7), A864 (2003).

[4] Susanti, D., Tsai, D.-S., Huang, Y.-S., Korotcov, A., and Chung, W.-H. *J. Phys. Chem. C* **111**(26), 9530 (2007).

[5] Toupin, M., Brousse, T., and Belanger, D. *J. Mat. Chem.* **16**, 3184–3190 (2004).

[6] Kim, H. and Popov, B. *J. Electrochem. Soc.* **150**(3), D56–D62 (2003).

[7] Zhang, B. and Zhang, N. *Acta Phys. Chim. Sin.* **19**(3), 286–288 (2003).

[8] Zhang, Z., Yang, B., Deng, M., Hu, Y., and Wang, B. *Acta Chim. Sin.* **62**(17), 1617–1620 (2004).

[9] Shinde, V. R., Mahadik, S. B., Gujar, T. P., and Lokhande, C. D. *Applied Surface Science* **252**(20), 7487–7492 (2006).

[10] Xie, L., Li, K., Sun, G., Hu, Z., Lv, C., Wang, J., and Zhang, C. *J. Solid State Electrochem.* **17**(1), 55 (2013).

[11] Xu, J., Gao, L., Cao, J., Wang, W., and Chen, Z. *Electrochim. Acta* **56**(2), 732 (2010).

[12] Wang, D. W., Li, F., and Cheng, H. M. *J. Power Sources* **185**(2), 1563–1568 (2008).

[13] Wang, Y., Zhou, D., Zhao, D., Hou, M., Wang, C., and Xia, Y. *J. Electrochem. Soc.* **160**, A98 (2013).

[14] Xu, Y., Huang, X., Lin, Z., Zhong, X., Huang, Y., and Duan, X. *Nano Res.* **6**(1), 65 (2013).

[15] Tang, Z., Tang, C.-H., and Gong, H. *Adv. Funct. Mater.* **22**(6), 1272 (2012).

[16] Lee, H., Kang, J., Cho, M. S., Choi, J.-B., and Lee, Y. *J. Mat. Chem.* **21**(45), 18215 (2011).

[17] Dam, D. T., Wang, X., and Lee, J.-M. *RSC Advances* **2**(28), 10512 (2012).

[18] Li, R., Ren, X., Zhang, F., Du, C., and Liu, J. *Chem. Comm.* **48**(41), 5010 (2012).

[19] Mu, J., Chen, B., Guo, Z., Zhang, M., Zhang, Z., Zhang, P., Shao, C., and Liu, Y. *Nanoscale* **3**(12), 5034 (2011).

[20] Zhao, X., Johnston, C., Crossley, A., and Grant, P. S. *J. Mat. Chem.* **20**(36), 7637 (2010).

[21] Chen, J., Huang, K., and Liu, S. *Electrochim. Acta* **55**(1), 1 (2009).

[22] Wang, S. Y., Ho, K. C., Kuo, S. L., and Wu, N. L. *J. Electrochem. Soc.* **153**(1), A75–A80 (2006).

[23] Qu, Q., Yang, S., and Feng, X. *Adv. Mat.* **23**(46), 5574 (2011).

[24] Jin, W.-H., Cao, G.-T., and Sun, J.-Y. *J. Power Sources* **175**(1), 686 (2008).

[25] Cheng, L., Li, H., and Xia, Y. *J. Sol. St. Electrochem.* **10**(6), 405 (2006).

[26] Wang, D., Li, Y., Wang, Q., and Wang, T. *J. Solid State Electrochem.* **16**(6), 2095 (2012).

[27] Wang, D., Wang, Q., and Wang, T. *Nanotechnology* **22**(13) (2011).

[28] Nasibi, M., Golozar, M. A., and Rashed, G. *Mater. Lett.* **85**, 40 (2012).

[29] Wu, M.-S., Lee, R.-H., Jow, J.-J., Yang, W.-D., Hsieh, C.-Y., and Weng, B.-J. *Electrochem. Sol. St. Lett.* **12**(1), A1 (2009).

[30] Wu, M.-S. and Lee, R.-H. *J. Electrochem. Soc.* **156**(9), A737–. (2009).

[31] He, K., Xu, C., Zhen, L., and Shao, W. *Mater. Lett.* **61**, 3159 (2007).

[32] Zhao, X., Johnston, C., and Grant, P. S. *J. Mat. Chem.* **19**(46), 8755 (2009).

[33] Huang, C., Grobert, N., Watt, A. A. R., Johnston, C., Watt, A. A. R., Johnston, C., Crossley, A., Young, N. P., and Grant, P. S. *Carbon* **61**, 525–536 (2013).

[34] Huang, C. and Grant, P. S. *Sci. Reports* **3** (2013).

[35] Mendoza-Sanchez, B., Rasche, B., Nicolosi, V., and Grant, P. S. *Carbon* **52**, 337–346 (2013).

[36] http://srdata.nist.gov/xps/Default.aspx. .

[37] Tan, B., Klabunde, K. J., and Sherwood, P. M. A. *Chem. Mat.* **2**(2), 186 (1990).

[38] Pico, F., Rojo, J., Sanjuan, M., Anson, A., Benito, A., Callejas, M., Maser, W., and Martinez, M. *J. Electrochem. Soc.* **151**(6), A831 (2004).

[39] Wang, J., Xu, Y., Chen, X., and Sun, X. *Compos. Sci. Technol.* **67**(14), 2981 (2007).

[40] Kim, J., Nam, K., Ma, S., and Kim, K. *Carbon* **44**(10), 1963 (2006).

[41] Xu, H., Hu, Z., and Wu, H. *Mater. Chem. and Phys.* **141**(1), 310 – 317 (2013).

[42] Wang, Z., Ma, C., Wang, H., Liu, Z., and Hao, Z. *J. Alloy. Comp.* **552**, 486–491 (2013).

[43] Guan, D., Gao, Z., Yang, W., Wang, J., Yuan, Y., Wang, B., Zhang, M., and Liu, L. *Mat. Sci. Eng. B* **178**(10), 736–743 (2013).

[44] Sethuraman, B., Purushothaman, K., and Muralidharan, G. *RSC Adv.* **4**(9), 4631–4637 (2014).

[45] Baltrusaitis, J., Cwiertny, D. M., and Grassian, V. H. *Phys. Chem. Chem. Phys.* **9**(41), 5542 (2007).

[46] Ansari, A., Peral, J., Domenech, X., Rodriguezclemente, R., Roig, A., and Molins, E. *J. Photochem. Photobiol., A* **87**(2), 121 (1995).

[47] Brug, G. J., Vandeneeden, A. L. G., Sluytersrehbach, M., and Sluyters, J. *J. Electroanal. Chem.* **176**(1-2), 275–295 (1984).

Chapter 5

Electrochemical properties of FeO_x/MWNT composite electrodes as a lithium-ion battery anode

5.1 Introduction

Lithium ion (Li-ion) batteries (LiBs) are now the most common energy storage device for portable electronics such as smartphones and mobile tablets, with a current global market of over $11 bn, which is predicted to rise to over $60 bn by 2020 as LiBs penetrate into hybrid electric vehicle applications.[1, 2] LiBs are comparatively lightweight, have good cycling behaviour (∼3000 cycles), have low self-discharge, and do not suffer the progressive reduction in charge storage ('memory effect') compared

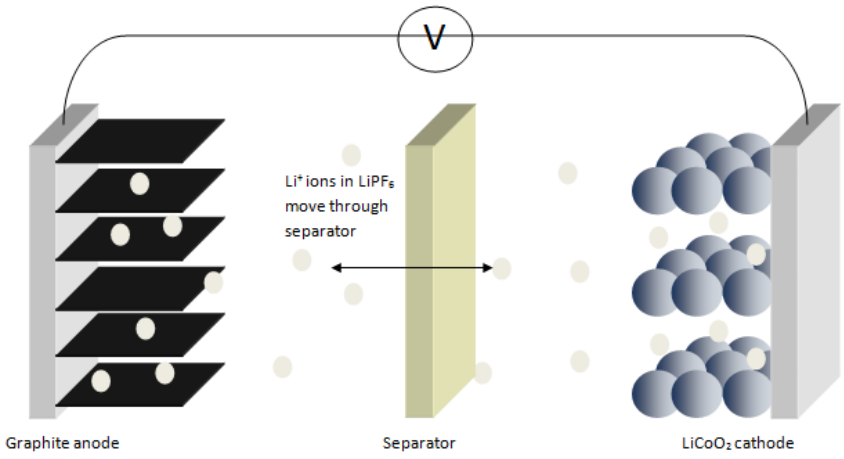

Figure 5.1: Schematic illustration of a operational lithium ion battery

with other secondary batteries e.g. nickel cadmium. The most common materials arrangement used in commercial LiB electrodes is a graphite anode with a lithium cobalt oxide/lithium iron phosphate cathode. A schematic illustration of this arrangement during operation is shown in Figure 5.1.

The energy storage reactions for a graphite/lithium cobalt oxide LiB are:

$$6C + Li^+ + e^- \rightleftharpoons LiC_6 \tag{5.1}$$

at the anode, a reaction which has a theoretical capacity of 372 mAhg^{-1} and:

$$LiCoO_2 - xLi^+ - e^- \rightleftharpoons Li_{1-x}CoO_2 \tag{5.2}$$

at the cathode, which has a theoretical capacity of 143 mAhg^{-1} for $x = 0.5$.

There is a strong commercial drive to increase the capacity of LiBs for higher energy applications, whilst keeping the electrode thickness (for portable electronics) and weight low, so alternative electrode materials with higher theoretical capacity, or

better power response, such as carbon nanotubes,[3, 4] silicon,[5] titania[6, 7] and tin[8] are being explored both academically, and commercially. Since LiBs are not the primary focus of this thesis, further details are not described, but there are many excellent reviews of LiBs elsewhere.[9–16]

Iron oxide has attracted interest as a potential replacement for graphite as an anode material in LiBs as the theoretical capacity of lithium reacting with Fe_2O_3 (1270 $mAhg^{-1}$) and Fe_3O_4 (924 $mAhg^{-1}$) is much higher than that of intercalation into graphite (372 $mAhg^{-1}$ for LiC_6). As detailed in Chapters 2 and 4, iron oxide is also a relatively safe, low cost and abundant material. Reversible capacities of over 1000 $mAhg^{-1}$ have been achieved in Fe_2O_3 electrodes[17, 18] and high performing iron oxide has been successfully fabricated in combination with carbon nanotubes[19–22] and graphene[23–25] to improve electrode conductivity and rate response.

The three most common iron oxide crystal phases: magnetite (Fe_3O_4), haematite (Fe_2O_3) and goethite (FeOOH)[26] all have the potential to store energy through conversion reactions, according to the following equations:

$$Fe_2O_3 + 6Li^+ + 6e^- \rightarrow 2Fe + 3Li_2O \tag{5.3}$$

$$Fe_3O_4 + 8Li^+ + 8e^- \rightarrow 3Fe + 4Li_2O \tag{5.4}$$

$$FeOOH + 3Li^+ + 3e^- \rightarrow Fe + Li_2O + LiOH \tag{5.5}$$

Historically, the irreversibility of these conversion processes was thought to be a barrier to the use of iron oxides in battery systems however, as with supercapacitor electrode materials, it has been shown that nanostructuring the electrode materials improves this energy storage behaviour significantly.[27–29] Nanoscale iron oxide has

been shown to intercalate lithium with higher reversibility than macrostructured crystals.[30] However, the current commercial technology for large scale electrodes, slurry casting, is not well-suited for nanomaterials processing and offers limited control over electrode morphology.

The approach and resulting structure/morphology of the FeO_x/MWNT nanowire-based electrodes developed in Chapter 4 may have potential as LiB electrodes given the relatively high inter-particulate spacing to accommodate the large volume changes caused by lithium conversion reactions. In this Chapter, the FeO_x/MWNT electrodes (ratio of 4:1) described in Chapter 4 were investigated for their behaviour as a potential lithium battry electrode in a $LiPF_6$ electrolyte using cyclic voltammetry and galvanostatic charging and discharging.

5.2 Experimental procedure

Iron oxide core shell nanowires (FeO_x) and acid-treated multi wall carbon nanotubes (MWNT) were synthesised and purified respectively, as described in Chapter 4.

Anodes were prepared by spraying suspensions of FeO_x and FeO_x/MWNT (mass ratio of 4:1) in ethanol onto 50 μm copper foil heated to 90°C on a stationary hotplate. The co-suspension was sprayed from a height of 10 cm through a nozzle moving at a surface speed of 100 mm s^{-1}. After deposition, 15 mm diameter samples were punched using an MTI coin cell punch and weighed, typically yielding a deposited mass of $\sim$1 mg cm^{-2}.

Scanning electron microscopy of sprayed materials was again performed on a JEOL FESEM 840F as described in Chapter 3. To investigate the structural integrity of

the sprayed film, the electrode sheets were rolled into a tight coil and held in this shape for 24 hours, then imaged in the SEM.

Stainless steel coin cells (type RB 1234) were assembled in an argon filled glove box with a $LiPF_6$ in 1:1 ethylene carbonate:dimethylcarbonate (EC:DMC) electrolyte, 0.3 mm Whatman glass fibre separators and lithium metal as both the counter and reference electrode before sealing with a bespoke MTI hydraulic crimping machine. The assembled cells were left to settle at room temperature for at least 24 hours after assembly before electrochemical testing to allow for thorough penetration of the electrolyte throughout the sprayed electrode.

Electrochemical tests were performed on a Gamry Reference 600 potentiostat using a 2 electrode arrangement as the Li acted as both the counter and reference electrodes. Cyclic voltammetry was performed at scan rates of 0.1 - 1 mV s^{-1} over potential range of 0.005 to 3 V vs Li^+/Li and cyclic charge/discharge was performed at current densities 1 to 0.1 A g^{-1} over a potential range of 0.005 to 2.995 V vs Li^+/Li.

5.3 Materials characterisation

The structure of the FeO_x/MWNT sprayed electrodes on a copper foil substrate/current collector was examined using scanning electron microscopy, and a representative image of the electrode microstructure is shown in Figure 5.2. The nanostructure was an open, porous network with the FeO_x and MWNTs well distributed and with meso/macroporous interparticulate and appeared to be largely unchanged compared with electrodes sprayed onto a stainless steel substrate/current collectors in Chapter 4. A picture of the flexible sprayed electrode sheet is shown in Figure 5.3 (a) and

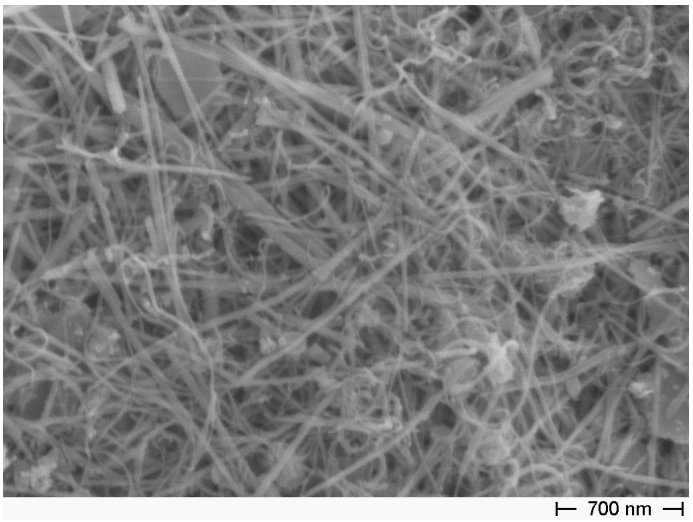

Figure 5.2: SEM image of sprayed FeO_x/MWNT composite electrodes on copper foil

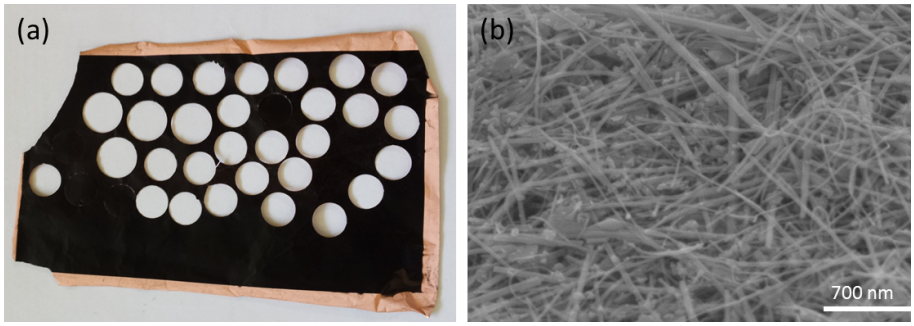

Figure 5.3: (a) A sprayed FeO_x/MWNT electrode on copper foil with samples punched for testing and (b) an SEM image of an electrode after rolling

an SEM image after the sheet was rolled and held in shape for 24 hours is shown in Figure 5.3 (b), which showed no obvious change/breakdown of the electrode microstructure, indicating encouraging mechanical flexibility and robustness required for a potential rolled battery arrangement.

5.4 Electrochemical behaviour

5.4.1 Cyclic voltammetry

Cyclic voltammetry was used to investigate reactions and structural changes occurring in the electrode as the potential was varied. Cyclic voltammetry curves of FeO_x/MWNT electrodes cycled in $LiPF_6$ at scan rates of 0.1 and 1 mV s^{-1} are shown in Figures 5.4 (a) and (b) respectively.

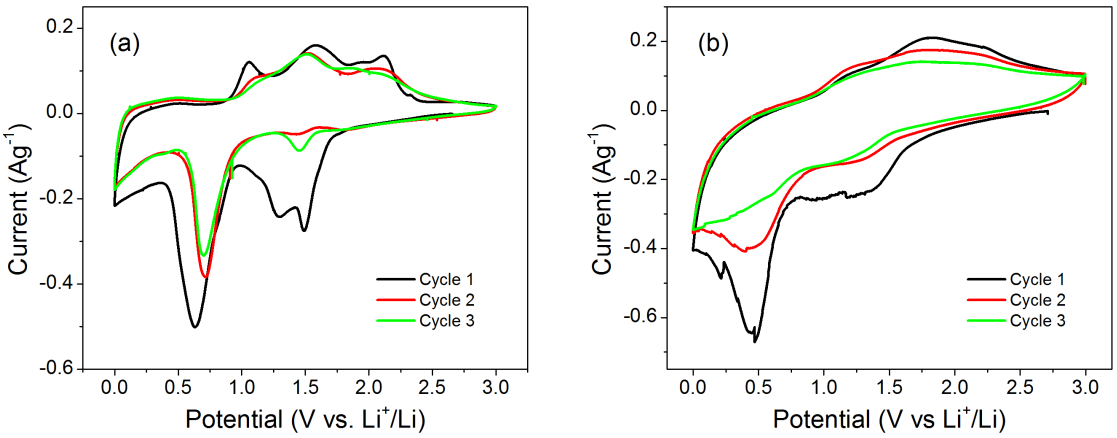

Figure 5.4: Differential capacity curves of FeO_x/MWNT electrodes taken at (a) 0.1 mVs^{-1} and (b) 1 mVs^{-1}

Figure 5.4 (a) shows much clearer redox peaks at 0.1 mV s^{-1} than those obtained at 1 mV s^{-1} in Figure 5.4 (b) as the kinetics of lithium insertion and solid electrolyte interphase (SEI) formation reactions were slow. Considering the CV curves in Figure 5.4 (a), the first anodic sweep exhibited three clear peaks and therefore three distinct electrochemical reactions, at 1.55, 1.3 and 0.6 V vs Li^+/Li. The peaks at 1.55 and 1.3 V vs Li^+/Li relate to initial Li intercalation reactions into the iron oxide before structural changes occur[18, 23] and the peak at 0.6 V vs Li^+/Li relates to both the reduction of Fe^{3+}/Fe^{2+} to Fe^0 with Li_2O formation from intercalated lithium ions

as well as the formation of a solid electrolyte interphase (SEI) due to decomposition of the electrolyte.[18, 31] The first cathodic sweep also showed three corresponding oxidation peaks at 1.05, 1.59 and 2.13 V vs Li^+/Li. The peak at 1.05 V vs Li^+/Li was related to the reversible conversion of Fe^0 to Fe^{3+} and Fe^{2+} and was much smaller than the corresponding reduction peak at 0.6 V, suggesting that most of the reactions occurring during the cathodic sweep were irreversible. The subsequent cycles contained only two redox pairs; a slightly reduced $Fe^{x+/0}$ reaction at a shifted potential of 0.7/1.1 V and a much reduced reaction at 1.45/1.5 V. The potentials shifted to slightly more positive potentials due to structural changes in the electrode and the influence of the newly-formed SEI layer. The reduced current flow during the second and third CV cycle was related to both the breakdown of the electrolyte to form the SEI layer in the first cycle, which acted as a barrier to the reversible lithium intercalation in subsequent cycles and reduces the number of available Li^+ ions, as well as the reduced number of $Fe^{2/3+}$ ions available due to some irreversible reduction in the first cycle. After the initial cycle, the voltammetry behaviour showed much higher stability.

5.4.2 Charging behaviour

The energy storage capabilities of battery electrodes are generally evaluated using galvanostatic charging and discharging. FeO_x/MWNT electrodes and FeO_x electrodes with no MWNT or conductivity enhancer were charged and discharged at a rate of 1 A g^{-1} (total electrode mass) which is approximately equal to a 1 C rate although with a mixed phase FeO_x material this was difficult to calculate accurately. The first, second, fifth, tenth and twentieth charge/discharge cycles are shown in Figure 5.5.

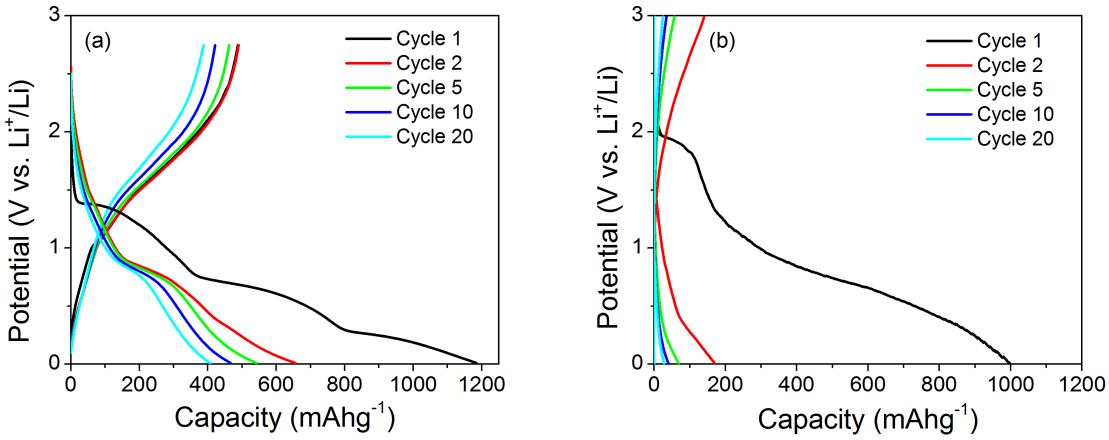

Figure 5.5: Charging and discharging curves at 1 Ag^{-1} for (a) FeO_x/MWNT electrodes and (b) FeO_x electrodes

For electrodes comprised of FeO_x nanowires only, a first discharge capacity of 998 $mAhg^{-1}$ was achieved, however this rapidly reduced to 170 $mAhg^{-1}$ on the second cycle and then to less than 40 $mAhg^{-1}$ by cycle 10. For FeO_x/MWNT electrodes a high first discharge capacity of 1180 $mAhg^{-1}$ gradually faded to 403 $mAhg^{-1}$ at cycle 20. The reduced capacity fading was due to improved conductivity through the electrode provided by the MWNTs, which has been shown to result in a thinner and more homogeneous SEI layer[29] , and possibly improved electrode resilience.

The extent of capacity fading in the FeO_x/MWNT electrodes was typical for many iron oxide-based anodes cycled at a relatively high rate of ~1000 mA g^{-1}[1,23, 32–36] and can be attributed to the formation of the SEI layer that blocked access to the active material, combined with some irreversible Li_2O formation. It was also likely that the FeO_x/MWNT network was pulverised (despite the nanostructuring) during cycling causing capacity fading. More rigid electrodes formed by hard templating of copper substrates followed by electrodeposition of a thin film of Fe_3O_4 (0.06 - 0.225 mg cm^{-2}) had a better capacity retention of 76% after 20 charge discharge cycles.[37] To improve the cycling behaviour of the sprayed FeO_x electrodes for lithium-ion

batteries, a more robust mechanical 'buffer' matrix of carbon could be investigated, as the advantageous high surface area provided by the MWNTs when the electrode were tested for surface dependent supercapacitor behaviour is of less importance for bulk Li charge storage. It should be noted that the capacity of FeO_x/MWNT electrodes after 20 cycles was still higher than the theoretical and achieved capacity of graphite-based anodes, which does not usually exceed 350 $mAhg^{-1}$.

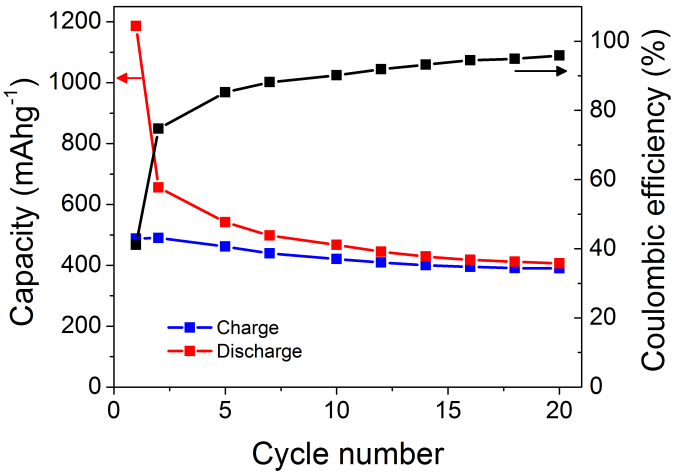

Figure 5.6: Cycling capacity and coulombic efficiency of FeO_x/MWNT electrodes over the first 10 cycles

Figure 5.6 shows the capacity calculated from charge/discharge curves for the FeO_x/MWNT electrodes and the corresponding coulombic efficiency, $\eta = \frac{t_c}{t_d}$, where t_c/t_d was the time for charge and discharge respectively. As the charging capacity stayed comparatively constant at approximately 400 $mAhg^{-1}$ from cycle 1 to 20 and the discharge capacity showed an initial sharp decrease followed by levelling above 10 cycles, the coulombic efficiency reached 96% by cycle 20.

5.5 Conclusions

FeO_x/MWNT electrodes provided a first discharge capacity of over 1180 $mAhg^{-1}$, which is close to the maximum theoretical capacity of iron oxide and much higher than the maximum theoretical capacity of graphite. The inclusion of MWNTs in the electrode helped sustain a much higher capacity after 20 cycles of 406 $mAhg^{-1}$ compared with 27 $mAhg^{-1}$ for FeO_x electrodes without MWNTs. Although first to second cycle capacity losses were large, the increased coulombic efficiency after 10 cycles and final stable capacity of over 400 $mAhg^{-1}$ was still higher than the maximum capacity of graphite and confirmed, in the right structural arrangement, that iron oxide may be a promising material for lithium ion anodes. The virtuous effect of the MWNTs on cycle behaviour was not identified conclusively, but may relate to helping to ensure that both SEI formation and the strains of intercalation and conversion were homogenised throughout the electrode assembly. Cycling response may be improved further by optimising the microstructure and conductivity additives used in the sprayed FeO_x electrodes, perhaps using both MWNTs and conventional carbon black, with the latter helping to minimise structural movement during conversion reactions.

Bibliography

[1] Scrosati, B. and Garche, J. *J. Power Sources* **195**(9), 2419 – 2430 (2010).

[2] Harrop, P. *Speciality Chemicals Magazine* Feb (2013).

[3] Chen, S., Chen, P., and Wang, Y. *Nanoscale* **3**(10), 4323–4329 (2011).

[4] Wang, W. and Kumta, P. *ACS Nano* **4**(4), 2233–2241 (2010).

[5] Fu, Y. and Manthiram, A. *Nano Energy* **2**(6), 1107–1112 (2013).

[6] Ortiz, G., Hanzu, I., Djenizian, T., Lavela, P., Tirado, J., and Knauth, P. *Chem. Mater.* **21**(1), 63–67 (2009).

[7] Su, X., Wu, Q., Zhan, X., Wu, J., Wei, S., and Guo, Z. *J. Mater. Sci.* **47**(6), 2519–2534 (2012).

[8] Xu, L., Dong, A., Kim, C., Mattox, T., Milliron, D., and Cabana, J. *ACS Nat. Meet.* (2011).

[9] Bruce, P., Scrosati, B., and Tarascon, J.-M. *Angew. Chem. Int. Ed.* **47**(16), 2930–2946 (2008).

[10] Etacheri, V., Marom, R., Elazari, R., Salitra, G., and Aurbach, D. *Energ. Environ. Sci.* **4**(9), 3243–3262 (2011).

[11] Zhang, W.-J. *J. Power Sources* **196**(1), 13–24 (2011).

[12] Marom, R., Amalraj, S., Leifer, N., Jacob, D., and Aurbach, D. *J. Mater. Chem.* **21**(27), 9938–9954 (2011).

[13] Bandhauer, T., Garimella, S., and Fuller, T. *J. Electrochem. Soc.* **158**(3), R1–R25 (2011).

[14] Malini, R., Uma, U., Sheela, T., Ganesan, M., and Renganathan, N. *Ionics* **15**(3), 301–307 (2009).

[15] Hu, M., Pang, X., and Zhou, Z. *J. Power Sources* **237**, 229–242 (2013).

[16] Song, J., Wang, Y., and Wan, C. *J. Power Sources* **77**(2), 183–197 (1999).

[17] Xu, Y., Jian, G., Liu, Y., Zhu, Y., Zachariah, M., and Wang, C. *Nano Energy* **3**, 26–35 (2014).

[18] Jiang, Y., Zhang, D., Li, Y., Yuan, T., Bahlawane, N., Liang, C., Sun, W., Lu, Y., and Yan, M. *Nano Energy* **4**, 23–30 (2014).

[19] Seo, S.-D., Lee, G.-H., and Kim, D.-W. *J. Alloy. Comp.* (2014).

[20] Bak, B., Kim, S.-K., and Park, H. *Mater. Chem. Phys.* (2014).

[21] Seo, S.-D., Lee, G.-H., and Kim, D.-W. *J. Alloy. Comp.* (2014).

[22] Bak, B., Kim, S.-K., and Park, H. *Mater. Chem. Phys.* (2014).

[23] Zhao, B., Liu, R., Cai, X., Jiao, Z., Wu, M., Ling, X., Lu, B., and Jiang, Y. *J. Appl. Electrochem.* **44**(1), 53–60 (2014).

[24] Jang, B., Chae, O., Park, S.-K., Ha, J., Oh, S., Na, H., and Piao, Y. *J. Mat. Chem. A* **1**(48), 15442–15446 (2013). cited By (since 1996)1.

[25] Wang, J.-Z., Zhong, C., Wexler, D., Idris, N., Wang, Z.-X., Chen, L.-Q., and Liu, H.-K. *Chem. Euro. J.* **17**(2), 661–667 (2011).

[26] Xiaoming Lou, X. W. and Zhang, Y. *EChem. Comm.* **11**(8), 16961699 (2009).

[27] Wu, C., Yin, P., Zhu, X., OuYang, C., and Xie, Y. *J. Phys. Chem. B* **110**(36), 17806–17812 (2006).

[28] Reddy, M., Yu, T., Sow, C.-H., Shen, Z., Lim, C., Rao, G., and Chowdari, B. *Adv. Funct. Mater.* **17**(15), 2792–2799 (2007).

[29] Zhang, W.-M., Wu, X.-L., Hu, J.-S., Guo, Y.-G., and Wan, L.-J. *Adv. Funct. Mater.* **18**(24), 3941–3946 (2008).

[30] Larcher, D., Masquelier, C., Bonnin, D., Chabre, Y., Masson, V., Leriche, J.-B., and Tarascon, J.-M. *J. Electrochem. Soc.* **150**(1), A133–A139 (2003).

[31] Chen, J., Xu, L., Li, W., and Gou, X. *Adv. Mater.* **17**(5), 582–586 (2005).

[32] Liu, H., Wexler, D., and Wang, G. *J. Alloy. Comp.* **487**(1-2), L24–L27 (2009).

[33] Wu, S., Wang, Z., He, C., Zhao, N., Shi, C., Liu, E., and Li, J. *J. Mat. Chem. A* **1**, 11011–11018 (2013).

[34] Di Lupo, F., Gerbaldi, C., Casino, S., Francia, C., Meligrana, G., Tuel, A., and Penazzi, N. *J. Alloy. Comp.* (2014).

[35] Hu, M., Jiang, Y., and Yan, M. *J. Alloy. Comp.* **582**, 563–568 (2014).

[36] Hong, Z., Tang, Z., Hong, Y., Tang, H., and Zhang, Z. *Mater. Lett.* **93**, 226–229 (2013).

[37] Wu, H., Du, N., Wang, J., Zhang, H., and Yang, D. *J. Power Sources* **246**, 198–203 (2014).

Chapter 6

Nickel oxide/exfoliated graphene composite electrodes for supercapacitor applications

6.1 Introduction

Nickel oxide (NiO) has attracted significant interest as a potential replacement for RuO_2 as a high performance supercapacitor electrode material for niche applications due to its much lower cost, practical availability and high theoretical capacitance of 2573 F g^{-1}.[1–3]

In an attempt to realise this high capacity in practice, nano-structuring of NiO has been investigated, and the specific morphology has been shown to have a significant impact on the resulting electrochemical behaviour. For example, a recent study[4] showed that NiO nanocolumns provided an enhanced capacitance of 290 F g^{-1} com-

pared with 175 F g^{-1} for NiO nanoslices, which was attributed to a higher specific surface area of 102 $m^{-2}g^{-1}$ compared with 11.4 $m^{-2}g^{-1}$, as well as nanopores providing effective diffusion channels for electrolyte ions. With this in mind, this chapter explores micro/mesoporous electrode morphologies afforded by the combination of 1D NiO nanomaterials with electrode processing by spray deposition for their potential to yield high performance supercapacitor electrodes. Despite the attractive properties, as with all transition metal oxides, NiO suffers from poor electron conductivity that undermines performance at high sweep and charge/discharge rates, and so practical implementations require the addition of conductivity enhancing additives to achieve acceptable energy and power density performance.

Graphene has attracted increasing interest as a supercapacitor electrode material, both stand-alone[5–9] and as a conductivity enhancer[10–12] has high inherent electrical conductivity (depending on form and purity) and has a theoretical surface area of over 2500 m^2g^{-1}. However, these advantages are usually marred by the tendency of individual graphene sheets to re-stack within the electrode and thus gradually block ion mobility.[13–15]

Exfoliated graphene is obtained by low cost, low temperature synthesis from bulk graphite and has shown promising capacitance retention in graphene-only electrodes up to scan rates as high as 10,000 mV s^{-1}.[16] Corresponding energy densities however, were disappointingly low and indicate that exfoliated graphene is likely to be most useful for energy storage applications in combination with materials able act as "spacers" to inhibit re-stacking, as well as additions to enhance specific energy, such as nanostructured transition metal oxides.

The exceptionally stable nature of exfoliated graphene suspensions over many months even when exposed to a variety of experimental conditions has suggested that they

are well-suited to spray processing of suspension directly into electrodes without requiring further modification. In contrast, most previous reports of high-performing nickel oxide-graphene composites for electrochemical capacitors have made use of reduced graphene oxide materials[17, 18] or employed expensive and complex processing routes such as electrophoretic deposition (EPD)[19, 20] or chemical vapour deposition (CVD).[21] Despite its proven high conductivity and power performance, at the time of writing there are no easily obtained reports that describe the route pursued here of combining ultrasonically exfoliated aqueous suspensions of graphene and transition metal oxide materials for supercapacitor applications.

In this chapter, nickel oxide was synthesised using a low temperature, hydrothermal synthesis followed by thermal annealing. The resultant NiO nanomaterial was combined with exfoliated graphene through a variety of spray processing variants in an all-aqueous, low cost process. These composite electrodes were investigated for supercapacitor behaviour in 2 M KOH using cyclic voltammetry, galvanostatic charge/discharge and electrochemical impedance spectroscopy. The particular processing variant used to combine the two nanomaterials had a notable effect on energy storage behaviour, with composite electrodes arising from co-synthesis sustaining superior performance at high sweep rates. The substrate/current collector choice was also carefully investigated, as the nickel foam substrates most commonly used in the literature were shown to be electrochemically reactive in the electrolyte and potential window of interest.

6.2 Experimental details

6.2.1 Materials

All chemicals were purchased from Sigma (UK) and used without further purification.

6.2.2 Nickel oxide synthesis

NiO nanowires were synthesised via hydrothermal synthesis followed by thermal annealing to NiO[22] as follows: 9.8 mmol NaOH was dissolved in 10 ml H_2O and 9.8 mmol $NiSO_4.7\,H_2O$ was dissolved in 30 ml H_2O. The NaOH solution was added dropwise to the $NiSO_4$ solution under magnetic stirring resulting in immediate precipitation of a pale blue solid. The mixture was transferred to a 120 ml teflon lined stainless steel autoclave and heated at 120 °C for 24 hours. After cooling, the resultant pale blue solid was collected, washed with DI H_2O until pH = 7 and dried in air overnight at 60 °C. Finally, the powder was annealed at 400 °C in air for 2 hours for complete conversion to NiO. For NiO-graphene co-synthesis materials described later, H_2O in the $NiSO_4 \cdot 7\,H_2O$ solution was replaced by 30 ml exfoliated graphene solution, synthesised as described below.

6.2.3 Exfoliated graphene synthesis

Aqueous solutions of exfoliated graphene were produced using a low power ultrasonic exfoliation technique outlined elsewhere.[23, 24] Briefly, 1.5 g graphite was added

to a 0.1% aqueous solution of sodium cholate (500 ml). Low power sonication was carried out in a 150 W ultrasonic bath for 50 hours. The resulting suspension was centrifuged at 1000 rpm for 90 minutes to remove residual graphite, and the supernatant graphene solution decanted. The graphene concentration c was determined using the Beer-Lambert law ($A = \varepsilon cl$ where A is the measured absorption, ε is the molar absortivity, c is the solution concentration and l is the path length) at 660 nm assuming a molar absortivity ε of 6600 mL g^{-1} cm^{-1}, and was determined to be $c = 0.03$ mg ml^{-1}

6.2.4 Materials characterisation

Materials were characterised by powder x-ray diffraction, scanning electron microscopy and Raman spectroscopy, details of which were given in Chapter 3 sections 3.2.1, 3.2.5 and 3.2.3 respectively.

6.2.5 Electrode processing

NiO suspensions were formed by sonicating NiO in DI H_2O at a concentration of 1 mg ml^{-1} in an ultrasonic bath for 20 minutes. No surfactant or pH adjustment was necessary to form a stable suspension. Suspensions were sprayed at a flow rate of 3 ml min^{-1} and a nozzle height of 10 cm onto substrates heated to 110 °C pre-coated with a thin layer of polyethylene imine (PEI, 0.1%, 2 coats) for improved adhesion. Typical 1 cm^2 electrodes had a deposited mass of 0.5 mg cm^{-2} and a film thickness of 2-3 μm. NiO-graphene composite electrodes were produced under identical conditions, further described in Section 6.6. For co-sprayed samples, exfoliated graphene was sprayed at 1 ml min^{-1} through a nozzle positioned next to the NiO solution nozzle with a spray

cone separation of 3 cm. The spraying area was adjusted accordingly to ensure all sections of the substrate were exposed to both suspension spray cones.

6.2.6 Electrochemical characterisation

Electrochemical testing was performed using a Gamry ref 600 potentiostat in a three electrode cell using a hydroflex reference electrode and a Pt coated titania counter electrode and 2 M KOH aqueous electrolytes. Cyclic voltammetry was performed in the potential range 0 to 0.6 V vs. hydroflex at scan rates 2 - 500 mV s^{-1}. Galvanostatic charge/discharge tests were performed at current densities of 0.5 - 100 A g^{-1}. Specific capacitance values were reproducible to +/- 10 F g^{-1}

6.3 Results and discussion

6.3.1 Nickel oxide characterisation

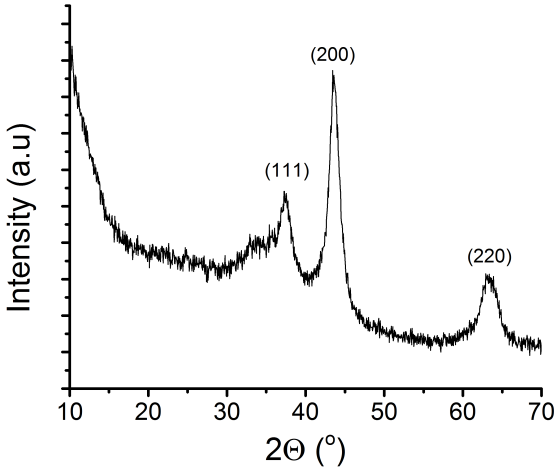

Figure 6.1: PXRD pattern of as-synthesised nickel oxide

Figure 6.1 shows the PXRD pattern of as-synthesised nickel oxide powder after annealing at 400 °C. The three clear peaks at 37.1, 43.1 and 62.5 ° (2θ) corresponded to hkl values of (111), (200) and (220) respectively and the material was indexed to NiO (JCPDS card number 22-1189) with a cubic unit cell and space group $Fm\bar{3}m$. PXRD of NiO electrodes taken after spray deposition (not shown) confirmed that the chemical phase was not altered during electrode processing.

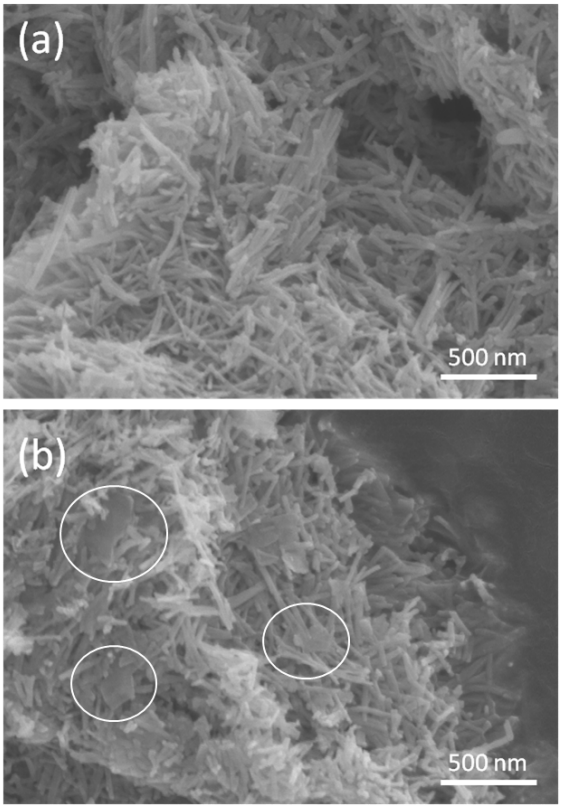

Figure 6.2: SEM images of (a) as-synthesised NiO and (b) NiO-graphene co-synthesised composite

An SEM image of typical as-synthesised NiO is shown in Figure 6.2 (a) revealing largely 1D nanostructures approximately 500 nm in length and 10 nm wide. This nanomorphology from the hydrothermal synthesis was unaltered by the subsequent relatively high temperature annealing at 400 °C. NiO synthesised in an exfoliated graphene solution rather than in DI H_2O, Figure 6.2 (b), exhibited a qualitatively

identical nanostructure indicating that the presence of graphene did not significantly affect the NiO morphology. It was possible to identify flat, plate-like carbon deposits in Figure 6.2 (b) (circled), which were most likely multi-layer (not fully exfoliated or partially re-stacked) graphene flakes.

6.4 Substrate choice

Most reports of NiO materials for supercapacitor electrodes utilise nickel or stainless steel foams as substrates/current collectors. It is important to note that these materials both contain nickel atoms that are able to partake in an electrochemical reaction in the KOH electrolyte to form nickel hydroxide,[25–27] which is able to undergo a reversible redox reaction according to:

$$\mathrm{Ni} + 2\mathrm{OH}^- \rightarrow \mathrm{Ni(OH)}_2 \rightleftharpoons \mathrm{NiOOH} + H^+ \tag{6.1}$$

Cyclic voltammetry (CV) curves of 1 cm^2 untreated 316 stainless steel (SS) and nickel foam immersed in 2 M KOH and cycled at 50 mV s^{-1} for 200 cycles are shown in Figure 6.3.

Both materials exhibited redox peak pairs in the potential window over which NiO is electrochemically active (-0.1 - 0.5 V vs SCE/0.9 - 1.5 V vs hydroflex). Stainless steel showed a broad anodic and cathodic peak at 1.5 and 1.3 V vs a hydroflex reference respectively, with a marginal increase of the peak current during cycling. Ni foam exhibited two sharp anodic and cathodic peak pairs at 1.4/1.15 and 1.5/1.3 V vs hydroflex, and a large increase in peak current during cycling. This increase can

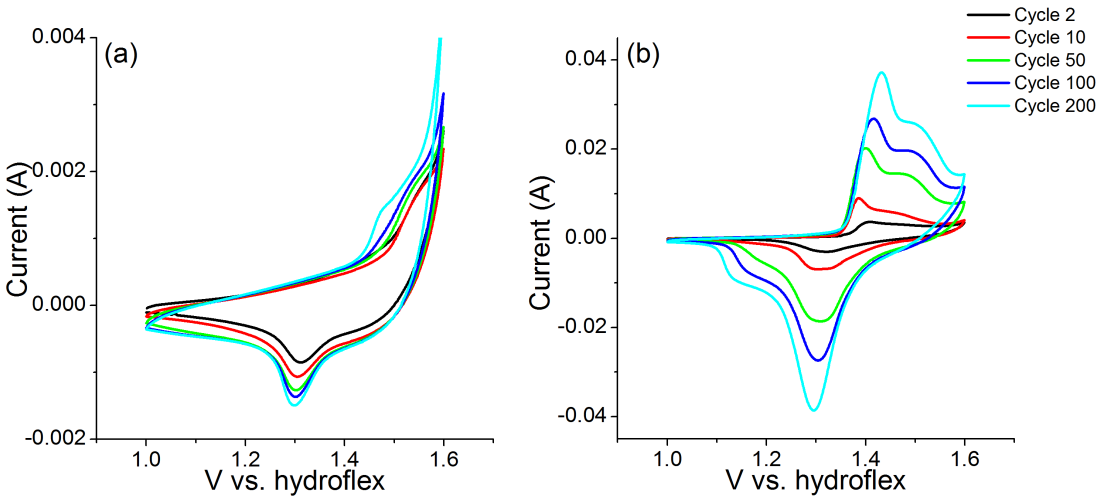

Figure 6.3: Cyclic voltammetry curves of (a) bare SS substrate and (b) bare Ni foam up to 200 cycles at 50 mV s^{-1} in 2 M KOH

be attributed to increasing amounts of oxidised Ni in the form of $Ni(OH)_2$ on the surface of the Ni foam and subsequent redox cycling.[28]

For comparable 2D areas of immersed electrode, a large disparity between absolute values of current was apparent, with the integrated area under cycle 200 for nickel foam (218 mC) ~17 x larger than that of cycle 200 for stainless steel (12.5 mC). This variation likely arose from (1) the higher absolute surface area exposed to electrolyte solution in the case of the foam (the stainless steel plate provided an accessible surface area of 1 cm^2 whereas the porous nature of nickel foam allowed for a surface area 8.7 times greater, according to the supplier's data); and (2) the reduced availability of Ni atoms to undergo reaction in the 316 stainless steel (Ni content = 10 - 14 %) compared with pure Ni foam.

As these commonly utilised substrates exhibit electrochemical activity in KOH, it is important to carefully extract the charge storage behaviour arising from the "elec-

trode material" itself from the overall measured behaviour of electrode plus substrate, since it is unlikely that all the underlying substrate surface could be entirely shielded from contact with the electrolyte solution, especially with the porous structures that are preferable for supercapacitor electrodes. It is not obvious from many literature reports that this factor is either acknowledged or accounted for in the reported capacitances.

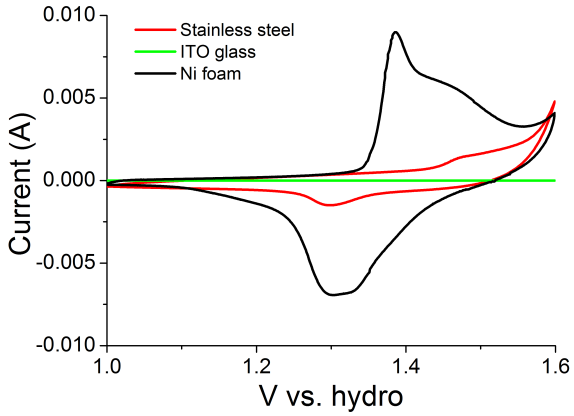

Figure 6.4: 10th cycle CV curves of bare stainless steel, bare Ni foam and bare ITO coated glass at 50 mV s^{-1} in 2 M KOH

To avoid electrochemical contributions due to the reaction of the substrate and electrolyte (or reactions between the electrode and substrates), ITO coated glass was initially used as a substrate/current collector for the sprayed NiO nanomaterials and its composites. A CV curve of ITO coated glass in KOH is also shown in Figure 6.4 (green) and, unlike Ni foam or stainless steel, there was no significant redox peaks or double layer capacitance, while providing the necessary electrical conductivity (sheet resistance of 7 ohm sq^{-1}). Results subsequently presented in Sections 6.5 and 6.6 refer to samples sprayed exclusively onto ITO coated glass.

6.5 Electrochemical activity of NiO

To first understand the baseline electrochemical behaviour of the system, electrodes comprised of NiO nanostructures on ITO glass with no conductivity additive or binder were investigated using cyclic voltammetry and galvanostatic charge/discharging.

CV curves for NiO electrodes in 2 M KOH at scan rates from 2 - 250 mV s^{-1} are shown in Figure 6.5. Curves at scan rates below 20 mV s^{-1} contained one clear redox peak pair with an anodic peak at 1.3 - 1.35 V and a cathodic peak at 1.24 - 1.21 V. As the electrode contained no conductivity additive or binder, the redox behaviour arose from the reaction of NiO as it was oxidised and reduced according to:[1–3, 29]

$$NiO + OH^- \rightleftharpoons NiOOH + e^- \tag{6.2}$$

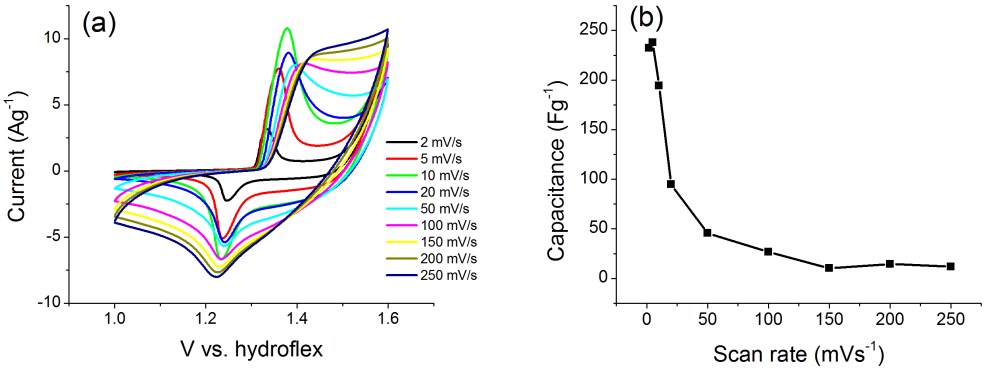

Figure 6.5: (a) Cyclic voltammetry curves of NiO only electrodes at scan rates between 2 mV s^{-1} and 250 mV s^{-1}, (b) capacitance of NiO electrodes calculated from cyclic voltammetry

Specific capacitance was calculated from the CV curves according to:

$$S_c = \frac{\int IdV}{2.m.\nu.\Delta V} \tag{6.3}$$

where $\int IdV$ corresponds to the area under CV curves, m is the mass of electrode material, ν is the scan rate in mV s^{-1} and ΔV is the operating potential window. At scan rates up to 10 mV s^{-1}, NiO electrodes sustained reasonable charge storage behaviour and reversibility, with a maximum capacitance at 5 mV s^{-1} of 237 F g^{-1}. However the electrochemical behaviour deteriorated rapidly beyond a relatively slow scan rate of 20 mV s^{-1}, above which the peak current did not surpass the peak anodic current of 10 A g^{-1} obtained at 10 mV s^{-1} and specific capacitance reduced to 50 F g^{-1} at 50 mV s^{-1} and then to less than 10 F g^{-1} at 150 mV s^{-1}.

Galvanostatic charge/discharge testing of NiO electrodes was performed at current densities of 1 - 50 A g^{-1} and at all current densities, the resulting curves showed a distinctly non-linear shape, with a plateau between 1.3 - 1.4 V vs hydroflex, as shown in Figure 6.6. Non-linear charge/discharge behaviour (no clear "saw tooth" shape of EDLC behaviour) is typical of pseudocapacitive materials involving a faradaic charge transfer process. Capacitance was calculated from the discharge curves according to:

$$C_s = \frac{I}{\frac{dV}{dt}m} \tag{6.4}$$

where I is the discharge current density, m is the electrode mass and $\frac{dV}{dt}$ was estimated considering the integrated area under the discharge curve, A, to be $\frac{dV}{dt} = \frac{\Delta V^2}{2A}$ due to the non-linearity of the slope. Capacitance estimated from the discharge

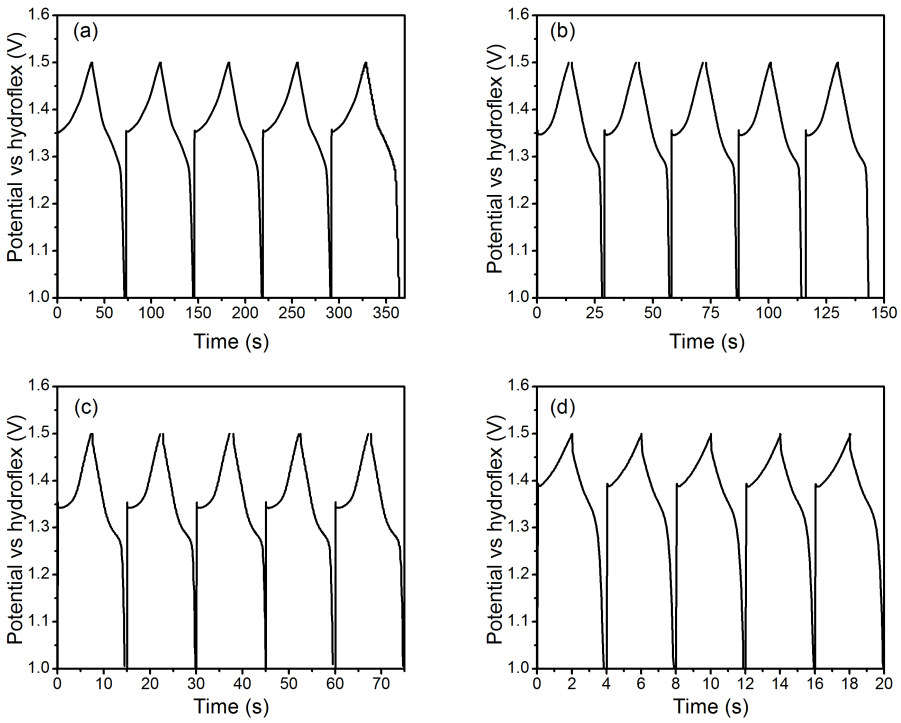

Figure 6.6: Charge discharge curves of NiO electrodes at a current density of (a) 1 A g^{-1} (b) 5 A g^{-1} (c) 10 A g^{-1} (d) 20 A g^{-1}

curves is shown as a function of current density in Figure 6.7 with capacitance a maximum of 132 F g^{-1} at a charging current of 1 A g^{-1} and dropping to below 70 F g^{-1} at a charging current of 20 A g^{-1}.

The poor charge storage behaviour at even relatively low rates can be attributed to sluggish electron transfer throughout the NiO electrode. This is an inherent feature of metal oxide electrodes and highlights the necessity of conductivity additives to improve performance. To overcome this limitation and improve energy storage behaviour, exfoliated graphene solutions were added to NiO nanostructures to improve conductivity both throughout the electrode and to then enhance charge transfer

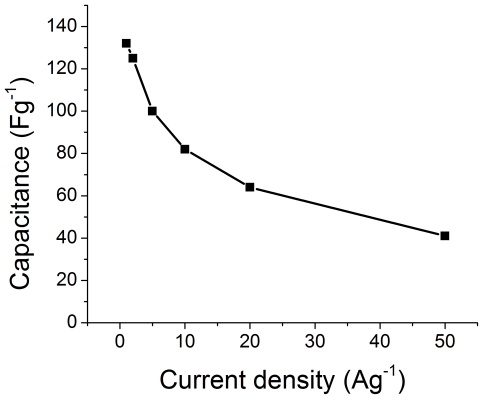

Figure 6.7: Capacitance from discharge curves for NiO electrodes in 2 M KOH

behaviour with the current collector.

6.6 Effect of graphene additions - processing

The spray deposition processing technique readily allowed for the addition of exfoliated graphene to the NiO electrodes. It was possible to add graphene at several stages of the process: during chemical synthesis of the NiO ('co-synthesis'), in the pre-spray suspension ('co-suspension') or during spraying ('co-spray'). A schematic description of the different processing routes is shown in Figure 6.8.

To investigate the effect of the processing route on the interaction between NiO and graphene, composite electrodes were prepared through each of the three routes. However, it was not possible initially to form a stable co-suspension of NiO and graphene as the opposing surface charges on the two materials resulted in immediate attraction and agglomeration, causing both materials to fall out of suspension. The addition of 1 % sodium dodecyl sulphate (SDS) as a surfactant and high power (750 W) sonication allowed a pseudo-stable suspension to form (approximately 30 minutes

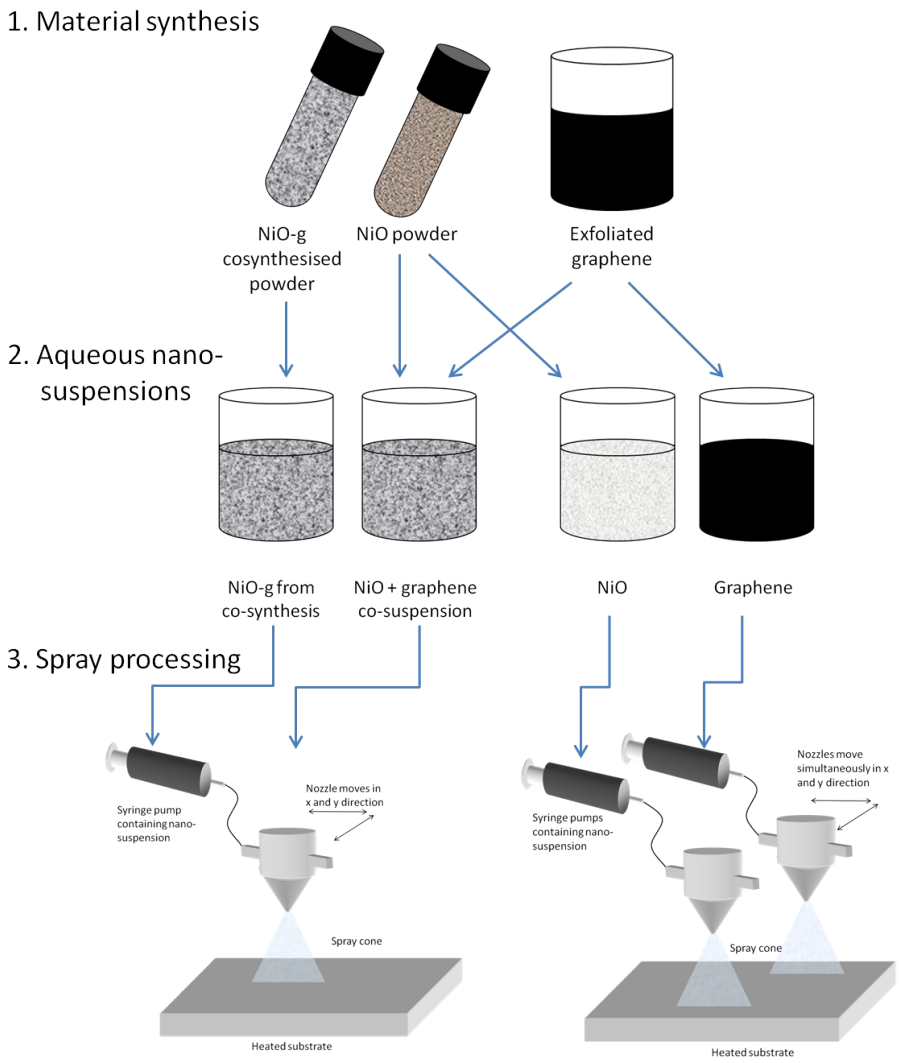

Figure 6.8: Spray deposition of NiO and graphene nano-suspensions

stability window) that was sufficient to allow for electrode formation.

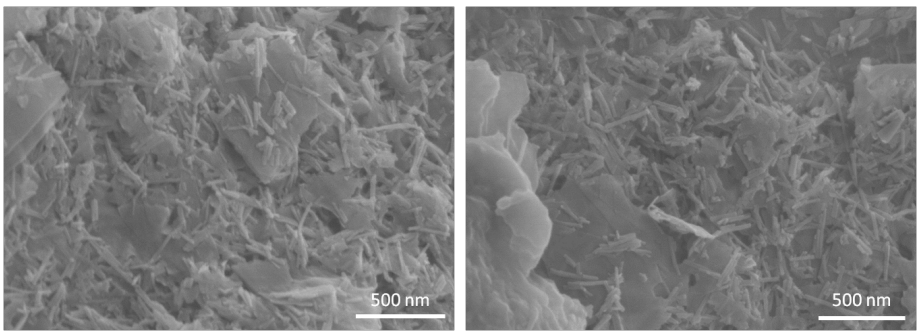

Figure 6.9: SEM images of NiO-graphene electrodes by co-spraying technique

Figure 6.9 shows representative SEM images of the surface of NiO-graphene co-sprayed electrodes. The images suggested a higher overall carbon content in the co-sprayed electrodes compared with the co-synthesised electrodes (Figure 6.2 (b)), which might be expected due to the larger volume of graphene suspension involved in processing (200 ml co-sprayed compared with 30 ml in the co-synthesis vessel). As graphene/NaCholate exhibited no electrochemical activity in the potential window that NiO was electrochemically active, it did not affect the resulting composite electrode capacity directly through double layer or pseudocapacitance contributions.

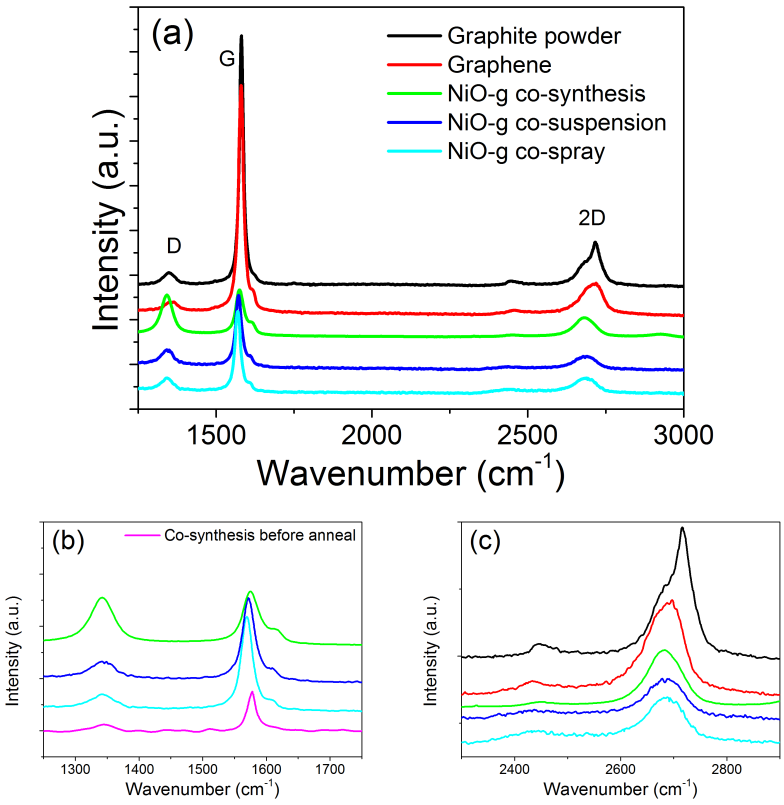

Figure 6.10: (a) Raman spectra of graphene, NiO-g co-synthesis, NiO-g co-suspension and NiO-g co-spray sprayed electrodes (b) zoom in region of D and G peaks (c) zoom in of the 2D peak

The nickel oxide-graphene (NiO-g) composite samples were investigated by Raman spectroscopy. Figure 6.10 (a) shows the Raman spectra of the precursor graphite powder before exfoliation (black) and a sprayed graphene electrode (red) with enlarged areas of interest in Figures 6.10 (b) and (c). The presence of graphene platelets after exfoliation was confirmed by the common graphene D, G and 2D peaks[30] at 1349, 1580 and 2700 cm^{-1} respectively. As expected, the Raman spectra of three NiO-g composite sprayed electrodes (co-synthesis, co-spray and co-suspension) also contained D, G and 2D peaks corresponding to graphene rotation/vibration modes.

The ratio of Raman D to G peak intensity (I_D/I_G) can be used to characterise the number of structural defects in graphene[31–33] and D and G peaks for NiO-g composites are shown more clearly in Figure 6.10 (b). Aqueous exfoliation produced comparatively pristine, defect free graphene with $I_D/I_G = 0.33$ for the graphene-only sample, which was maintained in the co-sprayed electrode. For co-suspension electrodes, there was in increase to $I_D/I_G = 0.52$ suggesting that the high power sonication required to form a stable co-suspension induced defects in the graphene sheets. When NiO was synthesised in the graphene suspension itself (NiO-g co-synthesis), defect concentration showed a much more marked increase to $I_D/I_G = 0.95$, which likely occurred during high-temperature annealing as the additional spectrum in Figure 6.10 (b) shows a low I_D/I_G ratio for the co-synthesis material after hydrothermal synthesis but before annealing. There was no significant underlying Raman response of NiO in the 1250 to 3000 cm^{-1} region of interest.

6.6.1 Electrochemical characterisation

A comparison of CV curves at 10 mV s^{-1} and resulting capacitances for NiO-g composite electrodes as well as NiO electrodes without graphene is shown in Figure 6.11. The processing route had a significant effect on the electrochemical activity, affecting both the voltage of redox peaks (Figure 6.11 (a)) and the charge stored (Figure 6.11 (b)).

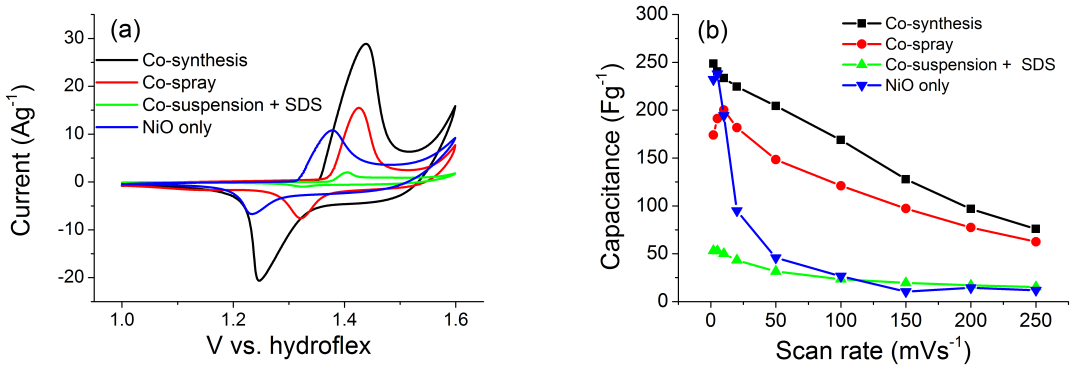

Figure 6.11: (a) Cyclic voltammetry curves for NiO and NiO-g composite electrodes with different processing routes at 10 mV s^{-1} in 2 M KOH electrolyte, and (b) capacitance from cyclic voltammetry for NiO and NiO-g composite electrodes

Electrodes produced through co-suspension exhibited the lowest charge storage, with a capacitance of 53 F g^{-1} at 2 mV s^{-1}. This poor performance was likely due to the necessary addition of sodium dodecyl sulphate (SDS) as a surfactant for suspension stabilisation, which then likely covered the NiO surface, blocking access of electrolyte ions to the active NiO material and increasing through-electrode ion and electron resistance. In contrast, the addition of graphene either through co-synthesis or co-spraying provided for a significant improvement in charge storage behaviour, notably improving capacitance retention at higher scan rates. Co-synthesis electrodes exhibited the highest specific capacitance of 248 F g^{-1} at 2 mV s^{-1}, which reduced

to 100 F g^{-1} at 250 mV s^{-1}, and a highest capacitance for co-sprayed electrodes of 200 F g^{-1} at 10 mV s^{-1}. In both cases, the principle effect of the graphene was concluded to be improved electron transfer throughout the electrode.

The superior performance of co-synthesised electrodes could be attributed to the more intimate contact that can be expected between NiO and graphene as Ni^{2+} ions were able to 'anchor' to surface oxygen groups on the graphene during synthesis,[34, 35] allowing for better electron transfer compared with co-sprayed samples where contact between the two materials only occurred briefly during the comparatively rapid drying on the substrate after deposition. Additionally, the higher number of structural defects within the graphene in co-synthesis electrodes may have facilitated movement of electrolyte ions throughout the electrode whereas the more pristine graphene sheets in the co-sprayed electrodes may block ion access to the inner parts of the electrode.[36]

Galvanostatic charge/discharge cycling over a maximum voltage range of 0.5 V, determined from the CV curves, at a current density of 1 A g^{-1} was performed for NiO and NiO-g composite electrodes and the resulting curves are shown in Figure 6.12. NiO-g co-synthesis electrodes showed qualitatively similar charge and discharge profiles to pure NiO electrodes in Figure 6.12 (b) and (a) respectively, with a flat plateaux in charge and discharge curves for both electrodes at 1.35/1.3 V corresponding to the faradaic charge transfer reaction in Equation 6.1. Discharge times at equivalent current densities were 60 - 100% longer for NiO-g co-synthesis electrodes than for NiO electrodes, which corresponded to their higher specific capacitance and improved charge storage. Co-sprayed samples in Figure 6.12 (c) exhibited less pronounced discharge plateau than NiO and co-synthesised electrodes. A reduction in discharge times occurred when NiO and NiO-g co-synthesis electrodes were contin-

uously cycled that led to a gradual reduction in capacitance, as shown in Figure 6.13. In contrast, co-sprayed NiO-g electrodes showed increasing capacitance up to 100 cycles, which may have been caused by their improved electrode structural integrity due to the higher amount of carbon in the electrode and/or improved physical contact between the two materials as cycling proceeded. NiO-g electrodes from co-suspensions in Figure 6.12 (d) provided negligible charge storage and a large vertical "IR" drop at the start of the discharge, further supporting that their poor electrochemical performance was due to increased resistance caused by the use of SDS in the electrode processing.

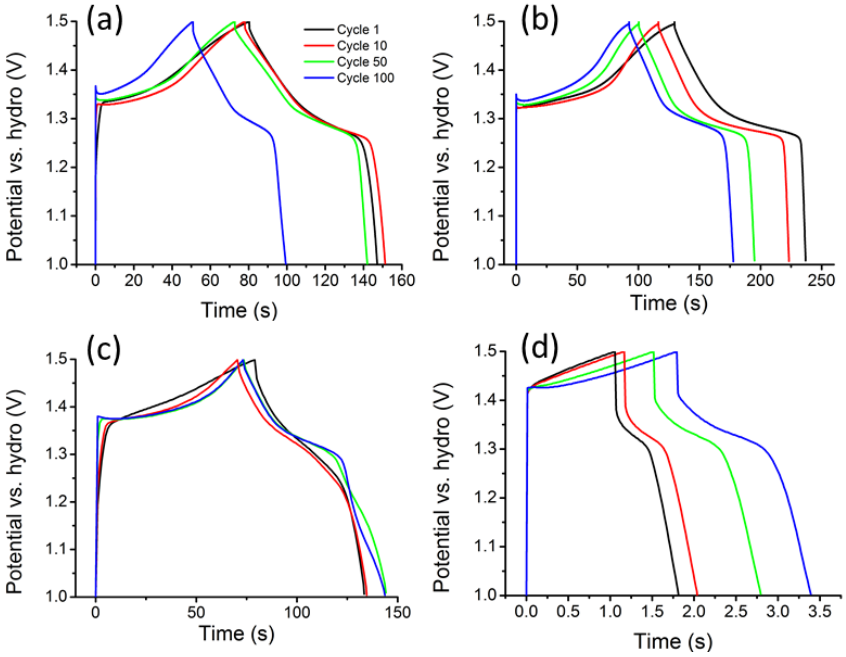

Figure 6.12: Charge discharge graphs for the 2nd, 10th, 50th and 100th cycle for electrodes (a) NiO only (b) NiO-g co-synthesis (c) NiO-g co-spray and (d) NiO-g co-suspension

The improved electron transport afforded by the addition of graphene was further studied by electrochemical impedance spectroscopy over the frequency range 100,000 - 0.01 Hz. Complex plane Nyquist plots of NiO and NiO-graphene composite electrodes taken at the open circuit potential are shown in Figure 6.14. The diameter of

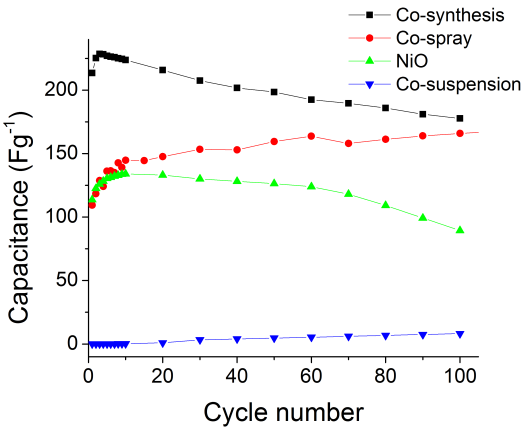

Figure 6.13: Capacitance calculated from discharge curves for NiO and NiO-g composite electrodes

the high frequency semi-circle is commonly related to charge transfer resistance and was estimated to be ∼1500 Ω for the NiO-g co-suspension electrode, compared with ∼50 Ω for NiO and NiO-g co-sprayed, and < 10 Ω for the NiO-g co-synthesis electrodes. Thus, charge transfer behaviour was consistent with capacitances obtained by CV and charge/discharge measurements. Henceforth, all nickel oxide-graphene (NiO-g) electrodes described refer to 'co-synthesis' sprayed electrodes.

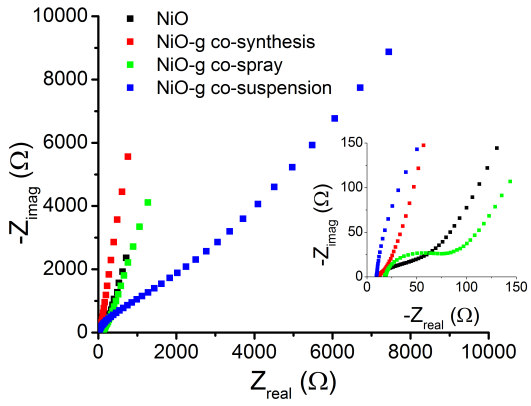

Figure 6.14: Nyquist plots of NiO and NiO-graphene composite electrodes at OCP with the high frequency semi-circle shown in inset

6.6.2 Optimised composite electrode - further tests

Cyclic voltammetry data can be used to probe the reversibility and kinetics of electron transfer reactions in solution, and the CV curves for NiO-g electrodes at scan rates up to 100 mV s^{-1} shown in Figure 6.15 indicate the symmetric behaviour of the anodic and cathodic reaction in this case.

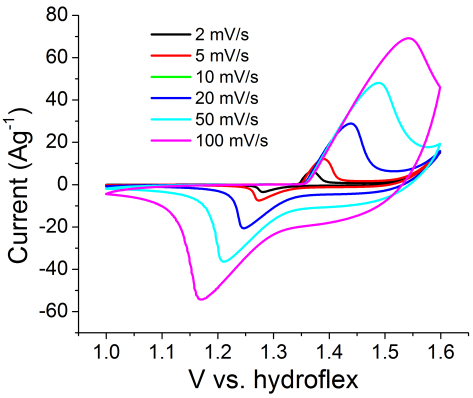

Figure 6.15: Cyclic voltammetry curves for nickel oxide-graphene composite electrodes at scan rates between 2 and 100 mV s^{-1} in 2 M KOH

Using data from these CV curves, Figure 6.16 reveals a strong linear dependance of both the anodic and cathodic reaction peak current with the square root of the scan rate ($\nu^{1/2}$). This behaviour is typical of a "fast" electron transfer process at the electrode/electrolyte interface controlled by linear diffusion kinetics to the electrode surface.[37] The potential separation of peak currents between the anodic and cathodic sweep increases with scan rate, from 100 mV at 2 mV s^{-1} to 380 mV at 100 mV s^{-1}, and further at higher scan rates, which is due to the progressive limitation placed on the reaction due to limited ion diffusion at high scan rates.

To evaluate the rate performance of NiO-g electrodes, galvanostatic charge/discharge cycling was performed at current densities between 1 and 50 A g^{-1} and corresponding

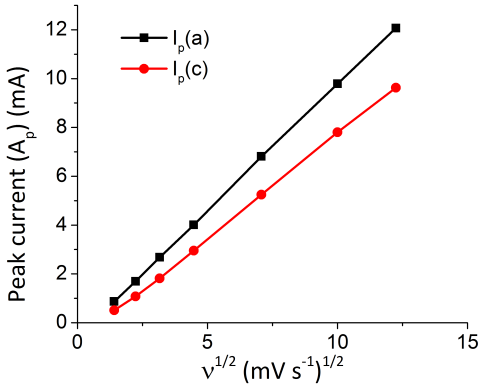

Figure 6.16: Peak current vs square root scan rate

capacitances calculated from the discharge curves according to Equation 6.4 are shown in Figure 6.17. A maximum capacitance of 254 F g^{-1} was obtained at 1 A g^{-1}, which was retained at over 100 F g^{-1} even for extremely high charging currents of 50 A g^{-1}. Capacitances were comparable with, but slightly lower than, NiO-graphene composite electrode manufactured by slurry/casting onto Ni foam[38] where a specific capacitance of 274 F g^{-1} was achieved at 1 A g^{-1} and 220 F g^{-1} at 10 A g^{-1}, compared with 162 F g^{-1} at 10 A g^{-1} in this work.

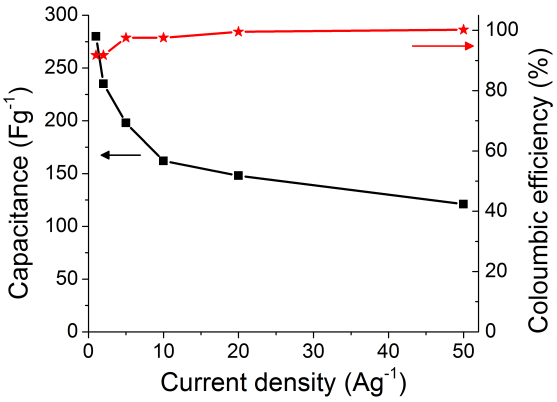

Figure 6.17: Specific capacitance and columbic efficiency of nickel oxide-graphene electrodes from galvanostatic charge/discharge tests at charging current densities of 1 - 50 A g^{-1} in 2 M KOH

The columbic efficiency (η) of cycling was calculated according to:

$$\eta = \frac{t_d}{t_c} * 100 \tag{6.5}$$

where $t_{d/c}$ are the time to discharge/charge respectively. The electrodes showed high columbic efficiencies of over 90 % at all current densities suggesting excellent electrochemical reversibility.

6.6.3 Effect of a nickel foam substrate

Given its relatively widespread use in the literature as a substrate for nickel oxide based supercapacitors, and to test the effect that the substrate/current collector material and morphology may have on energy storage behaviour, the optimised nickel oxide-graphene co-synthesis composite suspension was sprayed onto PEI pre-coated nickel foam, rather than the "flat" ITO coated glass slides previously described. This electrode material/substrate combination is referred to as NiO-g/Ni.

As supplied Ni foam can be expected to provide an enhanced surface area per unit area of current collector compared with the flat ITO glass substrates, and as shown in Figures 6.18 (a) - (c) the foam comprised an extremely open framework, truss-like structure. The nanostructured morphology of the NiO-g was maintained after spray deposition onto this Ni foam, as shown in Figures 6.18 (d) - (f), where the as-deposited nano-structure appeared qualitatively similar to the plan morphology of the same material on ITO coated glass, but now coated over the majority of the Ni foam surface.

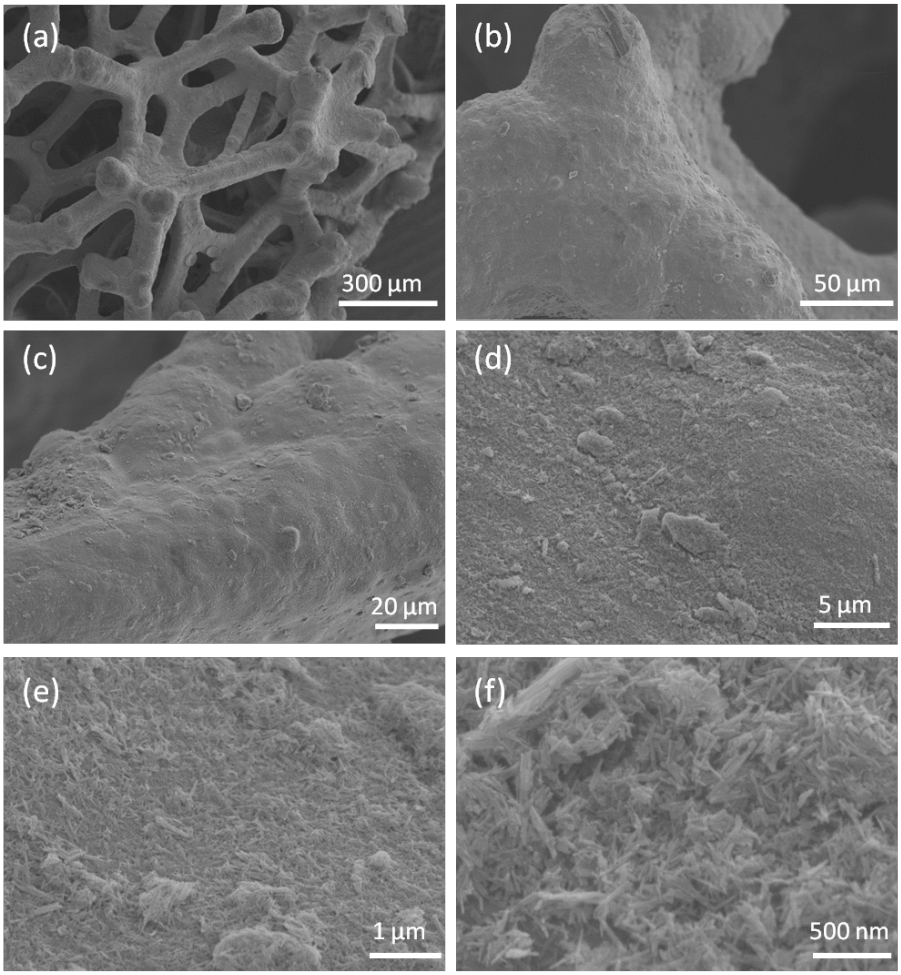

Figure 6.18: SEM image of (a) - (c) macrostructure of NiO-graphene coated Ni foam and (d) - (f) zoom in of NiO-graphene coating

NiO-g/Ni electrodes were first cycled at 50 mV s^{-1} in a three electrode cell under conditions identical to those used for NiO-g/ITO electrodes (Section 6.6.2) and bare Ni foam (Section 6.4) and the resulting CV curves of bare nickel foam (black) and NiO-g/Ni (red) for the 2nd, 50th, 100th and 200th CV cycle are shown in Figure 6.19. From Equation 6.3, the increased area under the CV curve indicated that the NiO-g coating on Ni foam provided a significantly improved charge storage capability compared with Ni foam alone. The increased charge storage must arise from surface redox reactions of the deposited NiO-g material discussed previously, although it

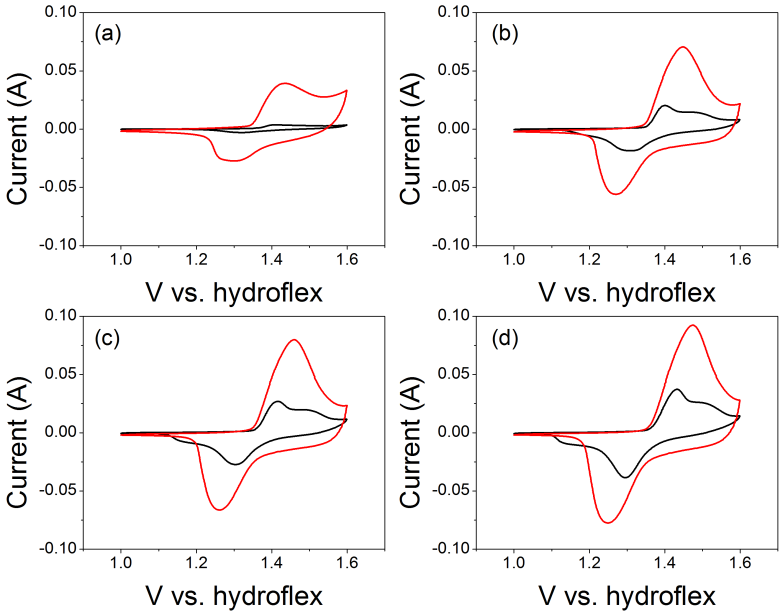

Figure 6.19: CV curves at a scan rate of 50 mV s^{-1} in 2 M KOH for Ni foam (black) and NiO-g on Ni foam (red) for the (a) 2nd (b) 50th (c) 100th and (d) 200th cycle

was not possible to exclude some contribution from the Ni foam substrate. The minimum possible charge storage provided by NiO-g on Ni foam was calculated by subtracting the integrated area under the Ni foam curves from the integrated area under NiO-g/Ni curves at the same cycle number and scan rate:

$$C_s = \frac{(\int IdV_{NiOg/Ni} - \int IdV_{Nifoam})}{(2.\nu.\Delta V.m)} \tag{6.6}$$

Capacitance calculated from Equation 6.3 for NiO-g/Ni electrodes with and without subtracting Ni foam contributions (Equation 6.6) up to 200 cycles are shown in Figure 6.20. When only the raw data is considered, the capacitance of NiO-g/Ni electrodes appeared to almost double from 404 F g^{-1} during cycle 1 to 812 F g^{-1} during cycle 200. However, as already shown in Figure 6.3 (b) this increase in capacitance

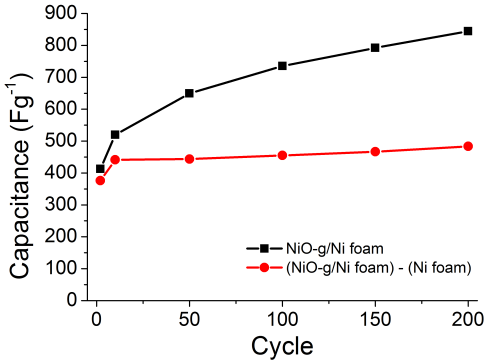

Figure 6.20: Capacitance from CV curves 1) calculated from raw data (black) and 2) calculated subtracting the effect of Ni foam contribution (red)

behaviour also occurred for the Ni foam only when cycled in KOH. When $\int IdV_{Nifoam}$ was subtracted from $\int IdV_{NiOg/Ni}$, a marginal increase in capacitance over the first 10 cycles occurred followed by stabilisation at ~450 F g^{-1}. From microscopy, most of the Ni foam surface was coated with NiO-g, and therefore it was unlikely that there was a majority contribution of the Ni foam surface to electrochemical reactions once spray coated. The approximate method developed here allows for the maximum effect of substrate reactions on behaviour to be estimated. Consequently, it is likely that the "true" specific capacitance of NiO-g on this reactive, high area substrate lies somewhere in between the red and black lines in Figure 6.20.

Figure 6.21 compares specific capacitance as a function of scan rate for NiO-g/ITO glass with NiO-g/Ni (with and without Ni foam contribution considered). Deposition onto Ni foam increased the specific capacitance at all scan rates, including when any Ni foam contributions were accounted for, from 248 to 742 F g^{-1} at 2 mV s^{-1} and from 221 to 319 F g^{-1} at 200 mV s^{-1}. The increase in specific capacitance may be attributed primarily to an increase in surface area from 1 cm^2 for flat ITO electrodes to 8.7 cm^2 for porous Ni foam, assuming coating was possible throughout the Ni foam. The NiO-g nanostructures were deposited in a relatively densely-packed layer,

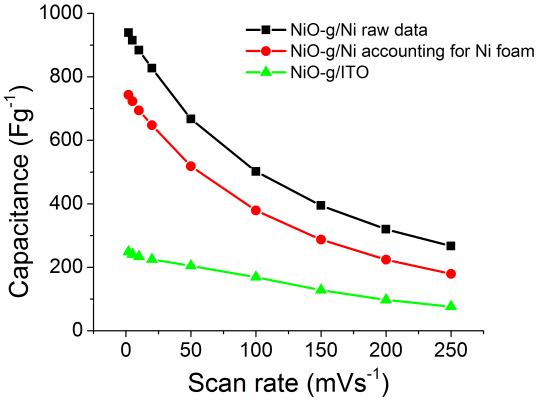

Figure 6.21: Capacitance calculated from cyclic voltammetry at scan rates from 2 to 250 mV s^{-1} for NiO-g composites on ITO coated glass, NiO-g/Ni from raw data and NiO-g/Ni with the contribution from the substrate subtracted

as shown in Figure 6.2 (b), and so the highly porous Ni foam substrate allowed higher accessibility of electrolyte ions to the surface of NiO at comparable electrode mass loading. A higher surface area additionally allowed for thinner film coatings for a similar electrode mass, and therefore facilitated shorter electron and ion diffusion lengths.

Galvanostatic charge/discharge curves for NiO-g/Ni electrodes at charging currents 10 - 100 A g^{-1} are shown in Figure 6.22 (a) and the corresponding capacitance estimated from the discharge curves up to 1000 cycles are shown in Figure 6.22 (b). Specific capacitances for the NiO-g/Ni electrodes of over 300 F g^{-1} were maintained up to an extremely high charge density of 100 A g^{-1}, which is much higher than many reports of nickel oxide/graphene composites that often use charge/discharge current densities as low as 0.2 A g^{-1},[39] and rarely greater than 30 A g^{-1}.[40] Although lower charge/discharge currents often result in higher specific capacitance values, they do not fully highlight the extremely high power potential of these composite electrodes.

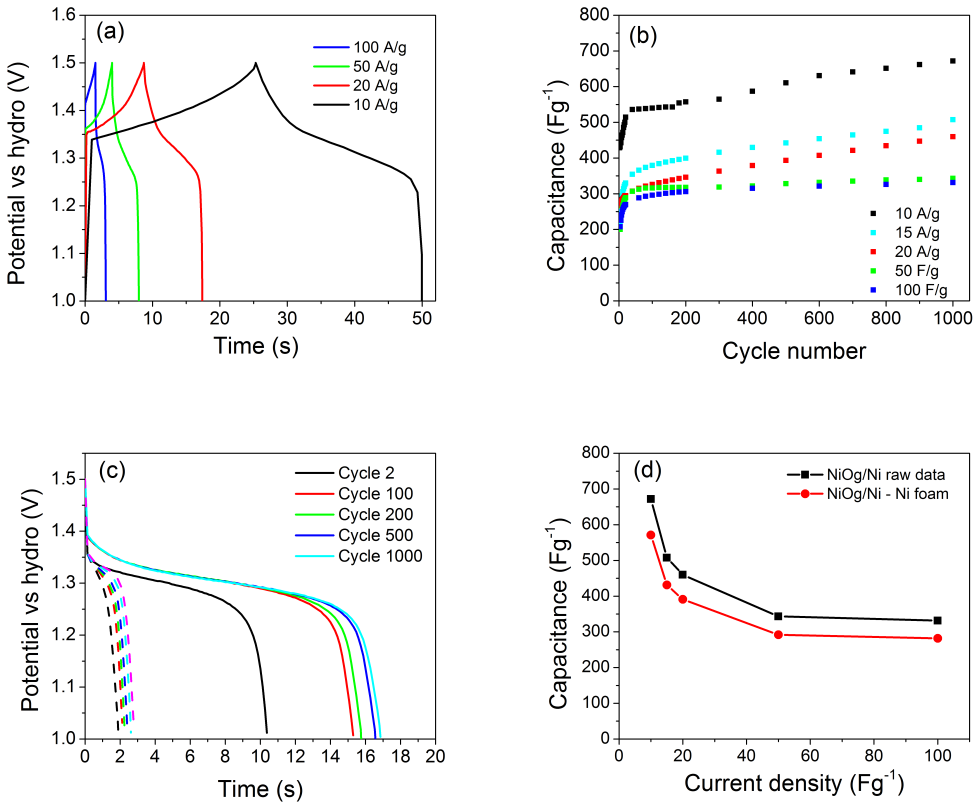

Figure 6.22: (a) Charge and discharge curves for NiO-g/Ni foam electrodes at charge densities 10 - 100 A g^{-1}, (b) capacitance from NiO-g/Ni discharge curves at up to 1000 cycles at charging currents between 10 and 100 A g−1, (c) discharge curves of NiO-g/Ni and Ni foam electrodes at 20 A g^{-1}, and (d) capacitance as a function of charging density for NiO-g/Ni raw data and NiO-g/Ni after Ni foam contribution was removed

Representative discharge curves for NiO-g/Ni (solid lines) and Ni foam (dashed lines) up to 1000 cycles at a discharge current density of 20 A g^{-1} are shown in Figure 6.22 (c). Both electrodes showed an increase in discharge time with cycling, although the increase was much more pronounced for NiO-g/Ni foam electrodes. Similarly, when calculating capacitance from discharge curves according to Equation 6.4, the contribution from Ni foam was approximated and accounted for by subtracting the integrated area under Ni foam alone discharge curves. At all current densities, by cycle 1000, this corresponded to ∼15 % decrease in capacitance, shown in Figure

6.22 (d). The specific capacitance calculated from charge/discharge was higher than reports of nickel oxide nanoflakes grown directly on nickel foam during hydrothermal synthesis[41] with no graphene/conductivity element included, where specific capacitance at 10 A g^{-1} was 383 F g^{-1} compared with 571 F g^{-1} in this work. The sprayed composite electrodes also showed improvements compared with NiO-graphene on Ni foam[42] where the capacitance stabilised at a maximum of 400 F g^{-1} during cycling at a comparatively low discharge current of 2 A g^{-1}. Reports of graphene oxide-NiO composites manufactured through an electrophoretic deposition (EPD) process achieved a specific capacitance of approximately 460 F g^{-1} at a current density of 10 A g^{-1}, less than the capacitance in this work, despite the use of expensive EPD for graphene oxide synthesis.

6.6.4 Conclusions

Nickel oxide-graphene composite electrodes have been prepared using a spray deposition route on ITO coated glass and porous nickel foam substrates. Aqueous suspensions of exfoliated graphene were incorporated to reduce rapid capacitance fading of NiO at high scan rates due to sluggish electron transfer. The processing route utilised for the addition of graphene was explored and a co-synthesis technique shown to result in superior energy storage characteristics due to improved physical interaction and electron transfer between NiO and graphene, and a higher concentration of graphene defects, assumed to aid ion mobility throughout the electrode.

The electrochemical contribution of the substrate for NiO-graphene on Ni foam electrodes, which is often neglected in the literature, was considered and approximations made in an attempt to separate out the contribution to charge storage from each

material. Specific capacitance was greatly affected by the substrate choice, with a maximum capacitance from cyclic voltammetry of 248 F g^{-1} at 2 mV s^{-1} when ITO glass was used compared with between 743 and 940 F g^{-1} for NiO-g/Ni foam composites. For a NiO-g/Ni electrode, high capacitance of over 300 F g^{-1} was sustained at extremely high charging densities of 100 A g^{-1} and charge/discharge stability was maintained up to at least 1000 cycles.

Bibliography

[1] Wruck, D. A. and Rubin, M. *J. Electrochem. Soc.* **140**(4), 1097–1104 (1993).

[2] Liu, K. C. and Anderson, M. A. *J. Electrochem. Soc.* **143**(1), 124–130 (1996).

[3] Nam, K. W. and Kim, K. B. *J. Electrochem. Soc.* **149**(3), A346–A354 (2002).

[4] Zhang, X., Hng, H. H., and Yan, Q. e. a. *Nano Research* **3**(9), 643–652 (2010).

[5] Zhu, Y., Murali, S., and Ruoff, R. S. e. a. *Science* **332**(6037), 1537–1541 (2011).

[6] Wang, Y., Shi, Z., Huang, Y., Ma, Y., Wang, C., Chen, M., and Chen, Y. *J. Phys. Chem. C* **113**(30), 13103–13107 (2009).

[7] Chen, S., Zhu, J., Wu, X., Han, Q., and Wang, X. *ACS Nano* **4**(5), 2822–2830 (2010).

[8] Liu, C., Yu, Z., Neff, D., Zhamu, A., and Jang, B. Z. *Nano Lett.* **10**(12), 4863–4868 (2010).

[9] Zhang, L., Zhou, R., and Zhao, X. S. *J. Mat. Chem.* **20**(29), 5983–5992 (2010).

[10] Zhang, K., Zhang, L., Zhao, X. S., and Wu, J. *Chem. Mater.* **22**(4), 1392–1401 (2010).

[11] Chen, S., Zhu, J., Wu, X., Han, Q., and Wang, X. *ACS Nano* **4**(5), 2822–2830 (2010).

[12] Yan, J., Fan, Z., Wei, T., Qian, W., Zhang, M., and Wei, F. *Carbon* **48**(13), 3825–3833 (2010).

[13] Chen, R., Yu, S., Sun, R., Yang, W., and Zhao, Y. *J. Sol. St. Electrochem.* **16**(11), 3635–3641 (2012).

[14] Wang, D., Li, F., Wu, Z.-S., Ren, W., and Cheng, H. *Electrochem. Comm.* **11**(9), 1729–1732 (2009).

[15] Liu, C., Yu, Z., Neff, D., Zhamu, A., and Jang, B. *Nano Lett.* **10**(12), 4863–4868 (2010).

[16] Mendoza-Sanchez, B., Rasche, B., Nicolosi, V., and Grant, P. S. *Carbon* **52**, 337–346 (2013).

[17] Zhu, X., Dai, H., Hu, J., Ding, L., and Jiang, L. *J. Pow. Sources* **203**, 243–249 (2012).

[18] Bu, Y., Wang, S., Jin, H., Zhang, W., Lin, J., and Wang, J. *J. Electrochem. Soc.* **159**(7), A990–A994 (2012).

[19] Wu, M.-S., Lin, Y.-P., Lin, C.-H., and Lee, J.-T. *J. Mat. Chem.* **22**(6), 2442–2448 (2012).

[20] Xia, X., Tu, J., Mai, Y., Chen, R., Wang, X., Gu, C., and Zhao, X. *Chem. Eur. J.* **17**(39), 10898–10905 (2011).

[21] Bello, A., Makgopa, K., Fabiane, M., Dodoo-Ahrin, D., Ozoemena, K., and Manyala, N. *J. Mat. Sci.* **48**(19), 6707–6712 (2013).

[22] Wang, Y., Zhou, D., Zhao, D., Hou, M., Wang, C., and Xia, Y. *J. Electrochem. Soc.* **160**(1), A98–A104 (2013).

[23] Lotya, M., Hernandez, Y., and Nicolosi, V. e. a. *J. Electrochem. Soc.* **131**(10), 3611–3620 (2009).

[24] Hernandez, Y., Nicolosi, V., Lotya, M., and Coleman, J. N. e. a. *Nature Nanotech.* **3**(9), 563–568 (2008).

[25] Weininger, J. L. and Breiter, M. W. *J. Electrochem. Soc.* **111**(6), 707–712 (1964).

[26] Sattar, M. A. and Conway, B. E. *Electrochim. Acta* **14**(8), 695 (1969).

[27] Nelson, P. A., E. J. M. and Owens, J. R. *J. Electrochem. Soc.* **14**, 524–529 (2002).

[28] Xing, S., Wang, Q., Ma, Z., Wu, Y., and Gao, Y. *Mater. Lett.* **78**, 99–101 (2012).

[29] Wu, M., Huang, Y., Yang, C., and Jow, J. *Int. J. Hydrogen Energ.* **32**(17), 4153–4159 (2007).

[30] Ferrari, A. C., Meyer, J. C., and Geim, A. K. *Phys. Rev. Lett.* **97**(18) (2006).

[31] Vidano, R. and Fischbach, D. *J. Am. Ceram. Soc.* **61**(1-2), 13–17 (1978).

[32] Jorio, A., Ferreira, E., Moutinho, M., Stavale, F., Achete, C., and Capaz, R. *Phys. Status Solidi* **247**(11-12), 2980–2982 (2010).

[33] Canado, L., Jorio, A., Ferreira, E., Stavale, F., Achete, C., Capaz, R., Moutinho, M., Lombardo, A., Kulmala, T., and Ferrari, A. *Nano Let.* **11**(8), 3190–3196 (2011).

[34] Hwang, S., Kim, G., Yun, S., and Ryu, K. *Electrochim. Acta* **78**, 406–411 (2012).

[35] Zhou, G., Wang, D.-W., Yin, L.-C., Li, N., Li, F., and Cheng, H.-M. *ACS Nano* **6**(4), 3214–3223 (2012).

[36] Luo, G., Liu, L., Zhang, J., Li, G., Wang, B., and Zhao, J. *ACS Appl. Mat. Interfaces* **5**(21), 11184–11193 (2013).

[37] Fisher, A. C. *Electrode Dynamics*. Oxford University Press, (1996).

[38] Zhu, Y.-G., Cao, G.-S., Sun, C.-Y., Xie, J., Liu, S.-Y., Zhu, T.-J., Zhao, X., and Yang, H. *RSC Adv.* **3**(42), 19409–19415 (2013).

[39] Bu, Y., Wang, S., Jin, H., Zhang, W., Lin, J., and Wang, J. *J. Electrochem. Soc.* **159**(7), A990–A994 (2012). cited By (since 1996)5.

[40] Wu, M.-S., Lin, Y.-P., Lin, C.-H., and Lee, J.-T. *J. Mat. Chem.* **22**(6), 2442–2448 (2012).

[41] Yan, X., Tong, X., Wang, J., Gong, C., Zhang, M., and Liang, L. *J. Alloy. Comp.* **593**, 184–189 (2014).

[42] Xia, X., Tu, J., Mai, Y., Chen, R., Wang, X., Gu, C., and Zhao, X. *Chem. Euro. J.* **17**(39), 10898–10905 (2011).

Chapter 7

Asymmetric supercapacitor devices with all-sprayed electrodes

7.1 Introduction

Over the last decade there has been a rapid increase in the number of research papers concerning electrode materials for electrochemical capacitors, with the vast majority involving investigations into electrode behaviour in a conventional three electrode electrochemical cell. Although three electrode testing is necessary to evaluate carefully the electrochemical reactions, cycle life and stability window of individual electrodes, for use in practical applications, these single electrodes - such as those described in Chapters 4 and 6 - must be paired to form full-cell devices where one electrode acts as the anode and the other the cathode. Pairing two electrodes in-

evitably reduces the capacitance of the device when compared with the individual electrodes since the cell functions as two capacitors in series. This gives a maximum device capacitance of half of the individual electrodes tested in a three cell set up according to:

$$\frac{1}{C_{cell}} = \frac{1}{C_+} + \frac{1}{C_-} \tag{7.1}$$

where C_{cell} is the capacitance of the device and $C_{+/-}$ are the individual cathode/anode capacitances measured in a three electrode set up. This results in $C_{cell} = \frac{C_+}{2}$ when $C_+ = C_-$ for a symmetric device and C_{cell} being limited by the lowest capacitance electrode where $C_+ \neq C_-$. If gravimetric capacitance is considered, the specific capacitance is reduced further by an additional factor of 2 as the total mass of electrode materials is doubled.

The maximum energy density (Wh L^{-1}) / specific energy (Wh kg^{-1}) provided by a full-cell supercapacitor device is:[1]

$$E_{max} = \frac{1}{2} C \Delta V^2 \tag{7.2}$$

where C is specific capacitance and ΔV is the operating potential of the device. To maximize specific energy, both the capacitance and voltage window must be maximised; however, the square term relating to operating potential means extending ΔV is a more efficient way of increasing specific energy. The capacitance provided by an electrode is an intrinsic property of the active material involved but as shown in earlier chapters, it may be maximised by controlling the morphology/structure of the electrode to increase surface area and enhance electron and ion mobility.

Where an aqueous electrolyte is employed, ΔV is limited by the breakdown (electrolysis) of water with H_2 and O_2 evolution occurring beyond $\Delta V = 1.23$ V. One way the potential limit may be circumvented is through the use of organic electrolytes or room temperature ionic liquids that can provide a potential window of up to 3 V or more.[2, 3] Nonetheless, an aqueous system may still be attractive from an industrial/commercial perspective due to high ion mobilities in aqueous systems and therefore high power delivery, and to avoid the safety risks of expensive, toxic and flammable organic solvents.

To extend the operating potential window of an aqueous device, two non-equivalent electrodes can be paired as anode and cathode with complementary operating voltage windows in the same electrolyte in order to extend hydrogen/oxygen evolution overpotentials. This technique has been widely used in battery systems such as the lead-acid battery that has an operating potential of 2 V in aqueous H_2SO_4.

When considering the performance of full-cell supercapacitors, it is important to retain the high power density of single electrodes while providing a useable specific energy as, since where higher energy densities are pursued, care must be taken not to sacrifice power density so that the device begins to act simply as a low performing battery with few practical applications. For example, a recent activated carbon//$Ni(OH)_2$ asymmetric device reached specific energy of 36 Wh kg^{-1},[4] that was exceptional for a supercapacitor, but the specific power was sacrificed to only 100 W kg^{-1}, which was comparable with the low power performance of a Li-ion battery.

Typical asymmetric supercapacitors consist of one faradaic, or pseudocapacitive, electrode and one EDLC electrode *i.e.* a metal oxide electrode paired with a carbon electrode such as $Ni(OH)_2$//carbon,[5–10] MnO_2//carbon,[11–17] CNT//TiO_2[18] and

RuO_2//carbon.[19, 20] Nickel oxides are sensible candidate materials for asymmetric supercapacitors because of their high theoretical capacitance, excellent cycling stability in KOH but a relatively low active potential window (∼0.5V) in a symmetric full-cell device. Iron oxides have a more negative active potential window than most other transition metal oxides and so are of interest as a higher energy density replacement anode for carbon in asymmetric devices.

In this chapter, the FeO_x/MWNT and NiO-g sprayed electrodes previously described in Chapters 4 and 6 are investigated for their suitability in various full-cell configurations involving carbon black as an EDLC electrode.

7.2 Experimental details

All materials were purchased from Sigma (UK) and used without further purification.

7.2.1 Electrode processing

FeO_x/MWNT and NiO-g electrodes on ITO, stainless steel (SS) and copper foil were prepared as described previously in Chapters 4 and 6 respectively.

High surface area commercial carbon black electrodes, henceforth referred to as SC3 (commercial name), were prepared by sonicating a 5 mg ml^{-1} mixture of SC3 in NMP with 5% PTFE added at 100% ultrasonic amplitude for 5 minutes to form a stable suspension. SC3 suspensions were then sprayed at a flow rate of 1 ml min^{-1} onto ITO, stainless steel (SS) and copper foil substrates heated to 200 °C and pre-treated

with a thin layer of polyethyleneimine (PEI).

ITO and SS substrates were pre-cut to 2 x 1 cm with a 1 x 1 cm section exposed to the atomised spray droplets. Copper foil was coated over a 30 x 30 cm area to allow punching of 8 - 15 mm diameter circular disks for use in swagelok and coin cells.

7.2.2 Electrochemical testing

Individual carbon black (SC3) electrodes were tested by cyclic voltammetry in a three electrode arrangement using aqueous electrolytes (2 M KOH, 0.5 M Na_2SO_3, 0.5 M Li_2SO_4). A Pt coated Ti wire was used as the counter electrode, a calomel electrode (SCE) as reference electrodes in Li_2SO_4 and Na_2SO_3 and a hydroflex electrode as reference electrode in KOH to prevent potential shifting and electrode degradation.

The specific details of the various two electrode electrochemical cell arrangements were dependent on the particular electrolyte and substrate used. For cells using KOH, ITO coated glass substrates were used to avoid substrate-electrolyte interaction. The ITO/glass substrates were conductive only on the single ITO coated face rather than through the substrate and so could not act as a double-sided current collector. Additionally, the brittle glass prevented post-spray modification of the electrode area. These properties precluded use of ITO/glass in standard two-electrode cells (swagelok, button, coin) and so to test the electrochemical behaviour on these substrates, two electrodes were pressed together separated by a glass microfibre membrane (300 μm, Whatman) wetted with KOH, the assembled layers held together with a plastic clip, and then immersed in electrolyte solution.

FeO_x/MWNT and SC3 electrodes deposited on copper foil substrate/current collector were suitable for use in the more device-like swagelok and coin cells. Electrodes were punched from coated copper foil sheets to circular electrodes of 8 - 12 (swagelok) and 15 mm (coin cell) diameter. Coin cells were assembled by layering cathode - wetted glass fibre separator - anode - stainless steel current collector - spring/spacer and packaging in standard coin cell casing before sealing using a hydraulic crimper. Swagelok cells were assembled with two electrodes facing each other, separated by an electrolyte wetted glass fibre separator and held together by pressure applied via the screw/thread.

All electrochemical testing was carried out using a Gamry Reference 600 potentiostat. Cyclic voltammetry was carried out in the optimised potential window at scan rates between 2 and 500 mV s^{-1}. Galvanostatic charge and discharging was carried out at current densities of 0.1 - 20 A g^{-1}. Cycling behaviour was studied by galvanostatic charge and discharging at 1 A g^{-1} for 500 cycles. Specific capacitance values were reproducible to +/- 10 F g^{-1}. Electrochemical impedance spectroscopy was carried out using a face-to-face arrangement submerged in a glass cell of the electrolyte with no separator and an electrode separation distance of 5 mm.

7.3 Results and discussion

7.3.1 Materials and electrode characterisation

Material characterisation data for FeO_x/MWNT and NiO-g electrodes can be found in Chapters 4 and 6 respectively. The SC3 carbon electrodes comprised of carbon nanoparticles that were spray deposited to form electrodes with an average thick-

ness of 5 μm. The specific surface area and micropore volume have been estimated previously to be 3069 m^2 g^{-1} and 0.22 cm^3 g^{-1} respectively.[21]

When two non-identical paired electrodes are charged, any applied voltage will split across the cell according to the capacitance of each electrode, that depends on specific capacitance and deposited mass. To ensure that the maximum cell voltage is achieved, the charge on both electrodes must be balanced *i.e.* $q_+ = q_-$. As $q = m * C * \Delta E$ where m is electrode mass, C is specific capacitance and ΔE is the electrode operating potential window, for two electrode arrangements discussed in this chapter, the mass ratio of anode to cathode material was calculated according to:[22]

$$\frac{m_a}{m_c} = \frac{C_c * \Delta E_c}{C_a * \Delta E_a} \tag{7.3}$$

using the capacitance data from three electrode experiments, and the appropriate mass ratios, which are shown in Table 7.1. For symmetric devices, a 1:1 mass ratio of anode:cathode material was suitable whereas for asymmetric devices, different electrode masses on the anode and cathode were used to balance charge across the electrodes so that one electrode did not degrade quicker than the other if fading were to be problematical. The deposited mass was calculated by weighing substrates before and after spraying and consequently represented the total mass of the electrode, including any conductivity additives (MWNT, graphene) and binder (PTFE), rather than the electrochemically active material only.

Anode	Cathode	Electrolyte	C_a (Fg^{-1})	C_c (Fg^{-1})	ΔE_a (V)	ΔE_c (V)	$\frac{m_a}{m_c}$
FeO_x/MWNT	FeO_x/MWNT	Na_2SO_3 Li_2SO_4	312	312	1.1	1.1	1
FeO_x/MWNT	SC3	Li_2SO_4	148	103	1.1	1	0.63
SC3	NiO-g	KOH	114	248	1	0.6	1.3
FeO_x/MWNT	NiO-g	KOH	49	248	1	0.6	3

Table 7.1: Mass balancing data for iron oxide, nickel oxide and carbon electrodes in various full-cell arrangements

7.3.2 A carbon black supercapacitor electrode

Untreated commercial carbon black has displayed attractive properties as a supercapacitor electrode with high cycling stability and high capacitance in aqueous electrolytes in previous work in the group.[21] Carbon black is low cost, non-toxic and abundant and displays energy storage capabilities in a range of aqueous electrolytes over varying potential ranges with fast kinetics and therefore high power capabilities, making it an ideal candidate for use in asymmetric supercapacitor devices.

To deduce suitable operation potentials for full-cell devices involving SC3 carbon black, sprayed SC3 electrodes were first tested in a three-electrode configuration using 2M KOH, 0.5 M Na_2SO_3 and 0.5 M Li_2SO_4 electrolytes and the resulting cyclic voltammograms at scan rates of 2 - 250 mV s^{-1} are shown in Figures 7.1 (a) to (c) respectively.

All the voltammograms displayed a generally rectangular/parallelogram shape with no significant redox peaks suggesting charge storage was largely double layer (EDLC) in KOH, Li_2SO_4 and Na_2SO_3. The current response at switching potentials lagged slightly in Li_2SO_4 indicating some resistive behaviour and that ion mobility was slowest in this electrolyte. The electrochemical stability window differed in the different

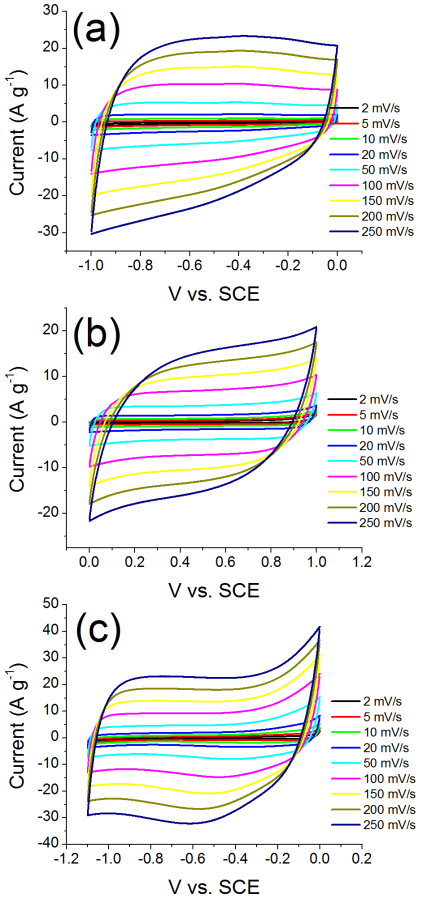

Figure 7.1: Cyclic voltammograms for SC3 carbon in (a) KOH (b) Li_2SO_4 and (c) Na_2SO_3 at scan rates of 2 - 250 mV s^{-1}

electrolytes based on the electrolyte pH and concentration that affected hydrogen and oxygen evolution overpotentials.

In 2 M KOH, the operating potential was between -1 and 0 V vs SCE, which was more negative than the electrochemical window and hydrogen evolution overpotential for NiO-g electrodes in Chapter 6.6.4 (between 1 and 1.6 V vs hydroflex/0 and 0.6 V vs SCE). When SC3 electrodes were cycled in 0.5 M Na_2SO_3, the active potential range was between -1 and 0 vs SCE with oxygen evolution occurring at 0.4 V vs SCE. This directly overlapped with the potential window of FeO_x/MWNT electrode in the same electrolyte suggesting that pairing FeO_x/MWNT with SC3 in Na_2SO_3

would not result in an extended operating potential and no significant improvement in specific energy. However, when SC3 electrodes were cycled in Li_2SO_4, the gas evolution overpotentials shifted to higher potentials and SC3 electrodes were then active between 0 and 1 V vs SCE, and were therefore potentially suitable as an asymmetric cathode for FeO_x/MWNT in Li_2SO_4.

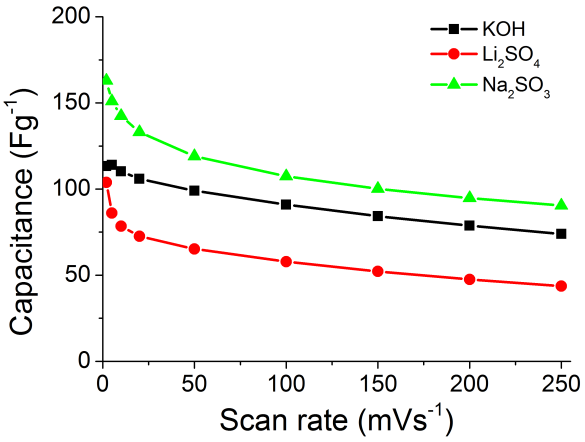

Figure 7.2: Capacitances from the CV curves of SC3 in 0.5 M Na_2SO_3 (green), 0.5 M Li_2SO_4 (red) and 2 M KOH (black)

Specific capacitances calculated from cyclic voltammetry at scan rates 2 - 250 mV s^{-1} are shown in Figure 7.2. When compared with the metal oxides in earlier chapters, there was much lower capacitance fading at high scan rates. Electrodes cycled in KOH showed the lowest capacitance fading as the relatively small, mobile OH^- ions allowed for improved kinetics compared with larger, lower mobility $SO_{3/4}^{2-}$ ions.[23]

7.3.3 An iron oxide symmetric capacitor

To first test the behaviour of a symmetric supercapacitor arrangement, FeO_x/MWNT symmetric two-electrode devices were constructed using a swagelok cell arrangement.

Copper foil was chosen as the substrate/current collector that provided low mass and high mechanical flexibility. The separator was pre-soaked in 0.5 M Na_2SO_3 electrolyte solution as FeO_x/MWNT electrodes exhibited preferable energy storage behaviour in this electrolyte (Chapter 4). The symmetric devices were characterised by cyclic voltammetry and galvanostatic charge/discharge operating over potentials of 1.2 and 1 V respectively.

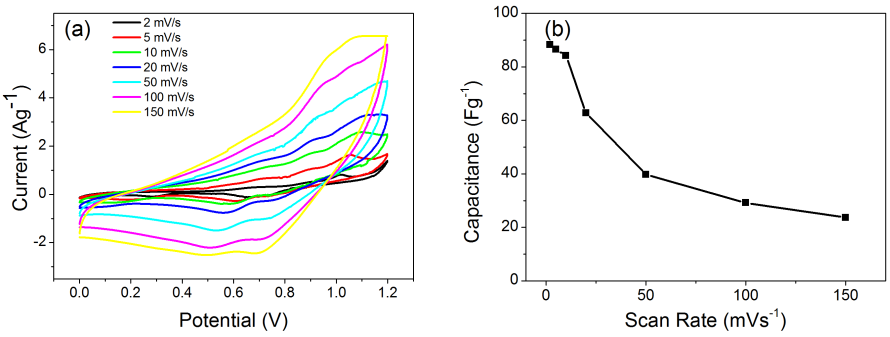

Figure 7.3: (a) Cyclic voltammograms and (b) capacitance calculated from CV curves for FeO_x/MWNT full-cell

Figure 7.3 (a) shows cyclic voltammetry curves and (b) the corresponding estimated capacitances at scan rates between 2 and 150 mV s^{-1} in Na_2SO_3. The symmetric FeO_x/MWNT devices exhibited a maximum capacitance of 88 F g^{-1} at a scan rate of 2 mV s^{-1} that rapidly decayed to less than 30 F g^{-1} at 100 mV s^{-1}, and were lower than single electrodes in a three cell configuration (maximum of 312 F g^{-1}), as expected from Equation 7.1.

The cycling behaviour measured by galvanostatic charge/discharging in Na_2SO_3 is shown in Figure 7.4 for current densities of 0.1 to 1 A g^{-1}. Both the charging and discharging profiles exhibited non-linear behaviour, particularly above 0.9 V, due to the pseudocapacitive reactions of SO_3^{2-}, although the plateaux and inflection potentials were not as obvious as those in the single electrode tests, especially during

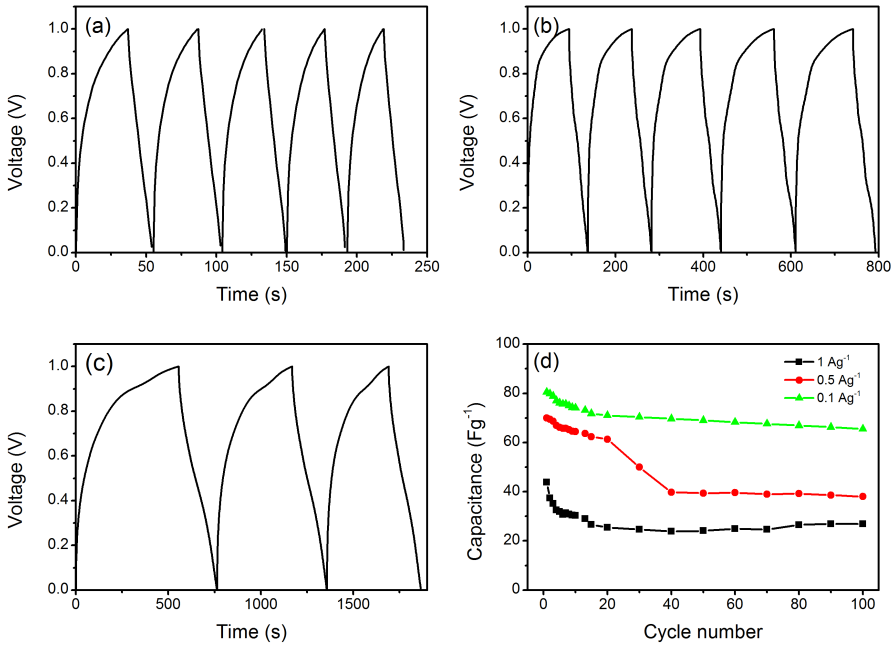

Figure 7.4: Charge discharge curves of FeO_x/MWNT symmetric cells at a current density of (a) 1 A g^{-1}, (b) 0.5 A g^{-1} and (c) 0.1 A g^{-1}

discharge. After 100 cycles, capacitance retention was 66% at 1 A g^{-1} and 75% at 0.1 A g^{-1}, which falls below the rule-of-thumb 80% fading of initial capacitance.

7.3.4 An iron oxide - carbon black asymmetric supercapacitor

Most reports of asymmetric supercapacitors use a carbon-based anode[4–8, 11–20, 24–27] to provide high stability and high hydrogen evolution overpotential. Despite the potential increase in specific energy due to pseudocapacitive reactions, as well as this high hydrogen evolution overpotential, low cost and environmental stability, there have been few reports of iron oxide anodes in asymmetric supercapacitor devices: iron oxide has been paired successfully with MnO_2[28, 29] in aqueous electrolytes and CNTs[30] and activated carbon[31] in non-aqueous systems.

FeO_x/MWNT electrodes were investigated for their suitability in an asymmetric two-electrode configuration using an SC3 electrode as the cathode and a Li_2SO_4 electrolyte. As Li_2SO_4 is benign and non-corrosive, a copper foil substrate/current collector was used and so the device could be tested utilizing swagelok and coin cells with a glass-fibre separator. CV curves of FeO_x/MWNT and SC3 single electrodes in Li_2SO_4 are shown in Figure 7.5. The FeO_x/MWNT electrode response was pseudocapacitive with two clear redox peaks at -0.9/-0.4 V vs SCE suggesting charge storage arose from both double layer capacitance and a pseudocapacitive reaction at the iron oxide surface. The hydrogen evolution reaction occurred at potentials <-1 V vs SCE. The SC3 electrode response was largely rectangular showing the beginning of oxygen evolution at 1 V vs SCE suggesting that cathodic charge storage was due to primarily double later capacitance. The electrochemical stability windows of the two electrodes therefore overlapped across a common voltage range, indicating that cell voltages of up to 2 V may be possible for an asymmetric full-cell arrangement.

To elucidate the applicable operating voltage window (OVW) for the asymmetric cell, FeO_x/MWNT-SC3 devices with a mass ratio of $\frac{m_a}{m_c} = 0.63$ were cycled at 50 mV s^{-1} with increasing maximum cell potentials from 0.5 V to 2 V, and the resulting CV curves are shown in Figure 7.5 (b). When the OVW was limited to <1.2 V a constant current response occurred with a rectangular CV curve as charge storage arose only from double layer capacitance. Small deviations in the CV curves in the form of superimposed peaks emerged at operating potentials >1.2 V due to the onset of previously identified pseudocapacitive reactions in the FeO_x/MWNT electrode. Capacitances estimated from the CV curves in Figure 7.5 (b) are shown in Figure 7.5 (c) and indicated a sharp increase at an OVW of 1.5 V as the FeO_x pseudocapacitive reactions were activated. There was an increase in capacitance up to the maximum OVW of 2 V, and so 2 V was chosen as a suitable cell potential for

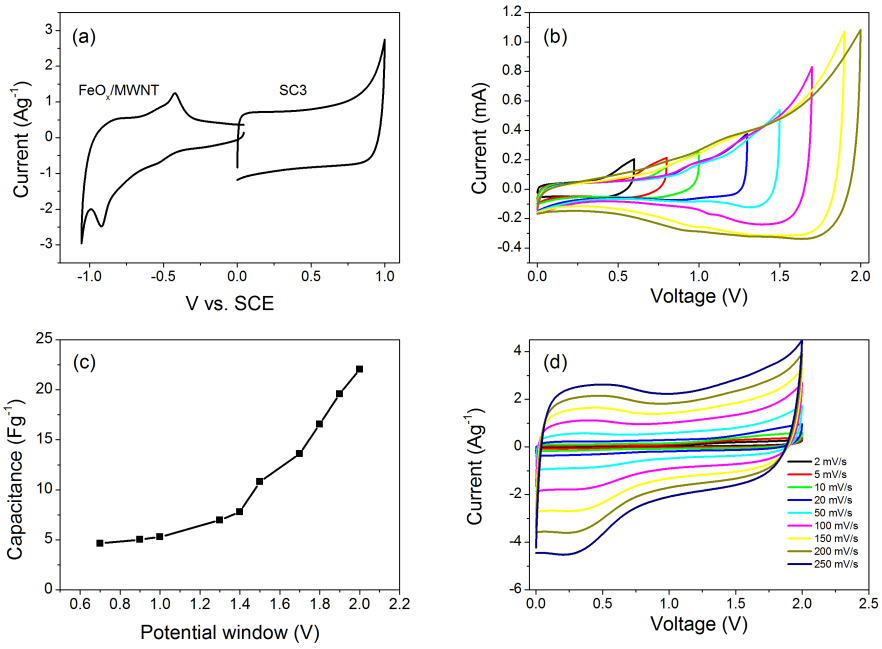

Figure 7.5: (a) Cyclic voltammograms of FeO_x/MWNT and SC3 carbon in a three electrode arrangement in 0.5 M Li_2SO_4 electrolyte at a scan rate of 10 mV s^{-1}, (b) FeO_x/MWNT-SC3 two electrode cell across different potential windows at a scan rate of 50 mV s^{-1}, (c) capacitance calculated from CV curves in (b) and, and (d) FeO_x/MWNT-SC3 two electrode arrangement at scan rates of 2 - 250 mV s^{-1} in Li_2SO_4

the FeO_x-SC3 arrangement.

Galvanostatic charge/discharge studies were performed on FeO_x/MWNT-SC3 devices at charging currents between 2.5 and 15 A g^{-1} and the resulting charge/discharge curves for the 500th cycle are shown in Figure 7.6 (a). There was a relatively large IR drop of approximately 180 mV on current switching, due to ohmic resistance across the swagelok cell caused by both the intrinsic electrode resistance and inhibited mobility across the separator. This might be improved by optimising the separator thickness and material to maximise ion mobility, and by improved cell design to maximise contact between the electrode material/current collector and electrode/separator.

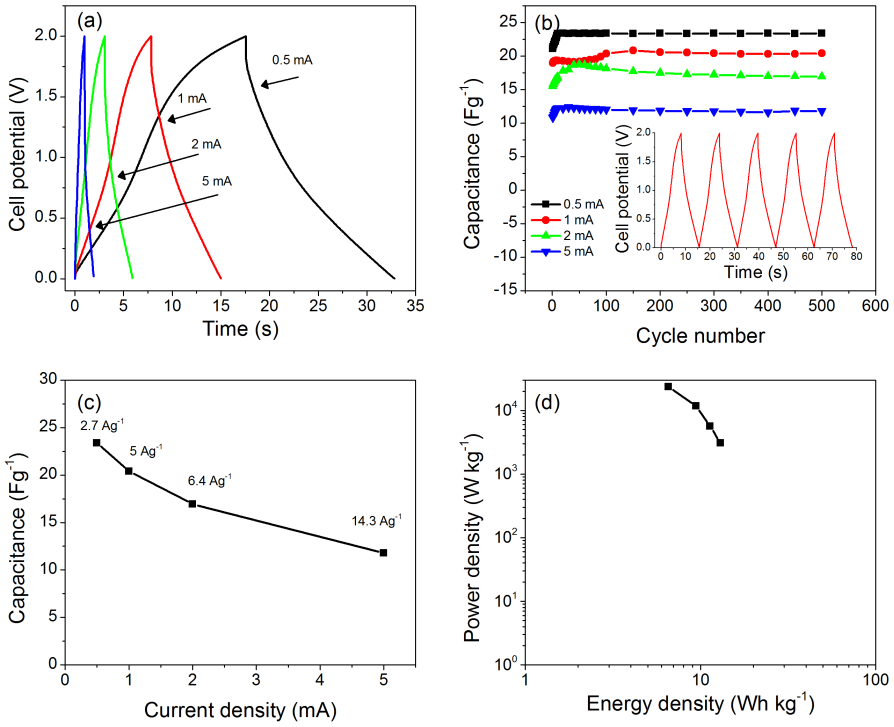

Figure 7.6: (a) 500th charge/discharge cycle for FeO_x/MWNT-SC3 cells at charge densities 0.5 - 5 mA (b) Capacitance from charge/discharge cycling test with 5 cycles at 2 mA shown inset (c) Capacitance as a function of discharge current (d) Specific power and energy for FeO_x-SC3 cells from charge/discharge cycling

Both charge and discharge curves displayed a non-linear response to a constant current due to the pseudocapacitive activity of the FeO_x/MWNT electrode. To test the stability of the arrangement, devices were subject to 500 charge/discharge cycles and the capacitance calculated from discharge curves is shown in Figure 7.6 (b) with the inset figure showing 5 consecutive charge/discharge cycles at a charging current of 2 mA. After an initial increase in capacitance over the first 10 - 100 cycles as the electrode/separator/electrode arrangement settled, the capacitance stabilised at all current densities.

Specific energy E and power W for the device were calculated from these capaci-

tances using Equations 7.2[26, 27, 32, 33] and

$$W = \frac{E.D.}{t} \tag{7.4}$$

respectively where t is the discharge time (h) after any IR drop occurred. Figure 7.6 (d) shows a maximum specific energy of 13 Wh kg^{-1} at a specific power of 3,060 W kg^{-1} which reduced to 6.6 Wh kg^{-1} at a specific power of 23,600 W kg^{-1}. These energy and power densities are discussed further in terms of the other configurations studied later.

7.3.5 A nickel oxide - carbon black asymmetric supercapacitor

The combination of a nickel oxide or hydroxide cathode with a carbon anode is one of the most commonly explored asymmetric supercapacitor systems. Most often a faradaic, battery like nickel cathode in the form of $Ni(OH)_2$ to provide high energy potential is paired with a carbon EDLC anode to provide high power potential ($Ni(OH)_2$//AC,[5, 8] $Ni(OH)_2$//CNT[7, 10] $Ni(OH)_2$//graphene[6]), however it is also possible to use a pseudocapacitive NiO cathode (NiO//AC,[24] NiO//rGO[25]).

NiO-graphene (NiO-g) composite electrodes were tested in a two-electrode asymmetric configuration with an SC3 electrode as the anode and a 2 M KOH electrolyte. As the electrolyte necessary for NiO pseudocapacitive reactions was KOH, the substrate/current collector used was ITO/glass and electrodes were pressed together, separated by a wetted glass fibre separator, as described in section 7.2.2. CV curves of individual NiO-g and SC3 electrodes tested in a three electrode cell with 2 M

KOH electrolyte are shown in Figure 7.7 (a). NiO-g electrodes exhibited pseudocapacitive behaviour between 1 and 1.6 V vs hydroflex with large, reversible redox peaks at 1.25/1.41 V, while SC3 displayed double layer capacitive behaviour with a rectangular current response between 0 and 1 V vs hydroflex. The combination of these two materials indicated that a cell voltage of 1.6 V may be possible for a two electrode configuration.

CV curves of two-electrode devices with a mass ratio of $\frac{m_a}{m_c} = 1.3$ cycled at 50 mV s^{-1} at operating voltage windows (OVW) between 0.5 and 1.9 V are shown in Figure 7.7 (b). When the OVW was <0.8 V, the CV curves displayed a quasi-rectangular shape, suggesting primarily double-layer capacitance. As the OVW reached 0.8 V, gentle peaks emerged as redox activity/pseudocapacitance began on the NiO-g cathode. The redox peaks continued to increase in height to a maximum at an OVW of 1.6 V, beyond which the peaks became distorted due to gas evolution reactions.

Corresponding capacitances from Figure 7.7 (b) are shown in Figure 7.7 (c), reaching a maximum of 21 F g^{-1} when OVW = 1.7 V, above which electrode degradation caused capacitance fading. Although a maximum capacitance was achieved at OVW = 1.7 V, the half cell behaviour suggested that oxygen evolution may occur at $\sim$ 1.6 V, and so the device was cycled over a range of scan rates at an operating voltage of 1.6 V to maximise the operating potential and capacitance without excessively undermining cycle life. CV curves of the two electrode NiO-g-SC3 device operated at 1.6 V at scan rates of 2 - 200 mV s^{-1} are shown in Figure 7.7 (d) with the NiO-g redox activity indicated by the current peaks at $\sim$0.4 and $\sim$1 V, which was largely maintained at all scan rates investigated.

Although cyclic voltammetry can be used to evaluate qualitatively the electrochemical behaviour of a cell, it has been suggested[34, 35] that a more accurate method

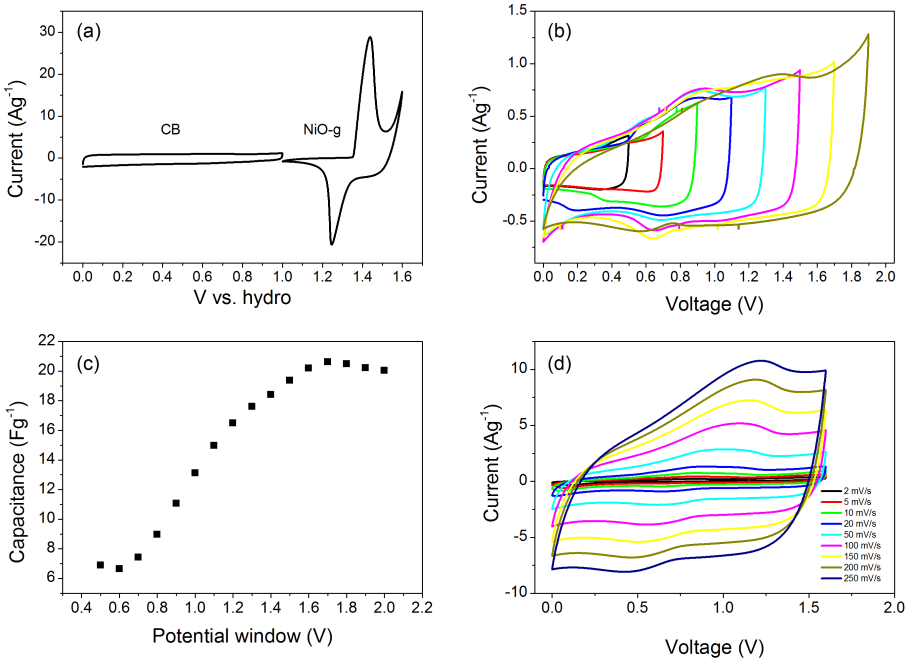

Figure 7.7: (a) Cyclic voltammograms of SC3 carbon and NiO-g in a three electrode arrangement in 2 M KOH electrolyte at a scan rate of 10 mV s^{-1}, (b) cyclic voltammetry curves of SC3-NiO-g two electrode cell across different potential windows at a scan rate of 50 mV s^{-1}, (c) capacitance calculated from CV curves in (b) as a function of operating potential, and (d) cyclic voltammetry curves of a SC3-NiO-g two electrode cell at scan rates of 2 - 250 mV s^{-1}

of determining the highest acceptable voltage of a cell is to use electrochemical impedance spectroscopy (EIS). Because of the discrepancy in the apparent optimum OVW from cyclic voltammetry tests, EIS was performed on two-electrode cells at various cell polarizations and at frequencies between 100,000 and 0.01 Hz. The impedance behaviour was modelled and fitted using the equivalent circuit shown in Figure 7.8, which has been suggested for an asymmetric supercapacitor containing one EDLC and one pseudocapacitive electrode.[16, 34] According to the model, R_{ESR} represents the equivalent series resistance of the system which encompasses electrolyte resistance and resistance through the electrode, R_{ct} represents double layer charge transfer resistance, C_{ct} represents double layer charge transfer capacitance, W accounts for a Warburg coefficient caused by finite diffusion within electrode pores

and C_{cell} represents the cell capacitance. Both capacitor elements were modelled as a constant phase element (CPE) that accounts for imperfections in the electrode surface that cause rotation in the low frequency region of the Nyquist plot by (1-α) x 90°. These imperfections can be thought of as arising from a combination of pseudocapacitance in the NiO-g electrode and general electrode defects, roughness and porosity.

Nyquist plots of SC3-NiO-g cells at cell voltages of 1.4 - 1.7 V are shown in Figure 7.9, with an inset showing the high frequency region.

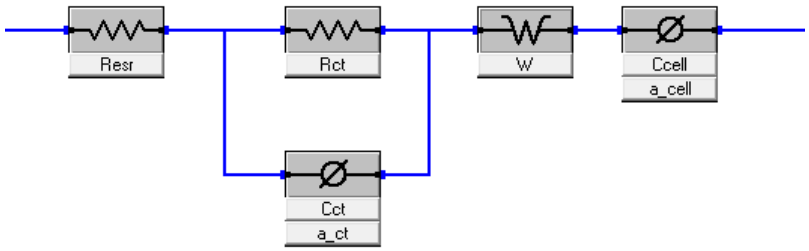

Figure 7.8: Equivalent circuit used to model the SC3-NiO-g cell

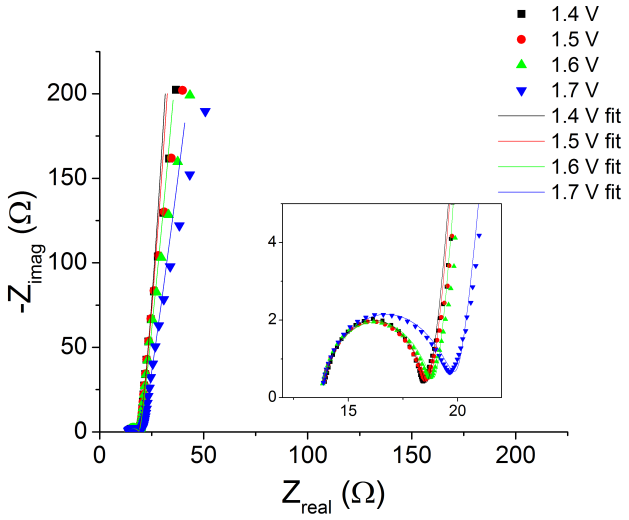

Figure 7.9: Nyquist plots of a SC3-NiO-g cell at cell potentials of 1.4 - 1.7 V

Best-fit values of the elements in Figure 7.8 from the EIS spectra in Figure 7.9 are

Model best-fit parameters	Cell OVW			
	1.4 V	1.5 V	1.6 V	1.7 V
R_{ct} (Ω)	4.6	4.9	5.2	6.3
R_{ESR} (Ω)	14	14	13.6	13.6
W ($\Omega s^{-\frac{1}{2}}$)	7	6.5	5	5.5
C_{ct} mF	0.01	0.02	0.04	0.07
α_{ct}	0.98	0.98	0.96	0.94
C_{cell} mF	10	10	10	10.8
α_{cell}	0.90	0.86	0.82	0.76
Goodness of fit	$0.87\text{x}10^{-4}$	$0.99\text{x}10^{-4}$	$1.21\text{x}10^{-4}$	$2.18\text{x}10^{-4}$

Table 7.2: Fitting parameters of equivalent circuit in figure 7.8 at SC3-NiO-g cell potentials of 1.4 - 1.7 V

shown in Table 7.2. To be considered an acceptable fit of the model to actual behaviour, the 'goodness of fit' parameter should be approximately 1 x 10^{-4}, which is equivalent to a 1% difference between the calculated and measured impedance.[36] All the best-fit values met this criteria and therefore the model was considered reasonable. R_{ct} increased from 4.6 to 6.3 Ω as cell potential increased from 1.5 to 1.7 V because the barrier to ion exchange increased. A CPE can be considered an acceptable substitution for a capacitor element in an equivalent circuit model when $\alpha \simeq 0.9$. At 1.4 and 1.5 V $\alpha = 0.9$ and 0.86 respectively, however, once the cell potential was at 1.6 V, $\alpha = 0.82$ and at 1.7 V, $\alpha = 0.76$, which suggested that another charge transfer process (gas evolution) had begun to occur and that the highest acceptable cell potential was 1.5 V if cycle life were to be preserved, despite the higher capacitance at 1.6 V and 1.7 V from cyclic voltammetry. Therefore subsequently, for charge/discharge testing and for specific energy and power estimations, a maximum cell potential of 1.5 V was used.

The galvanostatic charge/discharge behaviour of SC3-NiO-g two electrode cells up to 1.5 V is shown in Figure 7.10. Charge/discharge curves at current densities between 0.5 and 5 mA in Figure 7.10 (a) displayed a typical non-linear shape due to the

pseudocapacitive NiO-g redox activity with a small IR drop of ∼40 mV in all cases. Excellent capacitance retention of >98% was maintained after 500 charge/discharge cycles after an initial increase in the first 15 cycles due to so-called "conditioning" of the NiO-g electrode, previously seen in other reports.[37]

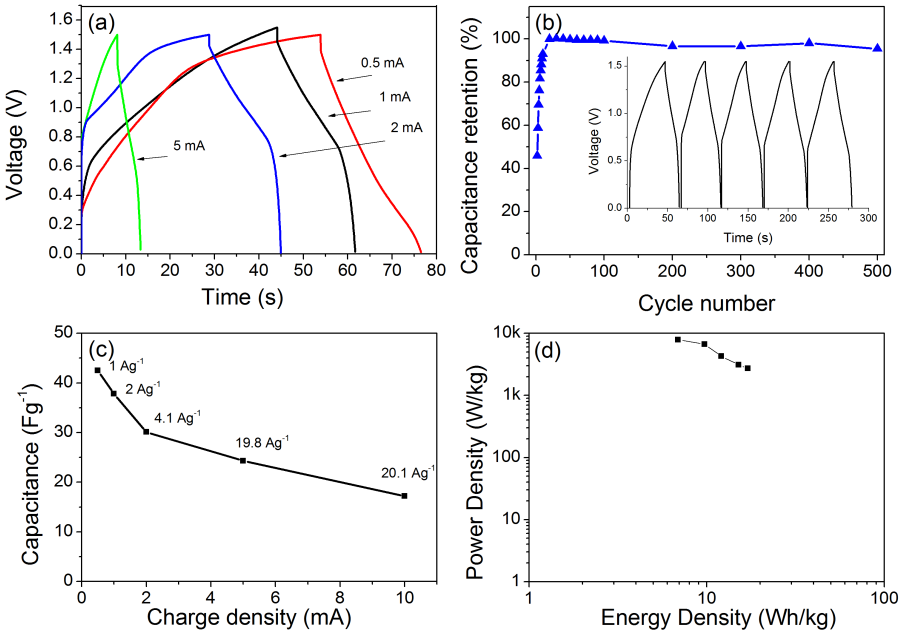

Figure 7.10: (a) Charge/discharge curves of SC3-NiO-g two electrode cells at scan rates of 0.5 - 5 mA, (b) capacitance retention for cycling at 2 mA/cm^{-1}, (c) capacitance from discharge curves, and (d) Ragone plot of SC3-NiO-g two electrode cells

Energy and power densities estimated from discharge curves after conditioning cycles are shown in Figure 7.10 (d), with a maximum specific energy of 17 Wh kg^{-1} at a specific power of 2,800 W kg^{-1}, which reduced to 7 Wh kg^{-1} at a high specific power of 7,900 W kg^{-1}. These energy and power densities are discussed in terms of the other configurations studied later.

7.3.6 An iron oxide - nickel oxide asymmetric supercapacitor

The combination of two transition metal oxides as anode and cathode in an asymmetric configuration has not been widely reported, probably due to the increased likelihood of capacitance fading, high electrode resistance and slow reaction kinetics and therefore lower power potential, when compared with arrangements using one EDLC (usually carbon) arrangements. Of the relatively few papers, $FeO_x//MnO_2$,[28, 29] $VN//NiO$[38, 39] and $Ta_2O_5//RuO_2$[40] arrangements described relatively low power densities, usually not exceeding 3 kW kg^{-1} and often dropping to lower than 0.5 kW kg^{-1} when energy densities were increased above 15 Wh kg^{-1}.

FeO_x/MWNT-NiO-g configurations were investigated in a face-to-face two-electrode arrangement on ITO/glass substrates, 2 M KOH electrolyte and a glass fibre separator. Cyclic voltammetry curves of the FeO_x/MWNT and NiO-g individual electrodes in KOH at a scan rate of 50 mV s^{-1} are shown in Figure 7.11 (a). From the pseudo-rectangular CV with no apparent redox activity, the charge storage mechanism on the FeO_x/MWNT anode in KOH involved relatively weak double layer capacitance only whereas the charge storage on the cathode involved surface-located pseudocapacitance. As there were no through-crystal faradaic reactions, compared with $Fe_2O_3//Ni(OH)_2$ devices previously reported,[41, 42] this arrangement is more accurately described as an asymmetric supercapacitor rather than an iron-nickel battery. Due to the large disparity between the charge on each electrode over the respective potential windows, the mass ratio of this device was much greater than the other arrangements already described, at $\frac{m_a}{m_c} = 3$ - although this was still lower than asymmetric devices that combine an EDLC electrode with a battery-like electrode

where $\frac{m_a}{m_c}$ can exceed 5.[7, 8] From the individual electrode CV curves, a maximum two-electrode cell voltage of 1.8 V may be possible before gas evolution occurs.

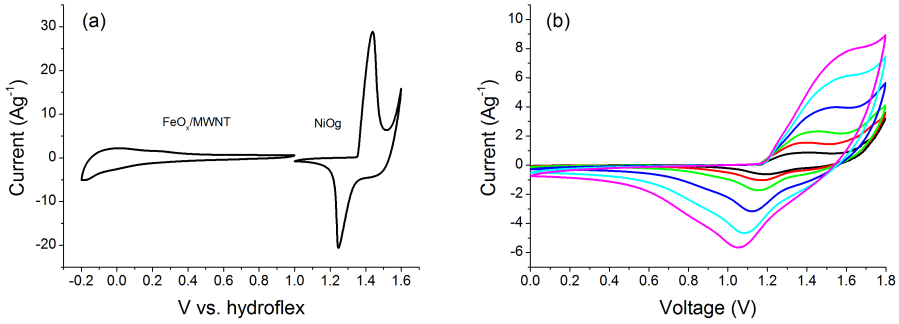

Figure 7.11: Cyclic voltammograms of FeO_x/MWNT and NiO-g (a) each electrode in a three electrode arrangement in 2 M KOH electrolyte at a scan rate of 10 mV s^{-1} and (b) in a two electrode arrangement at scan rates of 2 - 250 mV s^{-1}

Cyclic voltammetry curves of two electrode cells up to 1.8 V at scan rates between 2 and 250 mV s^{-1} are shown in Figure 7.11 (b) where the pseudocapacitive redox reaction of NiO-g occurred at 1.1 (anodic) and 1.2 (cathodic) V, which were maintained at scan rates of up to 250 mV s^{-1}.

To evaluate again the maximum acceptable OVW, EIS was performed using the model described in Figure 7.8 but where the EDLC carbon anode was replaced by a (largely) EDLC FeO_x anode. The resultant Nyquist plots and best-fit values to the model are shown in Figure 7.12 and Table 7.3 respectively.

Considering the α value of the cell CPE, at potentials of 1.4, 1.5 and 1.6 V, α= 0.87, 0.88 and 0.89 respectively, which suggested that these were acceptable cell potentials for the cell to be operating as an acceptable capacitive arrangement. However, at a cell potential of 1.7 V, α = 0.69, which was too low for the model to represent the real, physical process occurring in the cell. From the shape of the Nyquist plot in the medium and low frequency regions, a second charge transfer process with a

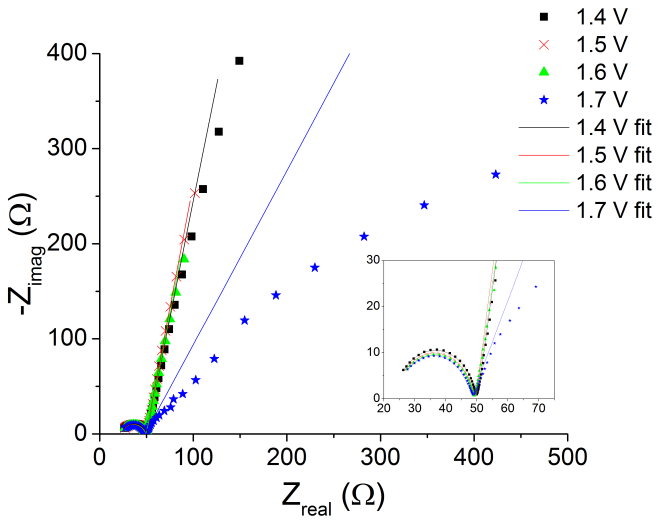

Figure 7.12: Nyquist plot of FeOx/MWNT-NiO-g cell in 2 M KOH

Model best-fit parameters	Cell OVW			
	1.4 V	1.5 V	1.6 V	1.7 V
R_{ct} (Ω)	27	26.5	26	24
R_{ESR} (Ω)	23	23	23	24
W ($\Omega s^{-\frac{1}{2}}$)	4.31 x10^{-4}	0.006	5	10.5
C_{ct} mF	0.5	0.75	1	0.5
α_{ct}	0.84	0.82	0.81	0.84
C_{cell} mF	840	820	810	840
α_{cell}	0.87	0.88	0.89	0.68
Goodness of fit	2.88x10^{-4}	0.78x10^{-4}	0.52x10^{-4}	3.11x10^{-2}

Table 7.3: Fitting parameters of equivalent circuit in figure 7.8 at FeO_x/MWNT-NiO-g cell potentials 1.4 - 1.7 V

different time constant now occurred, evidenced by the emergence of a second broad semi-circle. This may be due to an underlying pseudocapacitive/faradaic reaction of the FeO_x[41–43] or the beginning of gas evolution reactions on the electrodes. The charge transfer resistance (R_{ct}) of the FeO_x/MWNT-NiO-g cell was much larger than cells with a carbon electrode ($\sim$ 25 Ω *cf* $\sim$ 5 Ω) because of the higher characteristic resistance brought about by the combination of two transition metal oxide electrodes, despite the use of MWNTs and graphene to enhance electrode conductivity.

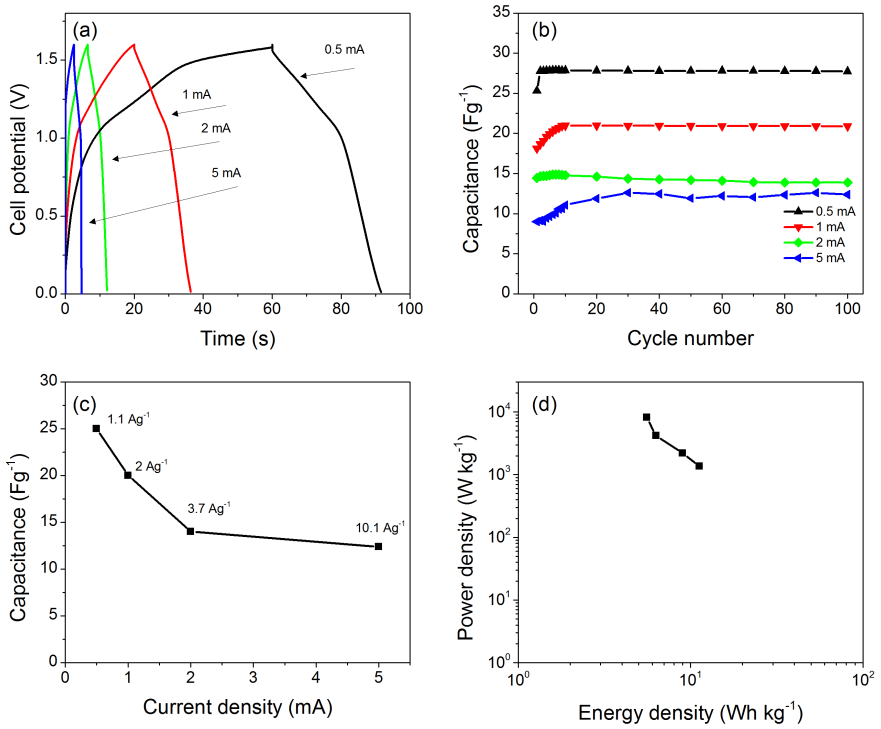

Figure 7.13: (a) Cyclic charge/discharging data for FeO_x/MWNT-NiO-g cells at 0.5, 1 and 2 mA/cm^2, (b) capacitance cycling data, (c) capacitance as a function of current density, and (d) specific energy and power

The charge/discharge behaviour of FeO_x/MWNT-NiO-g cells is shown in Figure 7.13. Figure 7.13 (a) shows charge/discharge curves at current densities of 0.5 - 5 mA that all displayed a non-linear shape with a shallow curve between 1.6 and 1 V due to pseudocapacitive reactions on the NiO-g cathode, together with an inflection point at 1 V with a steeper, linear portion between 1 and 0 V corresponding to double layer charge propagation only. The cycling behaviour at the different current densities is shown in Figure 7.13 (b) and suggested that after initial conditioning of the NiO-g electrode during the first 10 charge/discharge cycles, excellent capacitance retention of 98 - 100% was maintained at all current densities.

Corresponding energy and power densities were estimated from Equations 7.2 and 7.4 and a maximum specific energy of 11.3 Wh kg^{-1} at a corresponding specific

power of 1.4 kW kg^{-1} which reduced to 5.6 Wh kg^{-1} when a high specific power of 8.2 kW kg^{-1} was achieved.

7.4 Energy and power densities

Typical energy densities for current commercial supercapacitors based on activated carbon are 1 - 6 Wh kg^{-1} with power densities up to 15 kW kg^{-1}.[44] It is important to note that energy and power densities reported for single electrodes[45–48] do not have any 'real' meaning in a device context, and give potentially misleading, high values of specific energy as capacitance is always reduced for two electrode configurations.

A Ragone plot of the two-electrode cells in this chapter, compared with significant results from the literature,[49] is shown in Figure 7.14. Symmetric FeO_x/MWNT devices showed reduced specific energy compared with all the asymmetric configurations, as the voltage window was limited to 1 V. Although the highest energy densities from the literature were not surpassed by any of the sprayed electrode arrangements, acceptable energy densities of 8 - 20 Wh kg^{-1} were achieved. Power densities for all configurations were higher than most of the best literature and not lower than 1 kW kg^{-1}, possibly due to the thin film nature of the electrodes which was easily controllable to <500 nm (if necessary) with spray processing manufacture (although none of the literature values were also based on this film technologies). If the maximum specific power/power density of a supercapacitor is defined as:

$$P = \frac{V^2}{4R_s} \tag{7.5}$$

and $R_s = \frac{\frac{2}{3}t.r'}{A}$ where t is the electrode thickness,r' is resistivity and A is the electrode area, then, keeping all other factors constant, thinner electrodes will almost always lead to higher power densities.

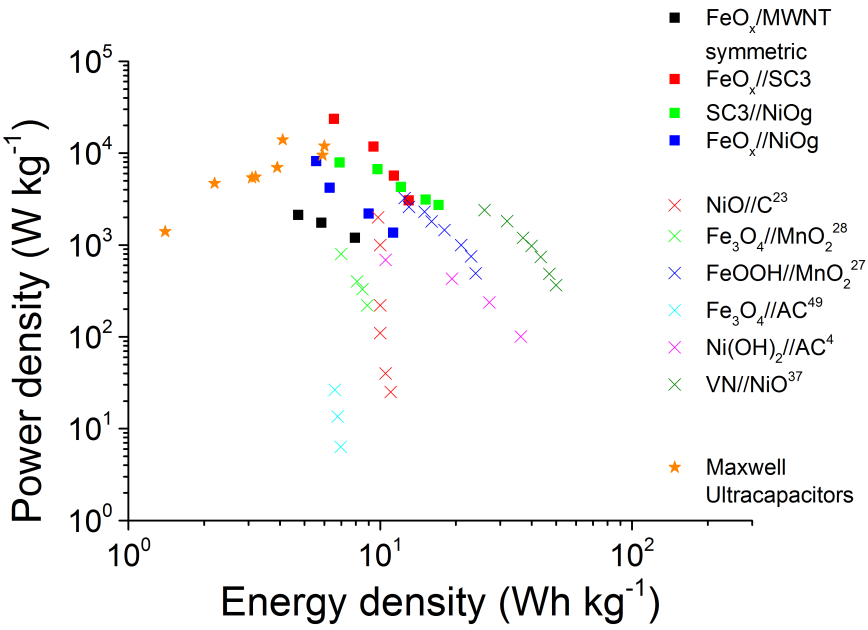

Figure 7.14: Ragone plot showing specific energy and power for full-cell devices in this chapter and some of the highest reports from the literature

7.5 Conclusions

Full-cell, all-sprayed, two-electrode devices utilising a combination of optimised transition metal oxide electrodes, carbon electrodes and a range of aqueous electrolytes in various combinations were investigated for their energy storage behaviour. Symmetric devices based on FeO_x/MWNT in Na_2SO_3 displayed reduced energy and power densities and cycling performance due to a restricted operating potential and slower kinetics for the pseudocapacitive-only reactions.

Asymmetric devices in KOH with a NiO-graphene cathode and carbon black anode

provided power densities of 2,700 W kg^{-1} at an specific energy of 17 Wh kg^{-1} and could be cycled reversibly with excellent capacitance retention of ∼97 % over 500 cycles. FeO_x/MWNT-NiO-g devices had the poorest performance of the asymmetric devices tested, due to the diminished redox activity of FeO_x electrodes in KOH, with a maximum specific energy of 11.3 Wh kg^{-1} at a relatively low specific power of 1,350 W kg^{-1}. Asymmetric devices with a FeO_x/MWNT anode and a SC3 cathode had a wide operating voltage window of 2 V in Li_2SO_4 and produced a maximum specific energy of 13 Wh kg^{-1} at a corresponding specific power of 3,100 W kg^{-1}. In general, the high power densities afforded by the relatively thin film sprayed electrodes were comparable to commercial symmetric devices using organic electrolytes and with higher energy densities, due to the wider operating voltage window provided in the asymmetric arrangement.

For improved performance, substrate choice might be optimised, for example by replacing ITO glass with a thin, high surface area nickel foam material for practical applications since the favourable morphology of Ni foam was shown to improve performance of single NiO-g electrodes in Chapter 6.

Bibliography

[1] Conway, B. *Electrochemical Supercapacitors: Scientific Fundamentals and Technological Applications*. Kluwer Academic/Plenum Publishers, (1999).

[2] Zhao, X., Johnston, C., and Grant, P. *J. Mat. Chem.* **19**(46), 8755–8760 (2009).

[3] Khomenko, V., Raymundo-Piero, E., and Bguin, F. *J. Power Sources* **177**(2), 643 – 651 (2008).

[4] Huang, J., Xu, P., Cao, D., Zhou, X., Yang, S., Li, Y., and Wang, G. *J. Power Sources* **246**(0), 371 – 376 (2014).

[5] Huang, J., Xu, P., and Wang, G. e. a. *J. Power Sources* **246**, 371–376 (2014).

[6] Yan, J., Fan, Z., and Wei, F. e. a. *Adv. Funct. Mater.* **22**(12), 2632–2641 (2012).

[7] Tang, Z., Tang, C., and Gong, H. *Adv. Funct. Mater.* **22**(6), 1272–1278 (2012).

[8] Lang, J., Kong, L., and Kang, L. e. a. *J. Sol. St. Electrochem.* **14**(8), 1533–1539 (2010).

[9] Qin, C., Bai, X., and Niu, H. e. a. *Pig. Res. Tech.* **38**(4), 230–235 (2009).

[10] X.F., W., D.B., R., and Z., Y. *Trans. Nonferrous. Met. Soc. China* **16**(5), 1129–1134 (2006).

[11] Shi, S., Xu, C., and Kang, F. e. a. *Sci. Rep.* **3** (2013).

[12] Wang, J., Yang, Y., Huang, Z., and Kang, F. *Carbon* **61**, 190–199 (2013).

[13] Shen, C., Wang, X., and Kang, F. e. a. *J. Power Sources* **234**, 302–309 (2013).

[14] Wu, Z., Ren, W., and Cheng, H. *ACS Nano* **4**(10), 5835–5842 (2010).

[15] Brousse, T., Taberna, P., and Simon, P. e. a. *J. Power Sources* **173**(1), 633–641 (2007).

[16] Fan, Z., Yan, J., and Wei, F. e. a. *Adv. Func. Mat.* **21**(12), 2366–2375 (2011).

[17] Cheng, Q., Tang, J., and Qin, L. e. a. *Carbon* **49**(9), 2917–2925 (2011).

[18] Wang, Q., Wen, Z., and Li, J. *Adv. Funct. Mater.* **16**(16), 2141–2146 (2006).

[19] Wang, Y., Wang, Z., and Xia, Y. *Electrochim. Acta* **50**(28), 5641–5646 (2005).

[20] Chen, C., Tsai, D., and Huang, Y. e. a. *Nanotech.* **23**(48) (2012).

[21] Jiang, M. *Processing and properties of nanostructured thin film energy storage devices*. PhD thesis, University of Oxford, (2013).

[22] Khomenko, E., Raymundo-Pinero, F., and Beguin, F. *J. Power Sources* **153**(1), 183 – 190 (2006).

[23] Zhang, X., Wang, X., Jiang, L., Wu, H., Wu, C., and Su, J. *J. Power Sources* **216**, 290–296 (2012).

[24] Wang, D., Li, F., and Cheng, H.-M. *J. Power Sources* **185**(2), 1563–1568 (2008).

[25] Luan, F., Wang, G., Ling, Y., Lu, X., Wang, H., Tong, Y., Liu, X.-X., and Li, Y. *Nanoscale* **5**(17), 7984–7990 (2013).

[26] Hong, M., Lee, S., and Kim, S. *Electrochem. Solid St.* **5**(10), A227–A230 (2002).

[27] Fan, Z., Yan, J., Wei, T., Zhi, L., Ning, G., Li, T., and Wei, F. *Adv. Funct. Mater.* **21**(12) (2012).

[28] Jin, W., Cao, G., and Sun, J. *J. Power Sources* **175**(1), 686–691 (2008).

[29] Cottineau, T., Toupin, M., Delahaye, T., Brousse, T., and Blanger, D. *Appl.Phys. A: Mater.* **82**(4 SPEC. ISS.), 599–606 (2006).

[30] Zhao, X., Johnston, C., and Grant, P. *J. Mat. Chem.* **19**(46), 8755–8760 (2009).

[31] Karthikeyan, K., Amaresh, S., Lee, S., Aravindan, V., and Lee, Y. *Chem. Asian J.* (2013).

[32] Yang, C., Shen, J., Wang, C., Fei, H., Bao, H., and Wang, G. *J. Mat. Chem. A* **2**(5), 1458–1464 (2014).

[33] Xiao, Y., Cao, Y., Gong, Y., Zhang, A., Zhao, J., Fang, S., Jia, D., and Li, F. *J. Power Sources* **246**, 926–933 (2014).

[34] Wu, T., Chu, Y., Hu, C., and Hardwick, L. *Electrochem. Comm.* **27**, 81–84 (2013).

[35] Wu, T., Hsu, C., Hu, C., and Hardwick, L. *J. Power Sources* **242**(0), 289 – 298 (2013).

[36] In *Equivalent Circuit Modeling Using the Gamry EIS300 Electrochemical Impedance Spectroscopy Software*. Gamry Instruments.

[37] Yuan, C., Zhang, X., Su, L., Gao, B., and Shen, L. *J. Mater. Chem.* **19**(32), 5772–5777 (2009).

[38] Eustache, E., Frappier, R., Porto, R., Bouhtiyya, S., Pierson, J., and Brousse, T. *Electrochem. Comm.* **28**, 104–106 (2013).

[39] Gao, Z., Zhang, H., Cao, G., Han, M., and Yang, Y. *Electrochim. Acta* **87**, 375–380 (2013).

[40] Chang, T., Wang, X., Evans, D., Robinson, S., and Zheng, J. *J. Power Sources* **110**(1), 138 – 143 (2002).

[41] Wang, H., Liang, Y., Gong, M., Li, Y., Chang, W., Mefford, T., Zhou, J., Wang, J., Regier, T., Wei, F., and Dai, H. *Nat. Commun.* **3** (2012).

[42] Liu, Z., Tay, S., and Li, X. *Chem. Comm.* **47**(46), 12473–12475 (2011).

[43] Qu, Q., Yang, S., and Feng, X. *Adv. Mater.* **23**(46), 5574–5580 (2011).

[44] http://www.maxwell.com/products/ultracapacitors/docs, (2014).

[45] Sethuraman, B., Purushothaman, K., and Muralidharan, G. *RSC Adv.* **4**(9), 4631–4637 (2014).

[46] Guan, D., Gao, Z., Yang, W., Wang, J., Yuan, Y., Wang, B., Zhang, M., and Liu, L. *Mat. Sci. Eng. B-Solid* **178**(10), 736–743 (2013).

[47] Yan, J., Fan, Z., Wei, T., Cheng, J., Shao, B., Wang, K., Song, L., and Zhang, M. *J. Power Sources* **194**(2), 1202–1207 (2009).

[48] Xia, X., Tu, J., Mai, Y., Chen, R., Wang, X., Gu, C., and Zhao, X. *Chem. Euro. J.* **17**(39), 10898–10905 (2011).

[49] Du, X. Wang, C. and Chen, M. *J. Phys. Chem. C.* **113**(6), 2643–2646 (2009).

Chapter 8

Conclusions and future work

Two low cost, scalable transition metal oxide systems have been investigated for their suitability for energy storage applications. Iron oxide and nickel oxide materials were synthesised with controlled nanomorphology, and then fabricated into thin (< 5 μm) film electrodes by atomised spray deposition in combination with nanostructured carbon conductivity additives. The composite electrodes were investigated using various electrochemical methods, both in two and three electrode configurations in a range of suitable electrolytes, with a general focus on aqueous electrolyte systems.

Due to its low cost, low toxicity, ease of handling, and attractive behaviour in previous energy storage devices, FeO_x nanostructures were synthesised using a low temperature, hydrothermal synthesis. The resultant 1-dimensional nanostructures were fabricated into self supporting, porous electrodes with multi-walled carbon nanotubes (MWNT) added to improve through-electrode conductivity. The best energy storage behaviour was observed when a 4:1 mass ratio of FeO_x:MWNT, which resulted in

a maximum specific capacitance of 312 F g^{-1} in a 0.5 M Na_2SO_3 electrolyte via a mechanism of charge storage due to redox activity of adsorbed SO_3^{-2} ions. Comparing the electrochemical behaviour in several aqueous, benign electrolytes, when the SO_3^{2-} ion was not present, the charge transfer mechanism involved reactions at the FeO_x surface, which resulted in lower specific capacitances and enhanced capacitance fading. Future work could consider how to reduce the cost of the electrodes by either investigating alternative, lower cost conductivity additives to MWNTs and/or iron oxide structures that do not rely so heavily on rather bespoke, low productivity hydrothermal routes.

The FeO_x/MWNT electrodes were then investigated for their behaviour as a Li-ion battery (LiB) electrode in a $LiPF_6$ electrolyte. A first discharge cycle capacity of 1180 $mAhg^{-1}$ faded to 400 $mAhg^{-1}$ after 20 cycles. The intimate combination of two 1-D nanomaterials that underpinned the favourable properties during the surface-dominated charge storage in the supercapacitor system was of less importance during the bulk intercalation/de-intercalation charge storage in $LiPF_6$. Therefore, future work could consider the effect of the nanomorphology of the iron oxide for LiB applications and the structural integrity of the carbon conductivity addition. If different electrode material nanomorphologies were employed then the spray parameters would need to be investigated and re-optimised to produce the highest performing electrode structure.

Nickel oxide (NiO)/exfoliated graphene electrodes were manufactured using several different spray processing variants. NiO nanostructures were synthesised using a low temperature hydrothermal synthesis followed by high temperature annealing, and aqueous graphene suspensions were produced via a room-temperature ultrasonic exfoliation technique. Synthesis of NiO in a graphene suspension and spraying

the resultant composite material into electrodes produced superior energy storage properties compared with combining the two materials at a later stage of electrode manufacture, due to improved physical contact and an increase in defect concentration within the graphene nano-sheets. The co-synthesis electrodes produced a specific capacitance from cyclic voltammetry of 248 F g^{-1} at 2 mV s^{-1} in 2 M KOH when an ITO/glass substrate was employed, which increased to 742 F g^{-1} when the composite material was sprayed onto a high surface area Ni foam substrate, due to an (often ignored) electrochemical contribution of the Ni substrate in KOH. High charge storage behaviour for the NiO/graphene electrodes on the Ni foam substrate was maintained to over 300 F g^{-1} at a very high charge/discharge current density of 100 A g^{-1}. Future work expanding on the NiO/graphene results might focus on further integration of low cost transition metal oxide and carbon materials for hybrid electrodes, for example by co-spraying or layer-by-layer spraying. Alternatively, investigations into the effect of spray parameters e.g. flow rate of each suspension, nozzle height etc could be expanded to better define the structure/property relationship of NiO/graphene co-sprayed electrodes.

Finally, FeO_x/MWNT and NiO/graphene electrodes were fabricated and tested in two-electrode, aqueous, asymmetric devices to extend the working operation potential compared with two-electrode symmetric devices. A commercial carbon black electrode was also fabricated and used to provide EDLC capacitance for high power properties. The appropriate potential window/electrolyte combination was investigated through cyclic voltammetry and electrochemical impedance spectroscopy, and FeO_x/MWNT-carbon, NiO/graphene-carbon and FeO_x/MWNT-NiO/graphene configurations were studied for their energy/power characteristics. The specific power of all of the sprayed asymmetric devices was higher than that of comparable slurry/cast devices in the literature; not lower than 1,000 W kg^{-1} for current densities of 0.5 A

g^{-1}, and above 10,000 W kg^{-1} for current densities up to 10 A g^{-1} due to the thin film (< 10 μm) nature of the electrodes. Capacitance was retained at >95 % after 1000 cycles for all of the asymmetric combinations. FeO_x/MWNT-carbon devices with Li_2O_4 electrolyte showed the best performance with a maximum experimental specific power of 23.5 kW kg^{-1} and a maximum experimental specific energy of 13 W kg^{-1}.

Future work relating to aqueous, asymmetric supercapacitor devices might investigate optimising the EDLC electrodes used to pair with FeO_x/MWNT and NiO/graphene electrodes in terms of material properties and electrode morphology. The substrate/current collector used with a KOH electrolyte should be changed from solid ITO/glass to a flexible metal foil for real-life, rolled devices. There is potential for fabrication of an all-sprayed, Fe-Ni battery for high energy applications using Fe_2O_3/$Ni(OH)_2$ electrodes rather than FeO_x/NiO. Finally, to achieve a device that removes the need for liquid handling and complicated cell manufacture, investigation into solid state electrolytes in combination with transition metal oxide/carbon electrodes might lead to the fabrication of an integrated, all-sprayed, asymmetric device.